Searching for Signatures of Electromagnetic Cascades in the Intergalactic Medium initiated by Blazars.

A dissertation submitted to the University of Dublin
for the degree of Doctor of Philosophy

Lisa Fallon
September 2012

School of Physics
University of Dublin
Trinity College Dublin

School of Cosmic Physics
Dublin Institute for
Advanced Studies

Declaration

I hereby declare that this thesis has not been submitted as an exercise for a degree at this or any other University and that, except where otherwise stated, it is entirely my own work.

I agree that the Library may lend or copy this thesis upon request.

Signed,

Acknowledgments

I must begin by thanking my supervisor, Prof. Felix Aharonian, with whom it has been a great privilege to work with. From the very beginning, I was given complete freedom and every opportunity was made available to me. Thank you for you kindness and support, and for giving me a push in the right direction when needed. I would also like to thank Prof. Luke Drury who kept a watchful eye on the students office, provided great support and has always been willing to share his wisdom (and humour!). A huge thank you is due to Prof. Jim Hinton for being a warm host on my trips to Leeds and Leicester. Your infinite patience, kindness and making yourself available for every minor problem will not be forgotten! Having these three great professors supporting me has made my life as a student very enjoyable and it has been a pleasure to learn from you.

I would like to acknowledge Dr. Anant Eungwanichayapant for the use of his Monte Carlo simulations in this work. I wish to thank Dr. Andrew Taylor for being a great collaborator. Your endless enthusiasm and energy was infectious and gave me a great push over the past few months. Thank you for sharing your knowledge (and your Monte Carlo results!) and for adding to the scientific value of this work. The "future work" section of this thesis benefited from the work provided by Dr. Richard White. Thanks Rich for all your help and for answering all my questions, as well as being great fun to work with. You acted as my CTA expert and taught me a lot! I would also like to acknowledge the work of Dr. Denis Malyshev, who provided the *Fermi* analysis results presented here. Thank you for always making yourself available to discuss your results. I would like to thank Dr. Brian Espey as my internal supervisor in Trinity for his support and for making the DIAS-TCD connection so accessible.

My life with H.E.S.S. began in Heidelberg with a crash course in the analysis provided by Dr. Anna Szostek and Dr. Martin Raue - thank you for giving me a great foundation and getting me started. I also wish to thank Dr. Christopher Van Eldik who shared his experience on extended analysis and helped a great deal in ironing out teething problems in the early days. I must acknowledge all the wonderful people I've met through the H.E.S.S. and CTA collaborations - especially Pol and Karl who always made the collaboration meetings more enjoyable.

I have very fond memories of my time in Heidelberg and was always made to feel part of the group in MPIK. I would like to thank Ms. Gabi Weese for her inexhaustible kindness and for making German bureaucracy seem effortless. A big thank you to Emma, Sabrina, Olga, Eva, Ervin, Frank and the rest of the group for being such great company. A big thank you goes to Ros & Chris for hosting me on more than one occasion, and to Surhud & Anu for the unforgettable trip to India. Thank you Giovanna for keeping me sane on the H.E.S.S. shift and

for providing fantastic support in the past year when I needed it most. A heartfelt thanks to Giulia and Claudia whose company in Salerno was a real tonic. Of course, I could not refer to Heidelberg without mentioning Marcello. Thank you for teaching me so much, especially about myself.

My time in DIAS has been greatly enriched by the friendships I've made here : to the rest of the astro redheaded trio, Rachael and Gráinne - thank you for being such great friends and for always making me laugh; the Italians (and italian speakers!) who were always great company - Stefano, Linda, Alessio and Rebeca - grazie per tutto; thank you Deirdre for listening and understanding, and for providing the beautiful layout of this thesis; thanks to Eileen for being such a mother-hen and looking after me a little when times were hard; thanks Paul and Emma for proof reading and all the lunchtime chats in the kitchen; thank you Valenti for listening to my hyper rants on occasion and for all your help in organising the summer school last year; thanks to present and past office-mates : Nakisa, Anne, Séan and Jonathan; thanks Philippe for all your help with computer related issues and to the rest of the staff in DIAS who have made the atmosphere at the institute so familial. I would also like to thank the extended DIAS family, including Jan, Javier and Thomas whose friendship and support have really helped get me through a tough year - and thanks to all the other students from Geophysics and Theoretical Physics (especially Matthew, Andrew, Duygu, Martin and my climbing buddy Joanne!).

Last but not least, I would like to thank the people behind the scenes who have kept me going and have always been there for me when I needed them: Bennan for all the great conversations (and the fab girly weekend in Zürich - I'm looking forward to the next one!); thanks to the Galway girls Eleanor, Liz and Sarah for always listening and understanding my weird ways!; thanks to James for reappearing in my life when times were toughest and being such fantastic support; thanks are due to Derek who came along at just the right time and stopped me from unravelling completely - your friendship and kindness have meant a lot. I would like to thank Cornucopia for keeping me well fed in the final months of my thesis and to Mooji for giving me so much inspiration and peace. Thanks to Mam, Dad for everything - although you haven't always understood my choices, you've always supported me. To my siblings David and Aoife, thanks for always reminding me not to take myself too seriously. The loss of our brother Paul has been very difficult for all of us but we will never forget him.

Summary

Very high energy (VHE) γ-ray astronomy has opened a new window into the Universe at the highest energies, allowing the exploration of unique astrophysical phenomena. This thesis constitutes an observational contribution to understanding the processes in the intergalactic medium as well as the resulting physical structures, in particular pair halos and beam broadened cascade emission. Pair Halos are giant electron-positron structures which are formed due to the development of pair cascades, initiated by interactions of primary multi-TeV photons from high energy extragalactic sources with the extragalactic background photon fields.

It is well known that the intergalactic medium (IGM) is not fully transparent to very high energy ($E > 100$ GeV) gamma-rays from extragalactic sources for which the propagation length is on a cosmological scale. VHE γ-rays interact with the background photon field, namely the Extragalactic Background Light (EBL). The spectral energy distribution of the EBL has two main features - a first peak around 1 μm produced from starlight and a second peak at $\sim 100\,\mu$m resulting from starlight which has been absorbed and reemitted by dust in galaxies. Through these interactions the initial VHE gamma-rays are absorbed via $\gamma\gamma$ pair production (PP) process.

Fortunately, the energy of the VHE γ-rays is not lost due to the resulting electron-positron ($e^{\pm}$) pairs, which in turn interact with the soft background photons through the process of inverse Compton scattering (IC). If the energy of the upscattered photons is higher than the PP threshold energy, this process will take place again. This sequence of PP and IC processes is generally known as the electromagnetic cascade.

The magnetic field strength in the vicinity of the source plays a key role in the formation of a pair halo. A magnetic field ($\mathbf{B} > 10^{-12}$ G) is required to isotropise the $e^{\pm}$ pairs in the cascade and hence the secondary gamma ray photons. This will lead to the formation of an isotropic halo around the VHE gamma-ray source. However, if a weaker magnetic field is present ($< 10^{-12}$ G), the cascade energy flux will continue to propagate along the initial beam direction, broadening the beam width as it does so. The angular size of this beam broadened cascade is dictated by the extragalactic magnetic field (EGMF) strength. A measurement of the beam width can provide a strong constraint on the EGMF value. The radiation from both pair halos and beam broadened cascades can be recognised by a distinct variation in intensity with angular distance from the centre of the source.

The High Energy Stereoscopic System (H.E.S.S.) array of four imaging atmospheric Cherenkov telescopes (IACT) is utilised in this work to search for extended blazar emission. The energy and angular distributions of three sources, namely 1ES 1101-232, 1ES 0229+200 and PKS 2155-304 were studied in detail. Initially, a standard H.E.S.S. analysis of these sources

is presented. Detailed morphological and spectral analyses are performed for all three AGN, as well as demonstrating their suitability for this study. This is followed by a more specialised analysis searching for extended emission around these blazars.

It is now understood that electron-positron pairs are inevitably produced following TeV gamma-ray emission from blazar sources, through the interaction of these γ-rays with the Extragalactic Background Light through PP and IC processes. Depending on the magnetic fields in the proximity of the source, the cascade initiated from pair production can result in either an isotropic halo around an initially beamed source or a beam broadened cascade flux. We searched for both extended Pair Halo (PH) and Beam Broadened Cascade (BBC) emission around the blazars 1ES 1101-232, 1ES 0229+200 and PKS 2155-304 using VHE data from the H.E.S.S. telescope array and HE data from the *Fermi*-LAT. By comparing the angular distributions of the reconstructed gamma-ray emission to that of a point-like source, it is possible to investigate if extended emission is present. For pair halos, upper limits for extended emission calculated for each of the three sources are presented. For beam broadened cascades, it is possible to exclude Extra-Galactic Magnetic Fields (EGMF) values in the range 3 to 9×10^{-15} G.

Finally, the prospects of pair halo detection with future detectors is discussed. Eighteen years after the concept of pair halos are was first proposed, the Imaging Atmospheric Cherenkov telescopes are now edging closer to the possibility of observing this elusive phenomenon. The potential of the next generation IACT, the Cherenkov Telescope Array (CTA) is explored, with the results from simulations presented. In addition, Monte Carlo simulations have been performed to reflect the improvements made in recent years in EBL modelling, as well as investigating the results for a more distant blazar, with a redshift $z \approx 0.2$ — 1ES 1101-232 being a prime example. Consequently, a suitable source for future observations is suggested, the radio galaxy 3C 15. Due to their powerful nature, radio galaxies are ideal candidates for a pair halo search. Details as to why this may provide an opportunity to detect pair halo emission in the future are discussed.

Contents

List of Figures

List of Tables

List of Acronyms

AGN	**A**ctive **G**alactic **N**uclei
CBR	**C**osmic **B**ackground **R**adiation
CIB	**C**osmic **I**nfrared **B**ackground
CMB	**C**osmic **M**icrowave **B**ackground
CoG	**C**entre of **G**ravity
CTA	**C**herenkov **T**elescope **A**rray
EAS	**E**xtensive **A**ir **S**hower
EBL	**E**xtragalactic **B**ackground **L**ight
EGMF	**E**xtra**G**alactic **M**agnetic **F**ield
HESS	**H**igh **E**nergy **S**tereoscopic **S**ystem
IACT	**I**maging **A**tmospheric **C**herenkov **T**echnique
IC	**I**nverse **C**ompton
IGM	**I**nter**G**alactic **M**edium
LAT	**L**arge **A**rea **T**elescope
MSRL	**M**ean **R**educed **S**caled **L**ength
MSRW	**M**ean **R**educed **S**caled **W**idth
NSB	**N**ight **S**ky **B**ackground
PMT	**P**hoto**M**ultiplier **T**ube
PP	**P**air **P**roduction
PSF	**P**oint **S**pread **F**unction
SED	**S**pectral **E**nergy **D**istribution
VHE	**V**ery **H**igh **E**nergy

Publications

Fallon, L., & the H.E.S.S. Collaboration, (2012),
"Search for extended blazar emission with H.E.S.S.",
Astronomy and Astrophysics, in prep

Fallon, L., & the CTA Collaboration, (2012),
"Active Galactic Nuclei under the scrutiny of CTA",
Astroparticle Physics, submitted

Fallon, L., & the H.E.S.S. Collaboration, (2010),
"Searching for extended Pair Halo emission",
25th Texas Symposium on Relativistic Astrophysics, confE, 192F

Fallon, L., & the H.E.S.S. Collaboration, (2010),
"Searching for Pair Halos",
38th COSPAR Scientific Assembly, 38, 2302

Bartu, P., Koeppe, R., Arnold, N., Neulinger, A., **Fallon, L.** & Bauer, S., (2010),
"Conformable large-area position-sensitive photodetectors based on luminescence-collecting silicone waveguides",
Journal of Applied Physics, 107, 123101

1

Introduction to γ-ray Astronomy

γ-ray astronomy is a relatively young science. However, long before we had experiments which could detect γ-rays from cosmic sources, theoretical calculations led astrophysicists to believe that several processes occurring in the Universe would result in the emission of γ-rays (see Morrison 1958). γ-rays are electromagnetic radiation in the range of about 100 keV upwards. In very high energy (VHE) astrophysics, we focus on photons which have an energy above 100 GeV, due to the limitations of ground-based detectors.

γ-rays from space are almost completely absorbed by the Earth's atmosphere, therefore the first experiments were either placed on balloons or on-board spacecraft. The first γ-ray telescope was launched into the Earth's orbit in 1961 on-board the Explorer XI satellite. Although this instrument only detected less than 100 γ-ray photons, the era of γ-ray astronomy was born and has progressed in leaps and bounds since then.

In more recent times, a sophisticated technique for ground-based γ-ray observation has been developed. Although the Earth's atmosphere is opaque to very high energy photons, the secondary effects of this atmospheric absorption can be detected. This observation technique exploits the Cherenkov effect (Čerenkov 1937). This effect was first discovered by the Russian physicist Pavel A. Čerenkov (1904 - 1990) in the course of nuclear physics experiments (Figure 1.1). He was awarded the Nobel Prize in Physics for this discovery in 1958. Further details

on the Imaging Atmospheric Cherenkov Technique (IACT) will be presented in Chapter 2, as well as describing its crucial role in γ-ray astrophysics.

The first Cherenkov light pulses from atmospheric air showers were registered by Galbraith & Jelley 1953. This was followed by an attempt to detect γ-rays from astrophysical sources with the first atmospheric Cherenkov telescopes (Jelley & Porter 1963) resulting in meaningful upper limits. Years later, the first detection of a TeV γ-ray source, the Crab Nebula, was with the 10 m Cherenkov telescope of the Whipple Observatory in 1989 (Weekes et al. 1989). Since this initial detection of the Crab, research in this field has flourished. For many years, the most advanced instrument in observational γ-ray astronomy was the *Energetic Gamma-Ray Experiment Telescope* (EGRET) which was on board the Compton Gamma-Ray Observatory (CGRO). This instrument provided a rich data set of many interesting sources. However, when ground-based observatories became more developed, new source classes not seen by EGRET were revealed, much to the delight of the newly emerging γ-ray community.

VHE γ-ray astronomy is emerging as an important discipline in both high energy astrophysics and astroparticle physics. At the lower end of the VHE energy range, space based telescopes are ideal for studying sources which emit at these energies. However, beyond $\sim$ 100 GeV or so, the detection area of these satellite detectors is limited and therefore the region of VHE γ-rays above 100 GeV remains the domain of ground-based astronomy. A common characteristic of the photon spectra at these high energies is that the flux decreases very rapidly as the energy increases, so large detection areas are needed (e.g. $\sim$ 100 m^2).

In the last decade, Cherenkov telescopes such as CANGAROO (an acronym for **C**ollaboration of **A**ustralia and **N**ippon (Japan) for a **GA**mma **R**ay **O**bservatory in the **O**utback), H.E.S.S (the High Energy Stereoscopic System), MAGIC (the Major Atmospheric Gamma-ray Imaging Cherenkov Telescopes), VERITAS (the Very Energetic Radiation Imaging Telescope Array System) as well as the *Fermi Gamma-ray Space Telescope* have made significant progress in pushing down the detection energy threshold and sensitivity, increasing almost exponentially the number of detected GeV and TeV sources.

1.1 γ-Ray Astronomy

γ-rays provide one of the best windows into the non-thermal Universe with the ability to probe fundamental physics beyond the capabilities of terrestrial particle accelerators. At present, the energy region of γ-rays is explored rather inhomogeneously. Although there is little doubt of the existence of "ultra" (or PeV) and "extremely" (EeV) high energy photons, until now primary cosmic γ-rays have been detected only in the *low* (MeV), *high* (GeV) and *very high* (TeV)

Figure 1.1: *Left: Russian stamp commemorating Pavel Čerenkov, discoverer of the Cherenkov effect. Right: Victor Hess preparing to take flight in 1912.*

energy domains.

The term 'gamma-ray' is a generic one which is used to describe a photon which has an energy in the range of 100 keV (10^5 eV) to > 100 EeV (10^{20} eV). γ-ray astronomy involves the detection of light from astronomical objects with photon energies of up to 10^9 times more energy than visible light. The area of modern astrophysics plays a crucial role in the exploration of non-thermal phenomena in the Universe, witnessed in all their violent forms. γ-rays cover a wide range in energy (from 10^6 eV to > 10^{12} eV), more than the combined emission from all remaining wavebands of electromagnetic radiation from keV x-rays to MHz radio waves. A wide variety of detection techniques is therefore required to cover this huge energy band.

The wavelength region considered in this work, very high energy γ-rays, are characterised by wavelengths in the range of 10^{-18} m and energies ~ 1 TeV = 10^{12} eV = 1.602 x 10^{-7} J (Figure 1.2), using the formula

$$E = hc/\lambda \tag{1.1}$$

with energy E, wavelength λ, Planck's constant h and the speed of light c.

1.1.1 Cosmic Rays

The field of astroparticle physics will celebrate its 100 year anniversary this year, marking the first discovery of ionising rays coming from the cosmos in 1912. Victor Hess (Figure 1.1)

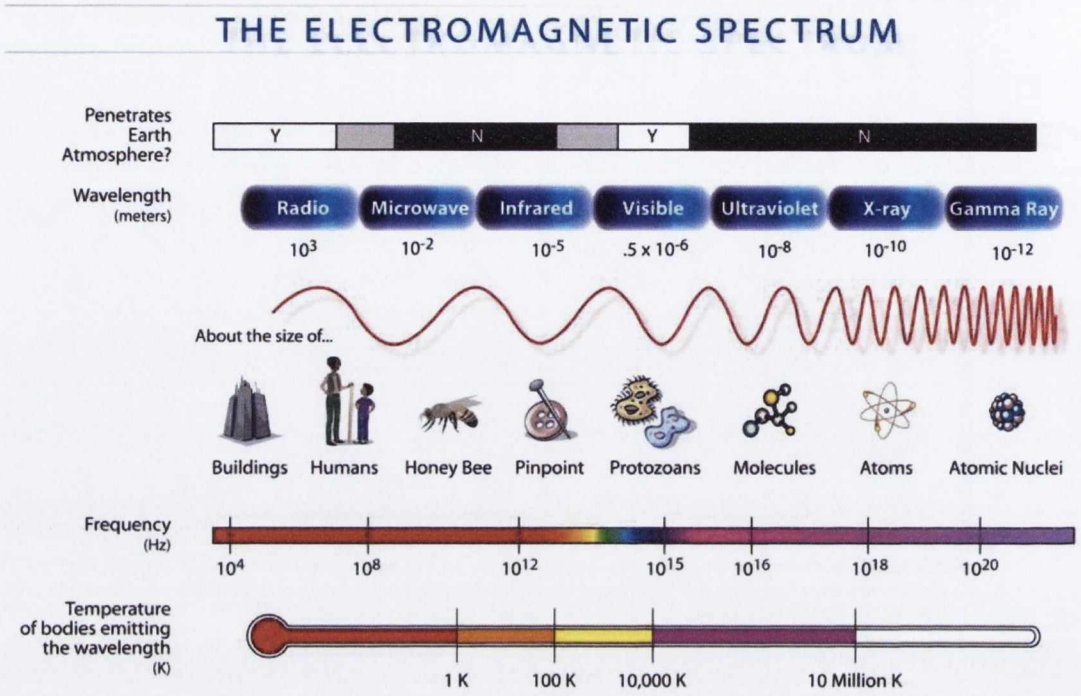

Figure 1.2: *The electromagnetic spectrum ranging from radio to γ-rays. Only a small fraction of the spectrum can penetrate the Earth's atmosphere (Courtesy of NASA).*

received the Nobel Prize in Physics for this discovery in 1936, and the H.E.S.S. (High Energy Stereoscopic System) experiment is named in his honour. The ionising radiation observed, which constantly bombards the Earth's atmosphere, increases with height, as witnessed in his balloon experiments in 1912. He attributed this to an ionising radiation from outer space, now known as 'cosmic rays'. Cosmic rays have been found to be mainly made of electrically charged particles, mostly protons, but their composition changes with energy (Antoni et al. 2005). There are contributions by heavier elements and from other stable particles, such as alpha particles, photons and even a small fraction of electrons. The overall differential cosmic ray spectrum is given in Figure 1.3. It extends over an energy range of 13 orders of magnitude with the flux dropping from $\sim$ 1 particle / cm^2 / second at energies of 10^8 eV, to a rate of $\sim 10^2$ particles / km^2 / year at 10^{20} eV.

The flux of charged cosmic radiation, over the energy range of interest to the VHE γ-ray astronomer is in the order of 10^3 - 10^4 times that of the diffuse γ-ray background. Cosmic ray ions interact in the upper atmosphere and initiate a cascade in a way which is superficialy similar to an electromagnetic cascade. The effect this has on our ability to take data will be

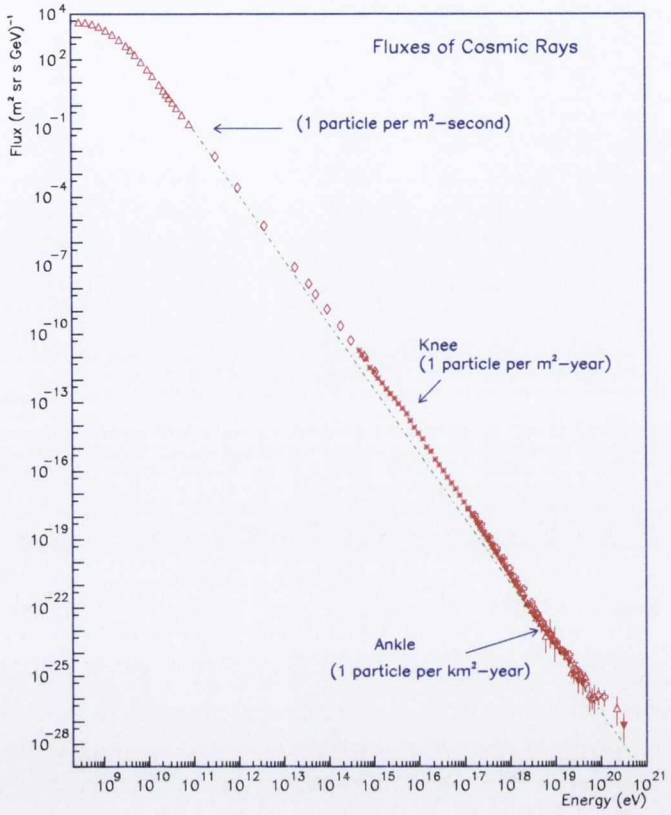

Figure 1.3: *All-particle cosmic ray spectrum (Bhattacharjee 2000).*

discussed in Chapter 2.

The spectrum roughly follows a power law, $dN/dE \sim E^{-\alpha}$ with a slope of $\alpha \approx 2.7$. The slope steepens at energies around 10^{15} eV, known as the knee (see Figure 1.3). One possible explanation for this steepening, is that the particles with energies above the knee are no longer confined by the galactic magnetic fields and hence diffuse out of our Galaxy. A second change of slope (known as the ankle) occurs at $\sim 10^{18}$ eV. A suppression, sometimes referred to as a cut-off, is expected at energies $> 5 \times 10^{19}$ eV, where the cosmic rays start to interact with the photons of the cosmic microwave background (CMB); (Greisen 1966; Zatsepin & Kuz'min 1966).

The origin of cosmic rays is not yet known. It is thought that cosmic rays below the knee are produced at galactic sites such as supernova remnants, pulsars or binary systems. For particles with energies exceeding 10^{18} eV, an extragalactic origin is likely, since these particles are no longer confined to the galaxy by the galactic magnetic fields.

Due to these magnetic fields, both galactic and intergalactic, charged cosmic rays up to 10^{19} eV are isotropised. Therefore, their arrival direction at Earth does not point back to their source of origin. Only at even higher energies, in the regime of ultra high energy cosmic rays, the

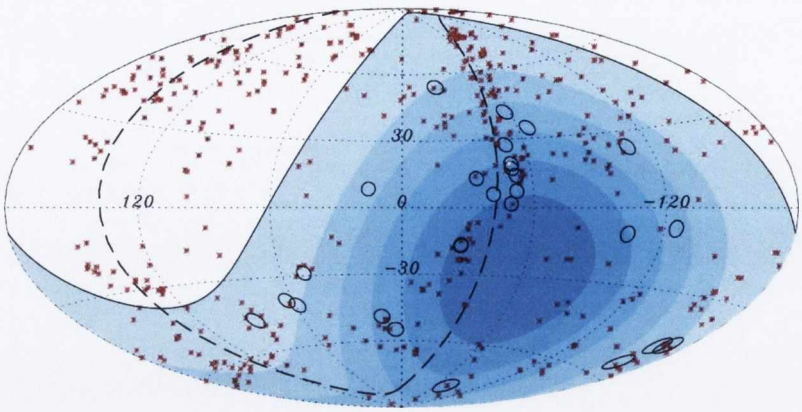

Figure 1.4: *Arrival directions of the Auger highest energy events. Black circles indicate the arrival directions of the 27 highest energy events recorded by the Pierre Auger Observatory. Red asterisks show the catalogue position of nearby active galactic nuclei (The Pierre Auger Collaboration et al. 2007).*

rigidity $R = E/Ze$ of the particles is so high (with a charge Ze), that they are not expected to be significantly deflected by extragalactic or galactic magnetic fields ($r_{gyro} = R/B$). In this context, rigidity is a concept used to determine the effect of magnetic fields on the motion of charged particles.

The Akeno Giant Air Shower Array (AGASA), a 100 km^2 scintillator air shower array in Japan, claimed anisotropies in the arrival direction of the highest energy cosmic rays (Takeda et al. 1999). This anisotropy was supported by results from the more sensitive Pierre Auger Observatory (The Pierre Auger Collaboration et al. 2007) as shown in Figure 1.4. They claimed a correlation between the arrival direction of Ultra High Energy Cosmic Rays (UHECR) and the Active Galactic Nuclei (AGN) present in the Veron-Cetty Veron (VCV) Catalogue (Véron-Cetty & Véron 2006).

However, a direct connection between AGN and UHECR is still a controversial claim. It must be kept in mind, that nothing is known about UHECR sources other than that they have to satisfy the so-called "Hillas criterion": the particles must be confined in the acceleration region long enough to be able to reach Ultra High Energies (Hillas 1984). It should also be noted that the catalogue used in the above study is highly inhomogeneous and incomplete, as the authors themselves concede in the article. In more recent times, as more data has been collected, the Auger collaboration have stated that the degree of correlation has decreased, but still provides evidence for anisotropy of UHECTs at E > 55 EeV at a 99% confidence limit.

1.1.2 Sources of Cosmic Rays

Finding the sources of cosmic rays has always been a key motivation for VHE γ-ray astronomers. In 2001, the HEGRA experiment detected VHE γ-rays from the supernova remnant (SNR) Cassiopeia A (Aharonian et al. 2001a). This was followed by two more detections of shell type SNR sources and for the first time, produced images of the shell morphology in VHE γ-rays (Aharonian et al. 2005c, 2006a, 2004b). These detections point towards SNRs as at least one of the sources of Cosmic Rays, but open questions still remain. A definite proof for hadronic acceleration in SNRs would be the detection of neutrinos from these sources with neutrino telescopes such as IceCube (Karle, for the IceCube Collaboration 2010) or KM3NeT (Katz 2006).

Proposed sources of extragalactic Cosmic Rays include relativistic jets in AGN, γ-ray bursts and massive star clusters. For a recent review of Ultra high energy cosmic rays, as well as current open questions see Kotera & Olinto (2011).

1.1.3 Production of VHE γ-rays

Unlike the charged components of cosmic radiation, cosmic ray photons are not deflected by magnetic fields and thus point back to their source. Therefore, the knowledge of γ-ray production sites allows the study of the physical properties of the sources and the acceleration mechanisms at work.

From the power-law shape of the cosmic-ray spectrum and the extremely high energies involved, it is evident that the radiation originates from non-thermal acceleration processes rather than from the black-body radiation of thermal processes. The hottest objects observed in the universe emit thermal radiation with energies extending up to the hard X-ray range of ≈ 10 keV. Hence, any radiation exceeding these energies must be created in non-thermal processes. VHE γ-rays provide a unique opportunity for the study of such non-thermal acceleration processes. They are abundantly produced in interactions of highly energetic particles with ambient radiation fields and matter in the interstellar medium. They propagate freely through interstellar space, unperturbed by magnetic fields. On galactic scales, they do not suffer from absorption by infrared and optical photon background fields. Non-thermal photons may be produced via inverse compton scattering, indicating a site of leptonic acceleration, and by pion decay, a result of hadronic acceleration.

The most relevant elementary processes that produce γ-rays are briefly described in the following (Longair 1992):

π^0 decay: As the lightest hadrons with $m_\pi \approx 135$ MeV, neutral and charged pions are among the hadronic end products of nucleonic cascades. Charged ($\pi^\pm$) and neutral (π^0) pions are produced

with the same probability. Neutral pions have a very short lifetime, of $\sim 10^{-16}$ s and decay into two very high energy photons. With their considerably longer lifetime of $\sim 2.6 \times 10^{-8}$ s, high energy charged pions usually undergo further interactions before they eventually decay into electrons and neutrinos.

Inverse Compton Scattering: Relativistic electrons can transfer part of their energy to lower energy photons through the process called inverse compton scattering. For $E_e \cdot E_\gamma \ll m_e^2 c^4$, the cross section needed is the Thomson cross section:

$$\sigma_T = \frac{3}{8}\pi r_e^2 \tag{1.2}$$

For $E_e \cdot E_\gamma \approx m_e^2 c^4$, the exact Klein-Nishina formula has to be used (Weinberg 1995). However, in the case of ultra-relativistic electrons, $E_e \cdot E_\gamma \gg m_e^2 c^4$, the approximation becomes:

$$\sigma_{KN} = \pi r_e^2 \frac{1}{\epsilon}(ln(2\epsilon) + 0.5), \quad \epsilon = \frac{E_\gamma}{m_e c^2} \tag{1.3}$$

In this regime, the electrons suffer large energy losses. It can be shown that the maximum energy gain is $E_{max} \approx 4\gamma^2 E_\gamma$ for Lorentz factors of $\gamma \approx 10^2 - 10^4$, where the Lorentz factor can be defined as

$$\gamma = \frac{1}{\sqrt{1 - v^2/c^2}} \tag{1.4}$$

This means that keV seed photons are upscattered to the Gev-TeV domain. This is the mechanism at work in synchrotron self-Compton models.

Synchrotron radiaton: In the presence of magnetic fields, relativistic charged particles emit Synchrotron radiation. For electrons, the peak emission energy is given by $E_{peak} = 5 \times 10^{-9} B_\perp \gamma_e^2$eV, with $B_\perp$, the transverse component of the magnetic field, given in units of Gauss. Synchrotron radiation of accelerated electrons is one of the most important processes in the non-thermal Universe. In the context of VHE γ-rays, synchrotron radiation is the usual process for the generation of seed photons for the above described Inverse Compton scattering. In addition, ultra-high energy cosmic rays can emit synchrotron photons directly in the VHE domain.

Electron Bremsstrahlung: When charged particles are deflected (or accelerated) in electric fields, they radiate Bremsstrahlung. The emitted photon spectrum has a power law form, with the same spectral index as the accelerated particles. Bremsstrahlung of ultra-high energy cosmic rays can reach TeV energies.

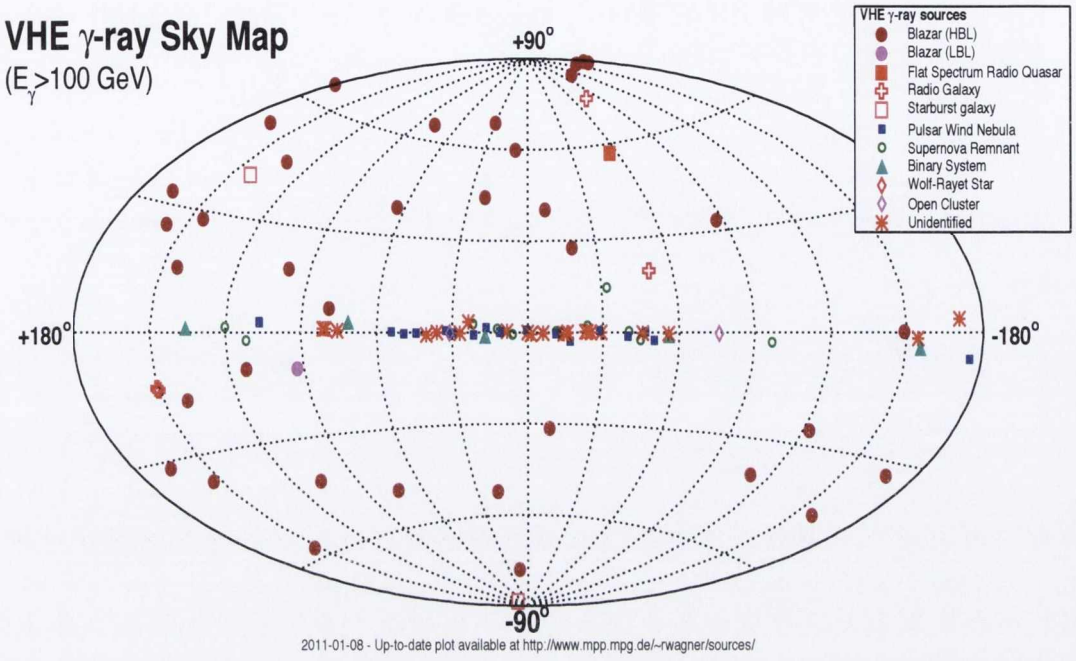

Figure 1.5: *Map of all known VHE γ-ray sources.*

1.1.4 Sources of VHE γ-rays

Many astrophysical sources have been proposed, which could give rise to relativistic particle populations and quite a few of them have been detected in VHE γ-rays (see Figure 1.5). In the following paragraphs, only a few examples are discussed. One source type in particular, Active Galactic Nuclei, will be discussed in detail in Chapter 4.

Galactic Sources: As mentioned previously, Supernova Remnants (SNR) are natural candidates for the production of VHE γ-rays (Drury et al. 1994). Different phenomena are connected with SNRs: (i) *shells* — the shock between the ejected outer shell of the supernova and the surrounding medium. The detection of this source type was an important step towards unveiling the sources of cosmic rays (Aharonian et al. 2005c, 2006a, 2004b). (ii) *Pulsar Wind Nebulae* — The electron-positron wind of the pulsar, which caries almost the whole rotational energy of the pulsar, collides with surrounding matter. The resulting terminating shock accelerates particles to energies up to 100 TeV and beyond. The synchrotron emission of these electron leads to the formation of the so-called pulsar wind nebulae. The Crab Nebula is the most famous source of this type, but others have also been discovered. The Galactic Plane survey, conducted by the H.E.S.S. experiment, was extremely fruitful in this regard (Aharonian et al. 2005a, Aharonian et al. 2006b).

Other Galactic sources which are not related to SNR, include micro-quasars, x-ray binaries and young open star clusters.

Extragalactic sources: About 50 extragalactic sources have been detected in the very high energy (E > 100 GeV) domain so far, the vast majority of which are classed as active galactic nuclei. The majority of these AGN are blazars, along with four radio galaxies established to be VHE γ-ray emitters: M 87 – see Figure 1.6 (e.g. (Aharonian et al. 2003b)), Cen A (Aharonian et al. 2009c), NGC 1275 (Aleksić et al. 2012), and IC 310 (Aleksić et al. 2010b); and two starburst galaxies have been discovered, NGC 253 (Acero et al. 2009) and M 82 (VERITAS Collaboration et al. 2009).

AGN harbour a massive black hole, surrounded by an accretion disk and sometimes a dusty torus. The production of VHE γ-rays is most likely linked to relativistic outflows (jets) from these objects. Further possible sources include massive galaxy clusters, as well as galaxies with high star-formation rates (starburst galaxies). A more detailed discussion of the VHE γ-ray production mechanisms in TeV Blazars, a sub-class of AGN, where a relativistic jet is directed towards the observer, will be given in the next section.

1.2 Active Galactic Nuclei (AGN)

In general, the term Active Galactic Nuclei refers to the intense emission from the central region of active galaxies, which cannot be attributed directly to stars. This central core often produces more radiation than the rest of the entire galaxy. The theory and classification of AGN has evolved and developed very much over the past number of years. Most of these divisions and classifications are due to historical reasons. The case of quasars is a prime example. Quasars were first observed in the radio waveband and because they were at very large distances, only the star-like nuclear source was seen. Due to their small angular size and relative faintness, these sources were labelled "quasi-stellar" objects. In general however, AGN are characterised by very bright, highly variable, non-thermal emission spanning the entire electromagnetic spectrum, from radio to TeV γ-rays.

The current thinking is that the pointing direction of the AGN (i.e. the angle at which we view them) is more important than the differences in the intrinsic physical properties, due to the strong anisotropic radiation patterns we observe. AGN with relativistic jets close to the line of sight are known as Blazars.

AGN occur in about 5% of all observed galaxies characterised by compact luminous centres (active nuclei), jets and very strong non-thermal activity. Theory suggests that there is a super-massive black hole (SMBH); ($\sim 10^6 - 10^{10} M_\odot$) at the centre of the AGN (Urry & Padovani

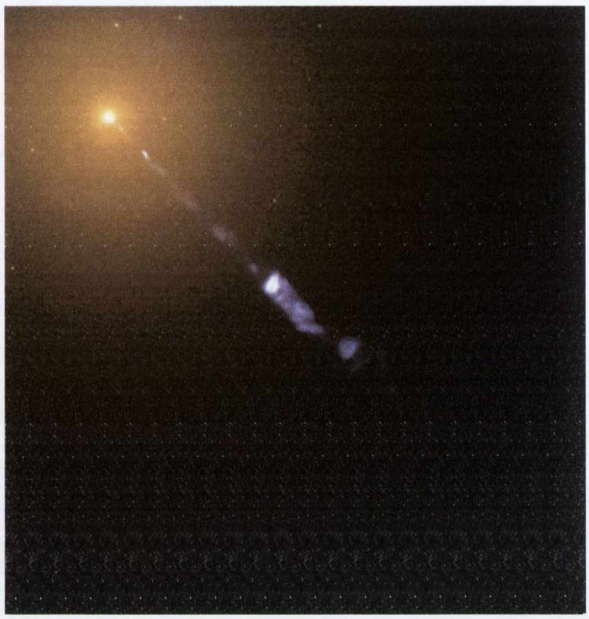

Figure 1.6: *The plasma jet emanating from the core of M87, taken from the Hubble Heritage Team (http://heritage.stsci.edu/).*

1995). This central black hole is surrounded by an accretion disk formed by hot ($\sim 10^5 K$) infalling material. The material in the accretion disk is heated up and emits black-body radiation peaking mainly in the ultra-violet waveband, another typical characteristic of these objects.

In about 10% of all AGN, collimated relativistic outflows of particles (known as relativistic jets) are seen, presumably along the magnetic field in the vicinity of the black hole and approximately perpendicular to the accretion disk and torus plane (see Figure 1.9).

In the unified model of AGN (Urry & Padovani 1995), the black hole is surrounded in the inner regions by an accretion disk and in the outer regions by a thick torus of gas and dust.

1.2.1 The Unified Model of Active Galactic Nuclei

The unification scheme of AGN (Urry & Padovani 1995) suggests that the different emission properties of different AGN classes are caused by differences in the viewing angle of the observer, the accretion rate and the mass of the central black hole. In this unified scheme, the SMBH located in the central region accretes surrounding material, forming a disk of hot plasma. The thermal radiation produced in the accretion disc ionises the gas clouds close to the SMBH, forming the broad-line region (see Figure 1.10 for a schematic drawing.). As the broad-line emission region is close to the central black hole, moving at high velocities, its emission lines are widened due to the Doppler effect. Further away from the SMBH, slower moving gas clouds

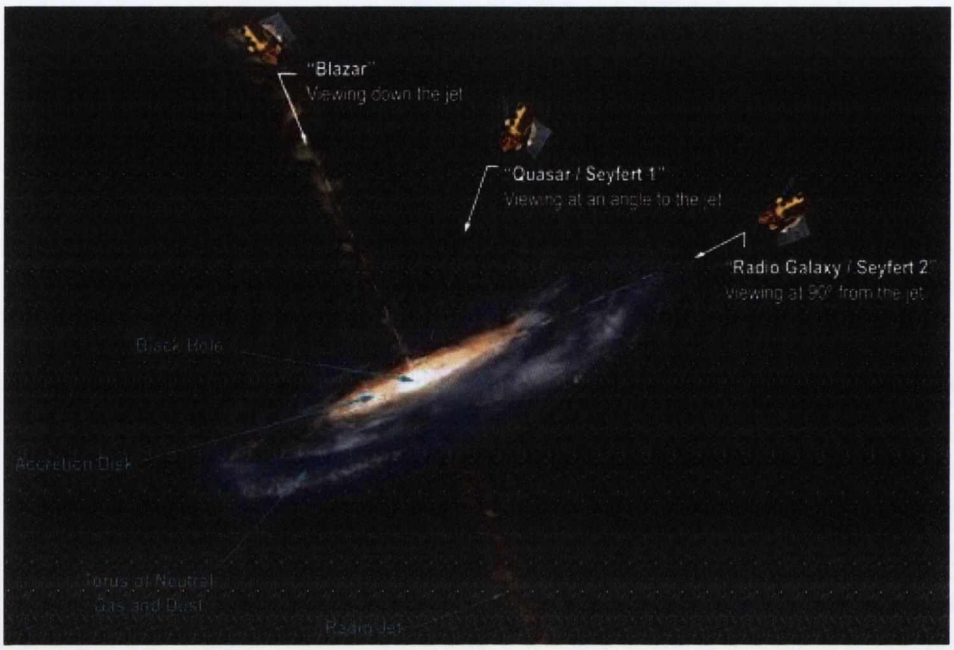

Figure 1.7: *Unified model of an active galactic nucleus. Image credit: Aurore Simonnet, Sonoma State University.*

produce the narrow-line absorption and emission spectrum of the AGN. The whole system is surrounded by a torus, which obscures the central part along the equatorial plane of the disc. If the accretion rate is high enough, a pair of collimated jets of ultra-relativistic plasma will appear in the direction perpendicular to the equatorial plane.

The jets emit polarised radio emission which is commonly interpreted as synchrotron radiation from relativistic electrons. Apparent superluminal motion (i.e. faster than light) of substructures (compact emission regions in the jet: knots) have been observed in several resolved jets (e.g. Pohl et al. 1995; Barthel et al. 1995), which is direct evidence for the relativistic bulk motion in the jets. X-ray emission from the accretion disk and from the jets is frequently observed.

1.2.2 Blazars

Blazars are AGN with a jet which is aligned close to the line of sight of the observer. It is widely believed that the relativistic jet is the key element of the observed non-thermal blazar emission. Acceleration processes in the jet generate non-thermal emission over an energy range spanning up to twenty orders of magnitude: from radio to TeV γ-rays. The jets appear to be stable up to Mpc scales and are often characterised by highly polarised radiation, short variability time-

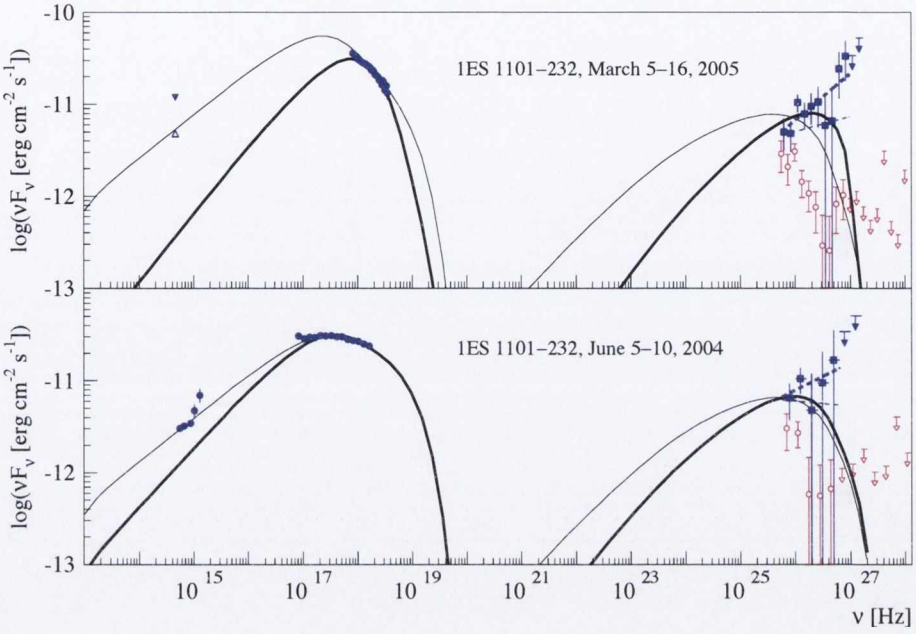

Figure 1.8: *Typical SED taken from blazar observations of 1ES 1101-232. First peak is X-ray data from the Rossi X-Ray Timing Explorer (RXTE). Second peak is from VHE band: red open symbols are the measured H.E.S.S. spectrum and the deabsorbed spectrum using a maximum Extragalactic Background Light (EBL) level are shown in blue squares (see Aharonian et al. 2007c).*

scales and an apparent superluminal motion (Fugmann 1988; Impey et al. 1991; Wills et al. 1992).

Doppler boosted radiation (where δ_j is the Doppler factor) is an effect predicted by the special theory of relativity. This effect enhances the radiation from material that is moving toward the observer at nearly the speed of light, and hides material moving in the opposite direction at such speeds. Doppler boosting ($\propto \delta_j^4$) combined with the orientation of the jets towards the observer make these objects excellent objects with which to study the underlying physics. The Doppler factor of the relativistic bulk motion is

$$\delta = \frac{1}{\gamma_{jet}(1 - \beta cos\theta)} \tag{1.5}$$

where $\beta = V_{bulk}/c$, and the bulk relativistic Lorentz factor $\gamma_{bulk} = 1/(1 - \beta^2)^{1/2}$. The relativistic beaming also contributes to overcoming the internal absorption of γ-rays by reducing the intrinsic luminosity of the source and allowing intrinsically larger emitting zones.

To explain the observed broadband spectrum of blazars, most models assume that a relativistic population of electrons and protons (or both) are accelerated within the jet. The spectral

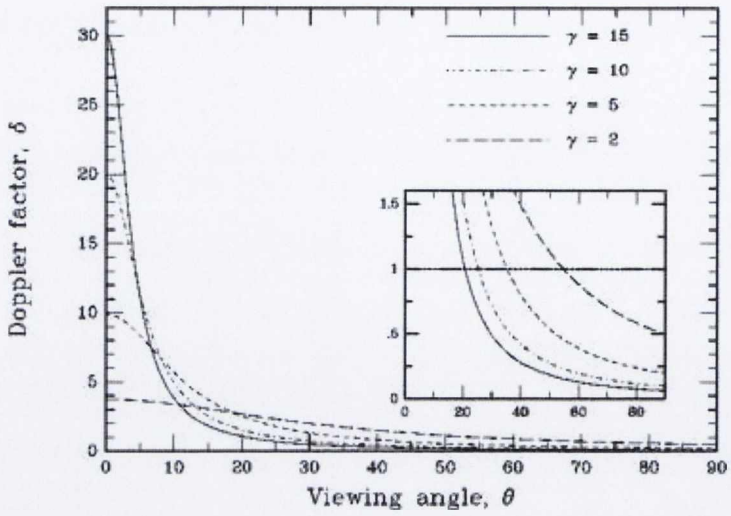

Figure 1.9: *The dependence of the Doppler factor on the angle to the line of sight. Different curves correspond to different Lorentz factors: from the top down, γ = 15, 10, 5, 2. The expanded scale on the inset shows the angles for which δ = 1 (Urry & Padovani 1995).*

energy distributions (SED) of blazars are characterised by two peaks, one at optical to X-ray energies and another at γ-ray energies (see Figure 1.8). For different objects, the peak energy of the lower and higher energy components can differ by several orders of magnitude. Additional emission at lower energies comes mainly from the stellar population of the host galaxy in the optical regime, as well as from extended jets, lobes and hot spots in the radio range.

1.2.2.1 BL Lac objects

BL Lac objects are a subgroup of AGN which were originally named after the prototype of the class BL Lacertae, which were originally identified as a new class of highly variable star. BL Lac objects are distinguished by the absence of strong emission or absorption lines in their spectra. BL Lac objects are believed to be AGN with the jet pointing in the direction of Earth, and are a sub-population of blazars. They show extremely variable emission in most wavelength bands and on short time-scales, which is attributed to emission processes connected to the relativistic jets. Depending on the position of the first peak of the broadband spectral energy distribution (SED), they are classified as either low frequency peaked BL Lac (i.e. peaked in the UV/optical: LBL) or high frequency peaked BL Lac (peaked in the X-rays: HBL). This classification is mostly historic, since there is a smooth transition between the two classes.

Monitoring of bright AGN led to the discovery of flux variability down to minute timescales, never before detected in active galactic nuclei and put new constraints on the physical mechanisms at work (Aharonian et al. 2007b; Albert et al. 2007b). All known extragalactic sources of

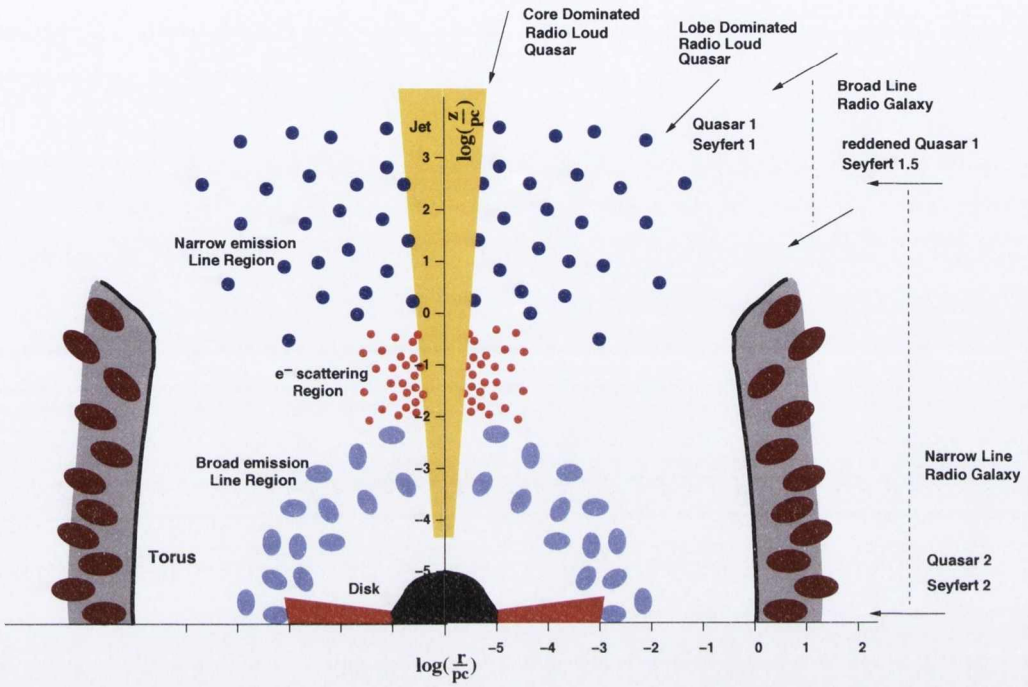

Figure 1.10: *Schematic drawing of the morphology of an AGN (Biermann et al. 2002).*

VHE γ-ray emission, with the exception of the radio galaxies M 87 and Cen A, belong to the class known as blazars. Radio galaxies have a much higher space density than blazars and their detection is less affected by their alignment to the line of sight. VHE studies of radio galaxies are therefore likely to contribute significantly to a better understanding of AGN unification schemes.

1.2.3 AGN Emission Models

Both leptonic and hadronic scenarios are widely used to describe the radiation processes in the VHE domain. However, in all accepted scenarios, the SED of blazars is described by the emission produced inside their jets. The relativistic beaming inside the jet is key to explaining the short timescale variations, as well as the high luminosity and energies of the emitted radiation. Nevertheless, a complete picture of the emission mechanisms is still a matter of debate. Since the primary accelerated particles responsible for the emission can either be electrons and positrons, or hadrons, the models are categorised as leptonic and hadronic and are described below.

1.2.3.1 Leptonic Models (EC, SSC)

Electrons accelerated within an astrophysical object will gyrate around the source's magnetic field lines, emitting photons. This process is known as synchrotron radiation and results in a population of photons ranging from radio to X-ray energies. High Energy (HE) photons in the X-ray to γ-ray regime are produced when low energy photons get an energy boost by interacting with a relativistic electron via Inverse Compton (IC) scattering. In such leptonic models, a highly relativistic and compact electron population are accelerated in the inner parts of the jet, moving down the jet with a bulk Lorentz factor Γ.

In the external Compton (EC) model, the electrons interact with photons from the accretion disk (Dermer et al. 1992), rescattered accretion disk photons (Sikora et al. 1994) or photons from the cosmic microwave background (CMB). EC models have been successfully used to describe the SED of Flat Spectrum Radio Quasars (FSRQ). In the case of BL Lacs however, the absence of strong emission lines in the optical band is usually interpreted as evidence that the ambient photon fields are not important, favouring the interpretation of their emission in terms of synchrotron self Compton (SSC) models.

The simplest realisation of leptonic emission is the so-called synchrotron self Compton model. In this scenario, the electrons produce synchrotron radiation in a random magnetic field and then IC upscatter the synchrotron photons to very high energies (Jones et al. 1974; Konigl 1981, Hartman et al. 1996). The result is a double peaked SED with a synchrotron bump in the optical to X-ray region and an IC bump in the hard X-ray to VHE region. The peak positions are coupled and depend mainly on the properties of the underlying electron population, the Doppler factor and the magnetic field.

If only one emission region is assumed and the electron population is homogeneous the model is called the *homogeneous one-zone SSC* model. If several emission regions are considered, usually assumed to be independent from each other, the model is labeled a *multi-zone SSC* model. One can combine the EC and SSC models by adding external photon fields to the SSC model.

The *homogeneous one-zone SSC* model has been very successfully utilised to describe the multi-wavelength data from different TeV blazars (Aharonian et al. 2005b; Albert et al. 2007a). Due to the close coupling of the synchrotron and the inverse Compton photons through the same electron population, a close correlation between the two emission components is expected. In general, leptonic models can explain many of the features observed in TeV blazars.

1.2.3.2 Hadronic Models

Hadronic models assume that a high energy protonic component contributes to the high energy bump, while the low energy bump is explained by synchrotron radiation of co-accelerated electrons. The energy of relativistic protons can be converted into high energy radiation via the following processes: direct synchrotron radiation of protons, photo-meson production ($p + \gamma \longrightarrow p + k\,\pi$) and nuclear collisions ($p + p \longrightarrow \pi + X$). The first two processes are known to be very inefficient, and they are only important in AGN jets for proton energies larger than 10^8 – 10^{10} GeV. Energy losses of such energetic protons are dominated by photo-meson production. This process was used to explain γ-ray production in blazars with the so-called "proton-induced cascade model" (Mannheim & Biermann 1992). In this model, the target radiation for photo-meson production is dominated by near/mid-infrared radiation. In blazars, such radiation can be emitted by hot dust at distances of $\sim 1 - 10$ pc from the central source and/or by synchrotron radiation due to relativistic electrons in the jet. The main outputs of the photo-meson processes are pions. Pions take about 1/3 of the proton energy and convert it to photons, neutrinos, and, through muons, to electrons and positrons. The photons injected by neutral pions immediately interact with low energy photons producing electron-positron pairs. Most of this radiation is so energetic that it produces two more generations of photons and pairs.

The more complex hadronic models are able to reproduce the observed properties of TeV blazars, although generally more fine tuning of the parameters is needed than in the simple SSC model (high Doppler factors, high magnetic fields, very high energy protons, etc).

A key way to differentiate between hadronic and leptonic TeV blazar models lies in the neutrino component, which can only arise in hadronic models. Future observations with neutrino telescopes such as IceCube (Karle et al. 2003) and KM3NeT (Katz 2006) will help to constrain or confirm hadronic models. The detection of neutrinos from blazars would clearly favour hadronic models.

1.2.4 Detected TeV Blazars

The sample of AGN detected at VHE energies currently includes 45 published sources, ranging in redshift from $z = 0.0018$ to $z = 0.536$ (see Figure 1.11). The VHE spectra of most sources can be described by simple power laws, with an observed photon index between 1.9 and 4.6. Sources can show quiescent, low and highly active (flaring) energy states. Flux variability is frequently observed, despite sparse time coverage for many sources. Variability has been detected on all time scales: years, months, days, down to the minute scale for three flaring sources.

Since the discovery of the first TeV blazar Mrk 421 in 1992 (Punch et al.), the number

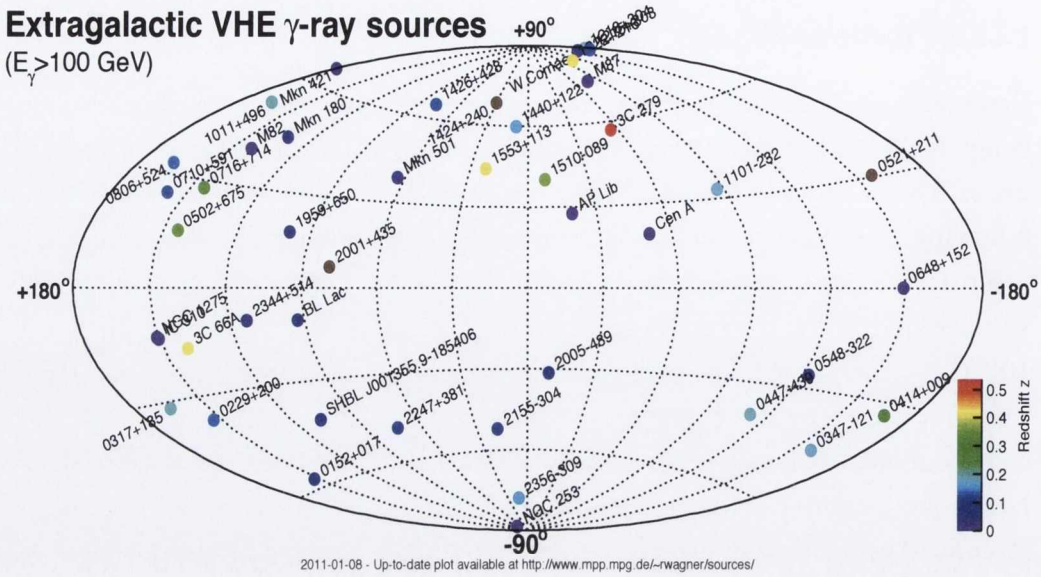

Figure 1.11: *Map of all known extragalactic γ-ray sources, with the redshift labelled by colour.*

of extragalactic VHE γ-ray sources has steadily increased. With IACT experiments such as H.E.S.S. and MAGIC, as well as the *Fermi* Gamma-ray Space Telescope, the number of known TeV blazars has increased dramatically.

From the recent *Fermi* LAT Second Source Catalogue, the number of AGN observed was at a count of 806 (being 44% of the total number of sources), with another 257 candidate AGN (14% of the total) observed (The Fermi-LAT Collaboration 2011).

1.2.4.1 AGN with H.E.S.S.

Essentially all AGN detected at very high energies are High Frequency Peaked BL Lac objects, due to selection effects. Approximately 30% of the H.E.S.S. observation schedule is dedicated to the study of AGN, mainly Blazars.

So why are AGN considered potential sources of pair halo production? AGN show spectra with no clear upper energy cutoff and may well have emission extending into the very high energy domain. If we have γ-rays in the VHE regime, this will lead to interactions with the diffuse intergalactic radiation fields, which in turn will produce a pair cascade, leading to the formation of a Pair Halo. With H.E.S.S. we have a collection of ~40 AGN in our internal source catalogue, with redshifts varying between 0.001 (Cen A) up to 0.5 (3C279). Using these very powerful extragalactic objects, we hope to learn more about extended pair halo emission. It can

act as a powerful probe for EBL evolution, intergalactic magnetic field strengths, to constrain the total VHE luminosity and source duty cycle of these sources.

1.3 The *Fermi* Gamma-ray Space Telescope

Although the main body of work presented in this thesis is the study of H.E.S.S. observations, the opportunity to profit from non-proprietary *Fermi* observations could not be overlooked. A brief description of this highly successful instrument is given below with analysis results provided in Chapter 5.

Before the launch of the *Fermi Gamma-ray Space Telescope* (FGST, formerly GLAST) in May 2008, high energy (HE) space-based γ-ray astronomy has been dominated by the results obtained with the EGRET telescope aboard the Compton Gamma Ray Observatory. Because of the rather modest angular resolution of EGRET (in the order of a few degrees), only two source populations - AGN and pulsars - have been clearly identified as high energy γ-ray emitters. With the *Fermi*-LAT (Large Area Telescope), HE γ-ray astronomy entered a new era. This instrument, which in comparison to EGRET, has a significantly improved angular resolution (0.6° at 1 GeV and better than 0.15° at energies above 10 GeV) and flux sensitivity (better than 10^{-12} erg/cm2s), is a perfectly designed tool for deep γ-ray surveys with an effective field of view in the order of 2 steradian (which proves useful in comparison to the narrow field of view allowed by ground based instruments.)

Over the last three years, *Fermi*-LAT (Figure 1.12) has been releasing vast amounts of important astronomical information. These results confirm, to a large extent, the optimistic pre-launch expectations concerning, in particular, the dramatic increase of the number of γ-ray emitting pulsars and AGN, discovery of new classes of compact / variable and *extended* galactic and extragalactic γ-ray sources, the detection of multi-GeV components of GRBs, etc.

The second *Fermi* LAT gamma-ray source catalogue The Fermi-LAT Collaboration (2011), based on the first two years of observations, consists of almost 2000 galactic and extragalactic γ-ray emitters. While more than half of these objects are associated with counterparts representing known source populations (more than one hundred sources being firmly identified), the origin of approximately 1/3 of these objects remains an open issue. This concerns, first of all, extended sources located in the galactic plane, e.g. SNRs and Pulsar Wind Nebulae, for which the chance of confusion with the diffuse emission of the galactic disk is especially high. Because of the limited angular resolution, the most reliable approach for identification of HE γ-ray sources is the analysis based on temporal studies. The periodic character of γ-ray emission the galactic binary systems or the sporadic flares of AGN provide a useful tool for the identification of

variable γ-ray sources based on simultaneous observations in different energy bands. In general, multi-wavelength observations are a key component for the identification of γ-ray emitters, as well facilitating a deeper understanding of the nature of these objects.

Figure 1.12: *Artist's impression of the Fermi Gamma-ray space telescope (Courtesy of NASA).*

With this in mind, a search for extended blazar emission with high energy data from the *Fermi*-LAT is conducted and the results are presented in Chapter 5.

The remainder of the thesis is structured as follows. *Chapter 2* provides a brief overview of the H.E.S.S. experiment, the Imaging Atmospheric Cherenkov technique, as well as the basic principles of the analysis methods. The new addition to the H.E.S.S. system, HESS II is also briefly described.

Chapter 3 presents the theory behind pair halos and beam broadened cascade emission. The physical processes are outlined, as well as the importance of the Extragalactic Background Light (EBL) and the Intergalactic Magnetic Fields (IGMF) in this study. A summary of the Monte Carlo simulations are described.

In *Chapter 4*, the three γ-ray sources studied in detail during the course of this work are presented, justifying their suitability for this search. These sources include 1ES 1101-232, 1ES 0229+200 and PKS 2155-304. A thorough H.E.S.S. analysis is presented.

The results from a specialised analysis searching for extended blazar emission are reported in *Chapter 5*, using H.E.S.S. and *Fermi*-LAT observations. Upper limits on pair halo emission

and constraints on the IGMF are presented. This chapter is based on a publication currently undergoing the H.E.S.S. internal review process.

Finally, in *Chapter 6*, theoretical constraints and the future prospects for this work are explored. The potential of the next generation Cherenkov Telescope Array (CTA) is discussed, with the results from simulations included. Recent results from updated Monte Carlo simulations for pair halos are presented, as well as a proposed candidate for future observations. Conclusions and a concise summary of this work can be found at the end of this chapter.

2

Imaging Atmospheric Cherenkov Telescopes

The most successful experimental technique, to date, for the detection of VHE γ-rays is the ground-based imaging atmospheric cherenkov technique. Although it is possible to detect cosmic γ-rays with space-based experiments, such as the *Fermi* Gamma-ray space telescope, these instruments are only competitive for γ-ray energies of up to 300 GeV. Higher energy photons are exceedingly difficult to detect with the few square metre detection areas allowable with satellite experiments, due to the steep decline of the γ-ray flux with energy. For higher energies, another method must be utilised. Fortunately, γ-rays of higher energies interact with the Earth's atmosphere, allowing indirect measurements to take place. The Cherenkov Technique is one such method of indirect detection, which records the images of air showers which are produced by the interaction of these initial γ-rays in the atmosphere.

2.1 Air Showers

High energy particles ($\gtrsim$ 50 GeV) coming from outer space will interact with the Earth's atmosphere to produce a cascade of secondary particles known as an Extensive Air Shower (EAS).

There are two different types of air shower, depending on the type of primary particle: elec-

tron or photon vs hadronic shower. Hadronic cosmic rays dominate the γ-ray signal by a factor of 10^3, even for the strongest γ-ray sources (e.g. the Crab Nebula). In the work of Hillas (1985, 1996), an analysis of simple image parameters can lead to an efficient hadronic-background separation, which was demonstrated by the detection of the Crab Nebula by the Whipple telescope (Weekes et al. 1989). The separation is based on the difference between an image of a (hadronic) cosmic-ray induced shower and a γ-ray induced (electromagnetic) shower and these differences are described below.

Electromagnetic Air Showers

Electromagnetic showers are initiated by electrons or photons. A γ-ray of sufficient energy entering the atmosphere will interact within the Coulomb field of an atmospheric nucleus to produce an electron-positron (e^+e^-) pair. Successive bremsstrahlung and pair production processes sustain the electromagnetic cascade. The leptons created will then be deflected by close-by nuclei and emit high energy photons (bremsstrahlung). These two processes dominate the propagation of the air shower mainly along the primary particle's initial course, as the secondary particles are emitted with minimal transverse momentum. The maximum number of particles is directly proportional to the energy of the primary particle. The height at which this maximum is reached however, depends logarithmically on the primary particle energy. Figure 2.1 (left panel) shows schematically these initial stages in the development of a photon induced EAS.

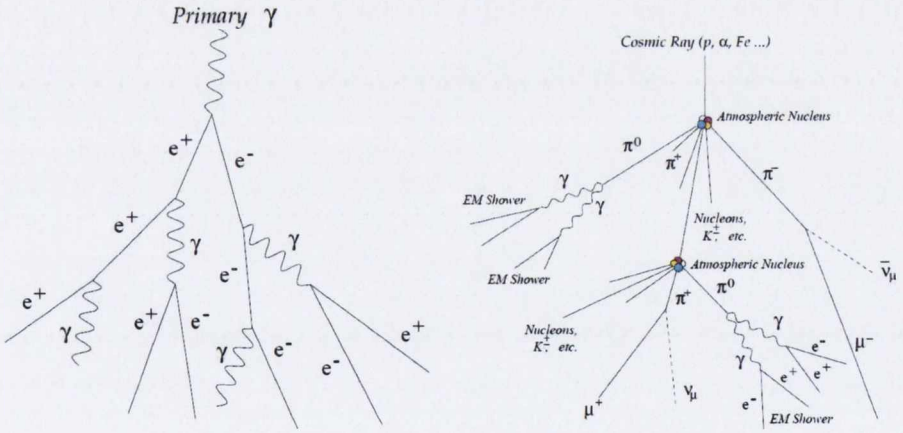

Table 2.1: *Schematic illustration of the development of an extensive air shower: induced by a γ-ray (left) and induced by a charged cosmic ray (right). Taken from Paneque (2004).*

As the cascade develops, pair production and radiation continue and the number of γ, e^+ and e^- grows exponentially around the forward direction of the original γ-ray, sharing out its total energy. Multiple Coulomb (elastic) scattering of the electrons and positrons deflects the sec-

ondary particles away from the direction of the primary photon, or shower axis. This scattering is more severe than the angular deviations introduced into a particle's path by bremsstrahlung and pair production and therefore dominates the lateral distribution of particles at a given height. The influence of geomagnetic deflections impact some shower observables, for example, the lateral distribution of muons in the case of events with large zenith angles (larger than 75 degrees) but do not play a dominate role (see Cillis & Sciutto (2000) for further details).

The particles form a disk a few metres thick that propagates through the atmosphere at a speed close to c. At a critical energy, E_c ($\sim$ 83 MeV in air), an electron loses equal amounts of energy per radiation length by the processes of ionisation and radiation. In addition the mean photon energy drops towards twice the rest mass of an electron. The cross-section for pair production becomes approximately equivalent to that for Compton scattering and, at lower energies, photoelectric absorption. Thus the shower reaches a maximum development at E_c. At larger depths the number of particles falls off and the shower is exhausted. A description of bremsstrahlung, pair production, elastic scattering, ionisation, and Compton scattering may be found in many texts including Williams (1991). As an illustration, a vertically incident 1 TeV γ-ray initiated EAS reaches a maximum of $\sim 10^4$ particles at $\sim$ 350 g cm^{-2} ($\sim$ 8 km above sea level). Monte Carlo simulations such as *CORSIKA* (Heck et al. 1998) have provided the most complete study of air showers.

Hadronic Air Showers

The shower development for hadrons hitting the Earth's atmosphere differs from the shower development for photons and electrons. These particles, most of which are protons, collide with an atmospheric nucleus, producing secondary particles which in turn interact – giving rise to a hadronic cascade as show in Figure 2.1 (right panel). At each successive generation approximately half of the available energy continues in nuclear particles, the bulk of which is carried by a single leading nucleon along the shower axis. The balance of the incident energy produces pions and kaons.

The interaction of relativistic hadrons with matter and photons results not only in the production of neutral pions but also in a population of charged pions which decay primarily into muons and muon neutrinos (with a likelihood of $> 99.98\%$). The muons then decay to electrons and electron neutrinos as shown below.

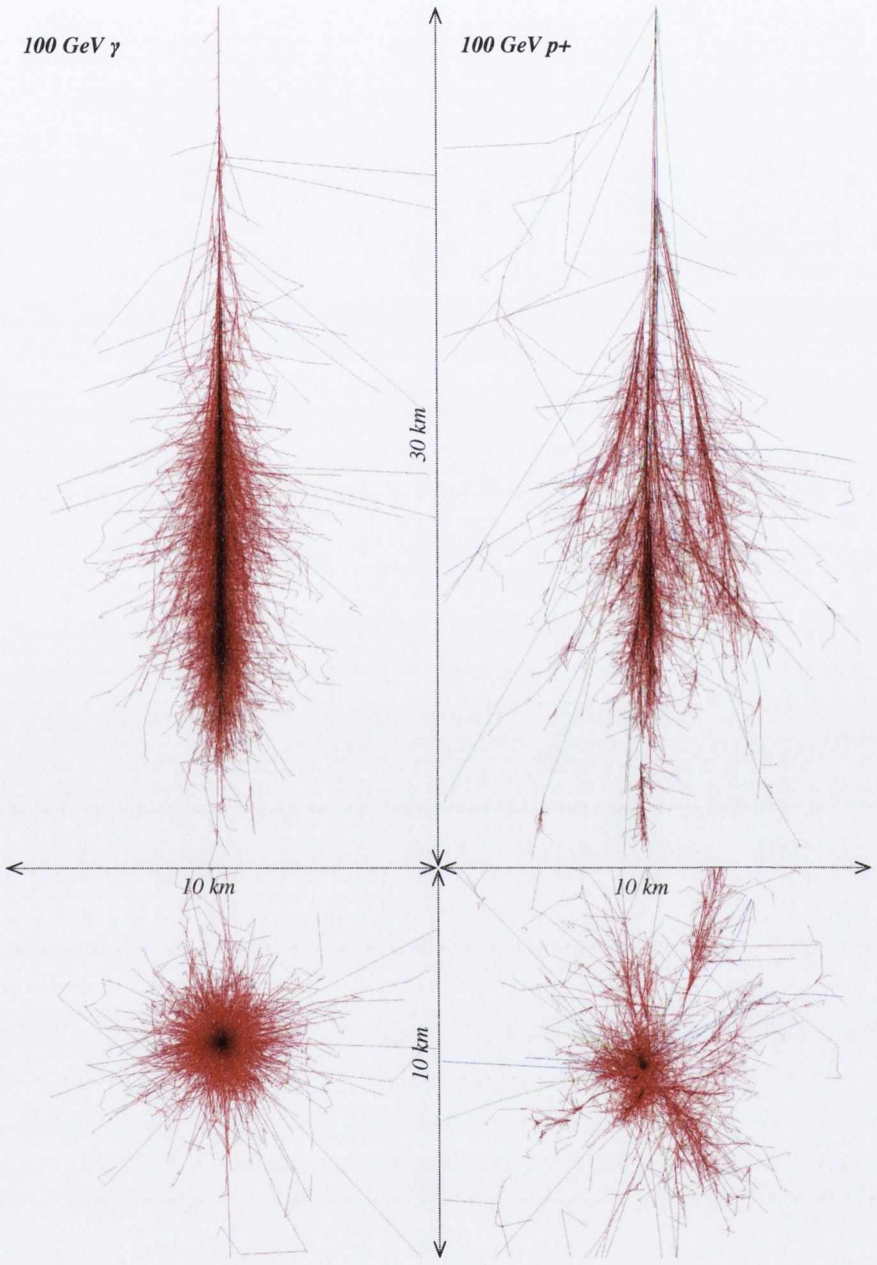

Figure 2.1: *The development of 100 GeV γ-ray (left) and 100 GeV proton (right) induced air showers. The upper panels show the longitudinal development of a cascade, and the lower panels the lateral distribution. These images were produced using CORSIKA with a fixed interaction height of 30 km above sea level. Red tracks are used to indicate electrons, positrons and γ-rays. Adapted from F. Schmidt, "CORSIKA Shower Images", http://www.ast.leeds.ac.uk/~fs/showerimages.html.*

$$\begin{aligned} \text{hadrons} \rightarrow \pi^+ &\rightarrow \mu^+ + \nu_\mu \rightarrow \mathrm{e}^+ + \nu_\mu + \bar{\nu}_\mu + \nu_\mathrm{e} \\ &\rightarrow \pi^- \rightarrow \mu^- + \bar{\nu}_\mu \rightarrow e^- + \nu_\mu + \bar{\nu}_\mu + \nu_e \end{aligned} \tag{2.1}$$

Although simple models of hadronic showers are available, complex Monte Carlo simulations provide the best models of hadronic interactions.

Due to the distinct interaction processes, hadronic showers exhibit different characteristics than their electromagnetic counterparts:

- While complex multi-particle processes occur in hadronic showers, electromagnetic showers are dominated mainly by simple three-particle processes. As a result, hadronic showers are less regular and exhibit larger fluctuations than electromagnetic showers.

- Due to the large transverse momentum of secondary particles produced in strong interactions, hadronic showers exhibit a far greater lateral spread than seen in electromagnetic showers.

- The mean free path within the atmosphere is far greater for protons than for γ-rays (of about a factor of 2). Consequently, hadronic showers penetrate deeper into the Earth's atmosphere. The interaction length of a proton in air is ~ 80 g cm^{-2} compared to ~ 36 g cm^{-2} for a γ-ray.

- A large fraction of the primary hadron energy is lost from the hadronic shower through the production of long-lived muons and neutrinos, as well as from dissipation in nuclear interactions. Despite the efficient energy transfer from the hadronic to electromagnetic component, a hadronic shower contains three times less particles in the electromagnetic component than a γ-ray induced one, given the same primary particle energy.

2.1.1 Cherenkov Radiation

A charged particle moving inside a transparent dielectric medium at a velocity $v = \beta c$, i.e. travelling faster than the speed of light in air, will emit Cherenkov light when $\beta > 1/n$, where c is the speed of light in a vacuum and n is the refractive index of the medium. This radiation, now known as Cherenkov radiation was discovered by P.A. Cherenkov in 1934 with details given in (Cherenkov 1935) and a theoretical explanation later given by Tamm & Frank (1937).

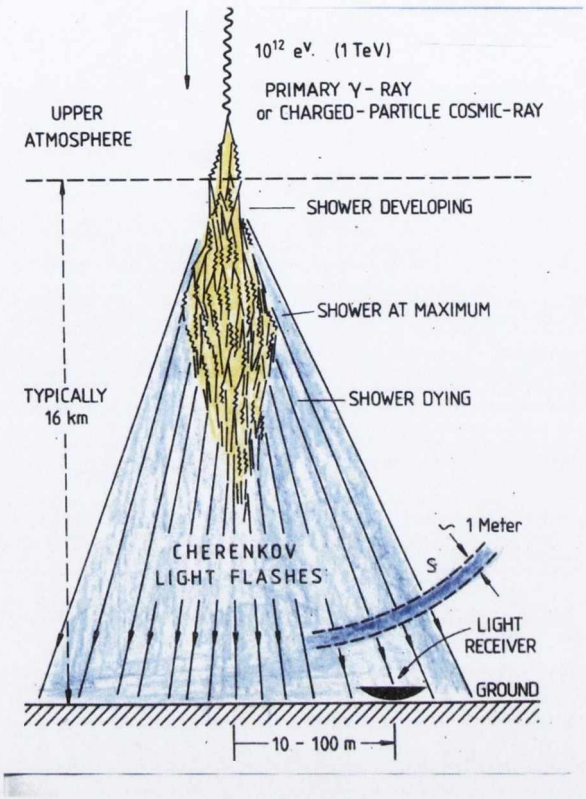

Figure 2.2: *Schematic of an extensive air shower. Image credit : Trevor Weekes*

As the particle travels, it disrupts the local electromagnetic field in the surrounding medium. The Cherenkov wave front propagates at a fixed angle with respect to the charged particle's trajectory, given by :

$$\cos\theta = \frac{1}{\beta n} \tag{2.2}$$

It is apparent that the maximum emission angle occurs when the particle is ultra relativistic and $\beta = 1$, given by $\theta_{max} = \cos^{-1}(1/n)$. In air at sea level, this corresponds to values of $n = 1.00029$ and $\theta_{max} = 1.3°$ respectively. The minimum particle energy required for the production of Cherenkov light is given by :

$$E_{min} = \gamma_{min} m_0 c^2 = \frac{m_0 c^2}{\sqrt{1 - 1/n^2}} \tag{2.3}$$

where m_0 is the rest mass of the charged particle. The threshold energy for electrons, muons and protons is 21 MeV, 4.4 GeV and 39 GeV in air at sea level.

The total number of electrons at the cascade maximum is closely proportional to the primary energy and the atmospheric depth of this maximum increases logarithmically with energy. The

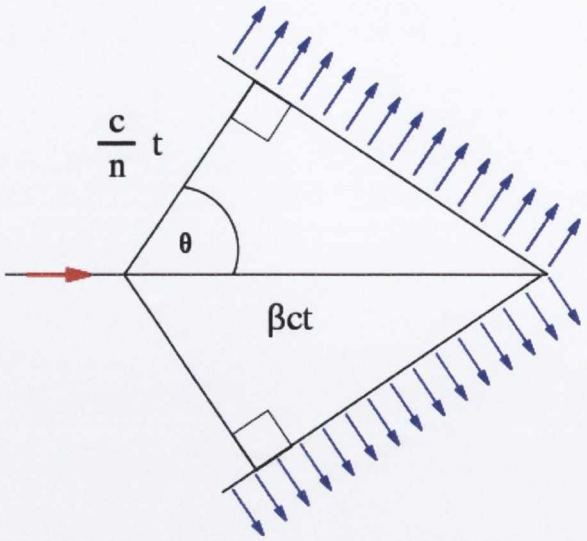

Figure 2.3: *The geometry of the Cherenkov radiation (shown for the ideal case of no dispersion). Image credit: Arpad Horvath*

duration of the Cherenkov flashes from air showers is of the order of a few nano-seconds. The ability to observe these short flashes depends on the weather conditions and the background light characteristics of the atmosphere. Aerosols like clouds or dust can scatter and absorb the light. A bright night sky can make the observation of Cherenkov light impossible. For optimal detection conditions, a dark and remote site with excellent weather conditions is needed.

Air showers from particles with energies in the GeV to TeV domain are compact. For a 1 TeV photon-initiated shower, the maximum of the air-shower occurs at a depth of ~300 g cm^{-2} or at 10 km above sea level for a vertically incident photon, to an opening angle of ~ 1° (see Figure 2.3). The light is collimated around the major axis of the cascade and the Cherenkov photons thus irradiate only a small "light pool" on the Earth's surface, which has a typical radius of ~120 m for a vertical event.

2.2 The Imaging Atmospheric Cherenkov Technique

This technique is very effective, as it utilises the Earth's atmosphere as a calorimeter and a particle detector. High energy photons (> GeV) on entering the Earth's atmosphere initiate an electromagnetic cascade, via the process of electron pair production and subsequent bremsstrahlung. Hence, for γ-rays of 10 GeV or larger, on hitting the Earth's atmosphere the γ-ray is effectively replaced by two charged particles travelling in almost the same direction as the γ-ray.

The two main components of an imaging Cherenkov telescope are 1) the reflector, which collects and focuses the light, and 2) the camera. The energy threshold of the telescopes is determined mostly by the size of the reflector. Less energetic particles will produce smaller air showers and therefore less Cherenkov light, so larger light collecting areas are needed. It is possible to lower the energy threshold further by using photo-multiplier tubes with higher quantum efficiencies or by locating the telescope at higher altitudes (i.e. closer to the shower maximum).

The camera is located in the focal plane of the reflector and consists of a number of fast and sensitive photon detectors used for the detection of the short blue Cherenkov light flashes. The imaging technique is based on the practise of recording an image of the Cherenkov light emitted in an air shower.

The major advantage of this technique with respect to other ground-based approaches is the precision with which the properties of the primary γ-ray can be reconstructed. Images of the shower events in the camera plane are, after calibration, analysed to retrieve information about the energy and direction of the primary γ-ray.

2.3 The High Energy Stereoscopic System (H.E.S.S.) and Analysis Methods

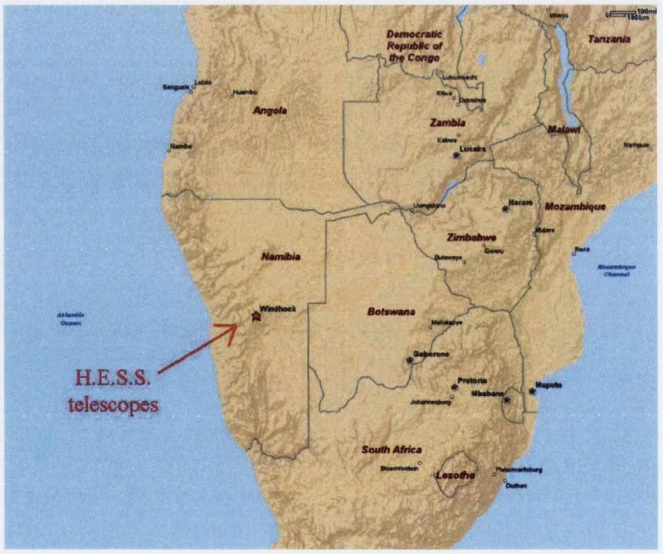

Figure 2.4: *Location of the H.E.S.S. site in Namibia, South-West Africa.*

The H.E.S.S. experiment has been in operation since June 2002 and is located in the Khomas

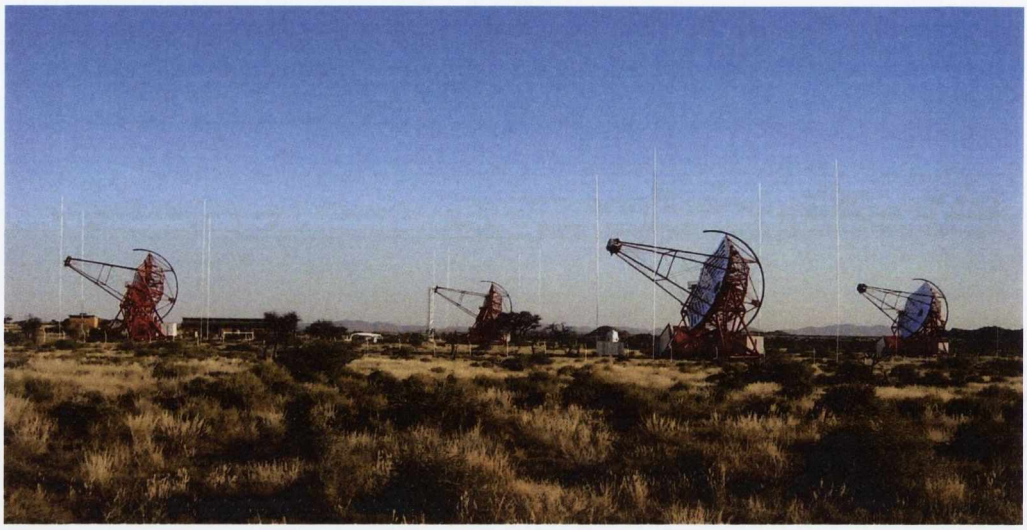

Figure 2.5: *H.E.S.S. array of four telescopes in Namibia. The new H.E.S.S. II telescope will be located in the centre of the array.*

Highlands of Namibia (23°16'18" S 16°30'1" E), 1835 m above sea level (see Figure 2.7). It is an array of four Imaging Atmospheric Cherenkov Telescopes (IACT) which detect cosmic γ-rays in the 100 GeV to 100 TeV energy range.

The H.E.S.S. system is characterised by a low threshold (~100 GeV) and high flux sensitivity resulting from good angular resolution and background rejection which we get from the stereoscopic technique. H.E.S.S. achieves an angular resolution of about 6 arcminutes per detected event and a point source sensitivity above 1 TeV of $< 2 \times 10^{-13} m^{-2} s^{-1}$ (or 1% of the flux from the Crab nebula) for a detection with statistical significance of 5 standard deviations in a 25 hour observation. The H.E.S.S. experiment, as well as the IACT technique has been well documented in a number of publications (Hinton 2009; Porter & Weekes 1977).

The key advantage of ground based instrumentation like H.E.S.S. is that it has a much bigger collection area in comparison to satellite based instruments such as *Fermi* and EGRET[1]. The typical effective collection area of a single Cherenkov telescope is 10^5 m^2, almost five orders of magnitude larger than can be realistically be achieved by direct detection in space. A summary of the basic properties of the H.E.S.S. system can be seen in Table 2.2.

The atmospheric Cherenkov imaging technique can be significantly improved by the use of multiple telescopes. In the case of stereoscopic observations, two or more telescopes are used to observe the air shower stereoscopically from different directions. Stereo detection allows for improved angular resolution and facilitates the improved rejection of background cosmic

[1]The Energetic Gamma Ray Experiment Telescope (EGRET)

Field of View (FOV)	$\sim 5°$
Direction Resolution	$0.1°$ per event
Energy Threshold (Zenith)	$\sim$ 100 GeV
Energy Resolution	$\sim$ 15 %
Sensitivity (5σ in 25 h)	$< 2 \times 10^{-13} m^{-2} s^{-1}$

Table 2.2: *Summary of properties of the H.E.S.S. experiment.*

ray showers. Multiple images of the same shower offer many advantages, including a reduced energy threshold by using a coincident trigger between telescopes, better angular resolution, determination of the shower maximum, elimination of the local muon background and pinpointing the shower axis location.

As previously stated, only secondary products of the primary particle can be recorded by IACTs. The main challenge therefore for IACTs is to fully reconstruct properties like type, energy and direction of the primary from the light of the Cherenkov air shower. The use of more than one telescope significantly improves the ability to reconstruct these properties as the shower can be recorded under different viewing angles. For γ-ray initiated showers the light yield at the ground is roughly proportional to the energy of the primary particle. γ-ray showers are observed against a background of much more numerous hadronic showers. This background can be greatly reduced using the morphology of air-shower images.

2.3.1 The Mirror System

The H.E.S.S. array is arranged in a square with 120 m sides, each telescope has a focal length of 15 m and a 13 m diameter. The reflectors consist of 380 quartz-coated round facets (60 cm diameter) arranged with Davies-Cotton optics (Davies et al. 1957), resulting in a total mirror area of 107 m^2 (Bernlöhr et al. 2003). The average reflectivity of the mirrors is $\sim$ 80% (for wavelengths above 330 nm). The individual mirrors can be moved by actuators, allowing for an automated mirror alignment. The alignment is performed by tracking a bright star with the telescope system and recording its image in the focal plane with a CCD camera mounted in the centre of the dish. Each mirror spot can be identified separately and can then be driven to its nominal position in the centre of the field of view.

2.3.2 The H.E.S.S. Camera

The cameras of the H.E.S.S. telescopes serve to capture and record the Cherenkov images of air showers. The cameras body of 1.4 m diameter houses the complete trigger and readout electronics, see Figure 2.10. Typical observations record images at a rate of 250 Hz while keeping

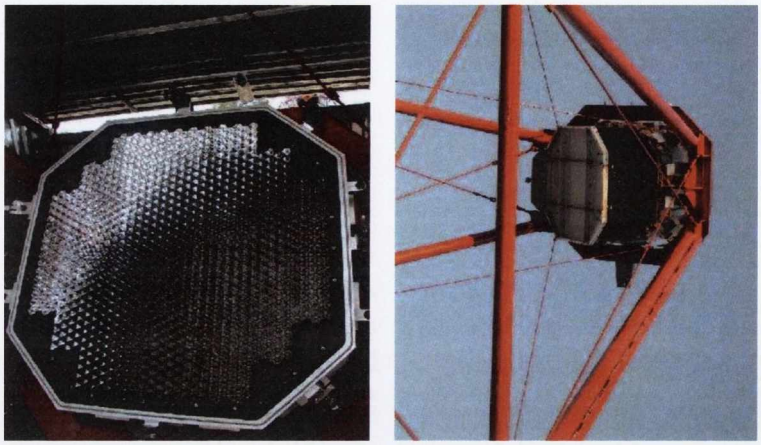

Figure 2.6: *Left: The front of the camera with the lid open showing the PMTs and the Winston light cones. Right: Camera shown with the telescope tracking and steel frame.*

the dead time below 10%. The design criteria of the camera include :

- a pixel size (0.16°) small enough to resolve image details.
- a large field of view (5° opening angle) to allow observation of extended sources.

In the case of H.E.S.S., an array of Photomultiplier Tubes (PMT) is used to record the Cherenkov light. This array consists of 960 PMTs (Photonics XP2960) in total, which are arranged in drawers of 16 PMTs each. Each pixel has a 0.16° angular size, which combined provides a total field of view of about 5°. Each PMT also has a Winston cone light collector, to increase the light collecting area in the camera plane. Individual photons are recorded using the PMTs with a quantum efficiency of $\sim$ 20%. The signal pulse from the PMT is fed into three different channels, one into the trigger channel of the camera and two into the acquisition system with different gains. By using a high gain and a low gain channel the linear response of the PMT is increased to a dynamic range of up to 2000 photoelectrons (p.e.).

2.3.2.1 Instrument Response

The camera response is monitored in the following way. The single photon-electron gain of PMTs is monitored by a LED system mounted in front of the camera. Differences between the PMTs of a camera (due to differences in quantum efficiencies of the PMTs and reflectivity of the Winston cones) are flat-fielded using a laser mounted on the telescope dish. Although some more details are provided in section 2.3.4. the calibration scheme is described in detail in

Figure 2.7: *A single drawer contains 16 PMTs and the associated electronics.*

Aharonian et al. (2004a).

The optical response of the instrument to Cherenkov light is affected by the reflectivity of the mirrors and the Winston cones, and also by the shadowing of the telescope masts. This response is monitored by studying Cherenkov light from single muons passing close to the telescope in dedicated Muon-runs in which no coincidence between telescopes is required. The analysis of muons in the determination of the telescope response is described in detail in Bolz (2004).

2.3.3 The Point Spread Function

The Point Spread Function describes the response of an imaging system to a point source or a point-like object. In general, this can be represented as :

$$\delta(x,y) \propto \int\int e^{j(k_x x + k_y y)} dk_x dk_y \tag{2.4}$$

The angular resolution of H.E.S.S. depends upon observation conditions (for example, the zenith angle), the analysis cuts applied and the reconstruction algorithm. The resolution of H.E.S.S. can be quantified by means of the γ-ray point spread function (PSF) given by the squared angular distance (θ^2) between the reconstructed and the true direction of a Monte-Carlo γ-ray point source. The H.E.S.S. PSF is well described by the sum of two Gaussians. A narrow one describes the narrow central peak and a broad Gaussian accounts for the exponential tail which originates from badly reconstructed events. The commonly quoted figure for the angular resolution is the 68% γ-ray containment radius R_{68}, the radius that encompasses 68% of the reconstructed γ-ray directions from a simulated point source. Unless otherwise stated, the Monte-Carlo simulated γ-rays used in this analysis to exemplify the performance of the system were simulated with an energy spectrum of a Crab-like photon index of 2.6 at a zenith angle of 20° .

The PSF is expected to broaden with increasing distance from the optical axis and to vary

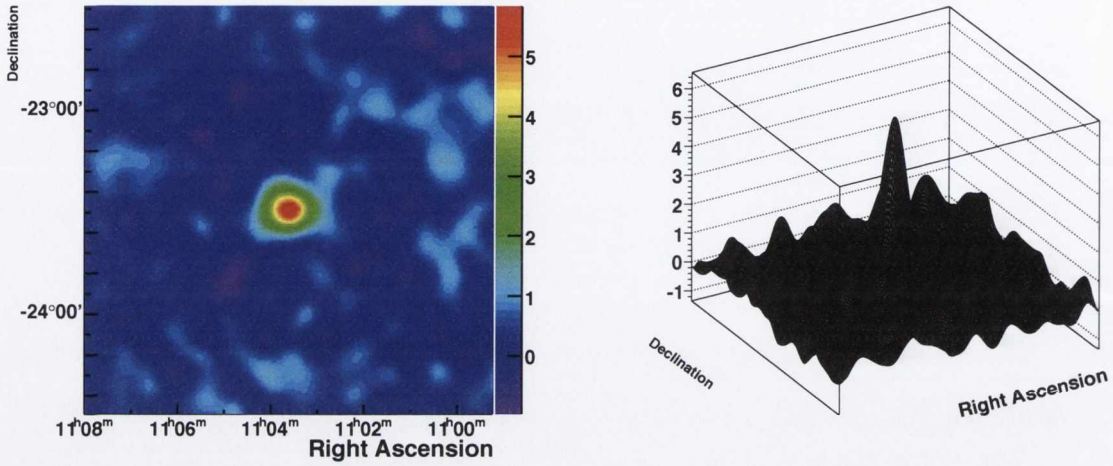

Figure 2.8: *Left: A two-dimensional (2D) skymap of the H.E.S.S. Point Spread Function for the source 1ES 1101-232. Right: The 2D PSF shown as a surface plot.*

slightly with elevation because of gravity-induced deformations of the dish. To describe the point spread function as a function of the angular distance θ to the optical axis around the mean alignment of 65°, characterised by the radius $r_{80\%}$ of a circle containing 80% of the light, the parametrisation :

$$r_{80\%}(\theta) = (r_\theta^2 + d_\theta^2 \theta^2)^{1/2} \tag{2.5}$$

is used. r_θ represents the on-axis width of the point spread function and d_θ the increase of the width per degree angular distance to the optical axis. The (on-axis) point spread function as a function of the telescope elevation Θ is characterised by :

$$r_{80\%}(\Theta) = (r_\Theta^2 + d_\Theta^2(\sin\Theta - \sin\Theta_c)^2)^{1/2} \tag{2.6}$$

where r_Θ is the minimum of the width and Θ_c its location in elevation; d_{Theta} specifies the increase of the width per 90° elevation.

The optical PSF of the resulting image by all mirrors in the focal plane is well contained within the camera pixel size of 2.8 mrad and with a value of 0.25 mrad on-axis well within its specifications. The optical PSF depends on the offset in the camera due to spherical aberrations of the reflector. Furthermore, it depends on the elevation of the telescope due to deformations of the dish structure but is for all practical observational pointing positions within the pixel size. This method has proven to be extremely successful, resulting in a point spread function well below the size of the camera pixel (Cornils et al. 2003).

The direction reconstructed PSF can be calculated for a fixed energy or averaged over a given energy range with an assumed spectral index. It can also be calculated over an energy range and a given distribution in zenith and offset, which was used in our analysis. In the most general case, the calculation of the averaged PSF for a given set of observation runs are as follows. Given the distribution of zenith angle ζ and offset angle δ, as well as the mean azimuth angle φ, telescope pattern p and optical configuration ϵ_{opt} for each run, the PSF can be calculated if a source spectrum $\phi(E)$ is assumed :

$$f(\theta^2) = \sum_{runs} \sum_{E} \sum_{x} N_{exp}(x, E) \cdot f(\theta^2, x, E) \tag{2.7}$$

where

$$N_{exp}(x, E) = \int_{E-\Delta E/2}^{E+\Delta E/2} \phi(E') A_{\text{eff}}(x, E') w(x) T \mathrm{dE} \tag{2.8}$$

Here, T is the livetime of the run, w is the fraction of livetime spent in each zenith/offset bin, $x \equiv (\zeta, \varphi, \delta, p, \epsilon_{\text{opt}})$ and the effective area A_{eff} is taken from the effective area lookup.

The precision with which the properties of the primary γ-ray can be reconstructed with the IACT method is one of the best, especially in comparison to other ground based approaches e.g. Milagro or HAWC). A general description of the H.E.S.S. system can be found in "The Status of the H.E.S.S. project" (Hinton 2004). The stereoscopic hardware trigger is detailed in Funk et al. (2004). The tracking of the telescopes is discussed in Bolz (2004).

2.3.3.1 Convolution Theorem

In the course of this work, the PSF is a fundamental part of the analysis. As can be seen in Chapters 5 and 6, when using a theoretical model for comparative studies, it is important to see the model in "real terms", i.e. the model must be convolved with the H.E.S.S. PSF so a direct comparison can be made between observations and theoretical predictions.

In general, if a system is linear and time-invariant, then the response to a delta function at $t - \tau$ is a shifted version of the response to a delta function at $t = 0$. i.e. $\mathrm{h}(t \,|\, \tau) = h(t - \tau \,|\, 0)$. For time-invariant systems we often write $h(t - \tau)$ in place of $h(t - \tau \,|\, 0)$ and so the output is :

$$g(t) = \int_{-\infty}^{\infty} f(\tau)\, h(t - \tau)\, d\tau \tag{2.9}$$

This is called the convolution of f and h and is denoted by :

$$g = f * h \tag{2.10}$$

and in 2-dimensional image processing terms, this convolution integral may be expressed as :

$$g(x,y) = f(x,y) * h(x,) = \int_{-\infty}^{\infty}\int_{-\infty}^{\infty} f(\tau_\mu,\tau_\nu)\, h(x-\tau_\mu, y-\tau_\nu)\, d\tau_\mu dt_\nu \tag{2.11}$$

In the context of this work, the PSF depends on three components, the zenith angle (θ), the offset (ϕ) and the energy (E) :

$$\int_{\theta_1}^{\theta_2}\int_{\phi_1}^{\phi_2}\int_{\mathrm{E}_1}^{\mathrm{E}_2} d\theta\, d\phi\, d\mathrm{E} \tag{2.12}$$

and this convolution integral for each theoretical model was solved numerically.

2.3.4 Calibration

Calibration is the process of conversion from the raw digital counts in the individual PMTs to light intensity in photoelectrons (p.e.) corrected for non-uniformity. Here, an overview of the main steps are presented. The calibration of the data for the H.E.S.S. experiment is described in further detail by Aharonian et al. (2004a).

During observations, the analogue signal in the PMTs is integrated over a time gate of τ = 16ns and converted into digital ADC (Analogue to Digital Converter) counts – ADC_i in pixel i. The raw data stored by the Data Acquisition system (DAQ) is stored in the form of ADC counts per pixel at a given time. The following steps assure a correct transformation of ADC counts in each pixel into the corrected signal amplitudes A in photoelectrons :

- **Estimation of pedestals :** The pedestal is defined as the mean ADC value ADC_{ped} in the absence of a signal and is produced by a combination of electronic voltage offsets and night-sky background (NSB) light. It is therefore determined by the value of high voltage on the PMTs. The pedestal values are determined during observations, from which the shower images are subtracted. The pedestal value is recalculated on a regular basis, always after a fixed number of events. Dedicated *electronic pedestal* runs are used to obtain the electronic pedestal, which do not contain the NSB. The fluctuations of the ADC values are Gaussian with the width depending mainly on the temperature and the NSB level.

- **Estimation of the conversion factor G_i between the signal and ADC counts :** This factor called the *gain* is defined as :

$$G \equiv \left(\frac{ADC_{counts}}{\#\ \mathrm{p.e.}}\right) \tag{2.13}$$

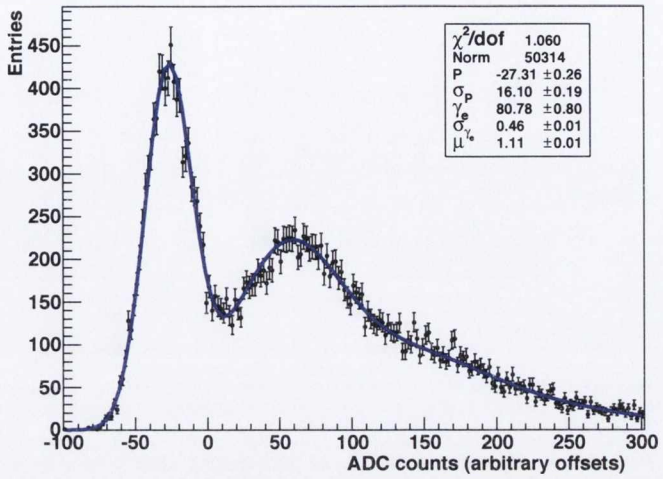

Figure 2.9: *Distribution of the ADC values for a single pixel, illuminated by dim light. Figure taken from Aharonian et al. (2004a)*

It is determined for each pixel i and is measured regularly, approximately every second night of observation. The measurement is performed under a very dim illumination of the cameras, corresponding to ~1 photoelectron per pixel per time window τ. The ADC distribution shows two distinct peaks – one corresponding to the electronic pedestal (with no light in the integration gate) and a second, corresponding to one p.e. hitting the PMT within the integration time. By fitting the second peak, we obtain a value $\mathrm{ADC}_{1\,p.e.}$ (see Figure 2.9). The gain is then determined from the distance of the two peaks measured in digital counts. A third peak might also be recognised, which denoted the case of two p.e.

- **Estimation of the flat-fielding coefficients :** Flat-fielding (FF_i) is an additional procedure that guarantees a homogeneous response of the camera to a homogeneous source of light. The deviations from homogeneity occur due to different photocathode efficiencies and different optical efficiencies of individual pixels. These would otherwise not be corrected by the previous steps.

- **Pointing corrections :** This step corrects deviations from nominal pointing of the telescopes. These are caused by mechanical bending of the masts depending on the observation angle. The procedure comprises of applying a mechanical model, observing stars with known positions and observing the projection of fixed LEDs on the camera plane from the mirror dish.

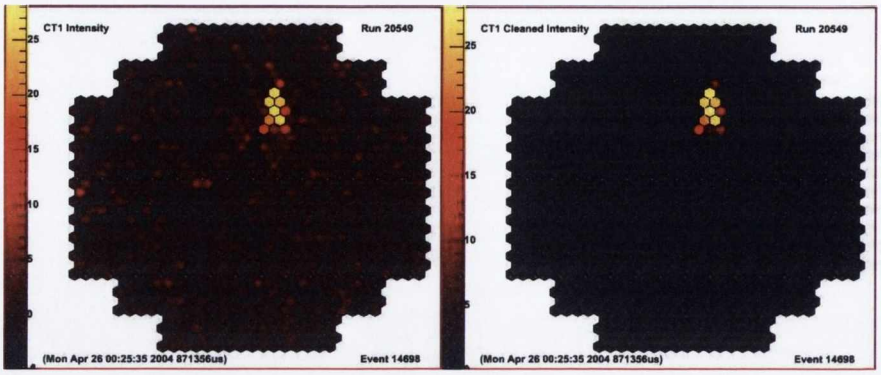

Figure 2.10: *Left: Intensity distribution of a γ-ray candidate event in one camera. The colour denotes the pixel intensity in photoelectrons. Right: Same event after image cleaning using tailcuts of $T_{high} = 10$ and $T_{low} = 5$. Figure taken from Funk (2005).*

Other processes such as the determination of the NSB and the identification of broken pixels, are also part of a standard calibration.

Therefore the signal amplitude in one pixel can be calculated as :

$$A_i = \frac{ADC_i - ADC_{ped,i}}{G_i} FF_i \tag{2.14}$$

where ADC_i is the value measured in one pixel i, $ADC_{ped,i}$ is the pedestal value, FF_i flat-fielding coefficient and G_i gain.

After the calibration, data is stored in the form of signal charge (p.e.) per pixel per event. The data is checked to meet certain data quality criteria and can then be analysed.

2.3.5 Image Cleaning

After calibration of the light intensity distribution in the camera, the image is cleaned of noisy pixels which are likely to have been created by noise in the PMTs or the NSB. The process of image cleaning is typically based on two threshold values : T_{high} (~ 10 p.e.) and T_{low} (~ 5 p.e.). These threshold values correspond to the number of photoelectrons in a given pixel. The image cleaning method categorises each pixel of the image in the following way:

- pixels containing more p.e. than T_{high} with a neighbouring pixel above T_{low} are kept in the image.

- pixels containing more p.e. than T_{low} but less than T_{high}, with a neighbouring pixel above

T_{high} are also kept in the image.

- in addition to the two fixed threshold values, a NSB threshold is used to prevent the inclusion of pixels suffering from bright star light. Only pixels passing the two first cuts have an intensity of more than 3σ of the pedestal RMS are kept.

- all other pixels are discarded and are not considered in the calculation of the Hillas parameters which are described in Section 2.3.9.

Figure 2.10 shows a camera image for a γ-ray candidate before and after image cleaning. The cleaning process leads to a large reduction in the number of pixels present in the image.

2.3.6 Data Quality

Quality checks of data are an important part of the H.E.S.S. experiment. The main purpose of these checks is to identify possible problems during and after observations. As well as trying to reduce systematic effects caused by atmospheric and weather changes, it is a regular check for any problems caused by malfunctioning hardware.

Of course observers want the best quality data possible, so the suppression of systematic errors at this early stage is very important to achieve good quality results later in the analysis. The DAQ at the H.E.S.S. site is largely automated. During the course of each observation, data is monitored directly by a shift crew of two or three people on site in Namibia. The observed qualities are mainly the stability and absolute value of a trigger rate. The trigger rate is very sensitive to changes in the atmosphere and its stability is thus the most important data-quality criterion. As well as this, the observers monitor the weather conditions and any malfunctions in the hardware, which allows one to produce a set of preliminary results.

At the end of each night, online data quality checks are performed in order to identify hardware problems which could be repaired during the following day. Data have to pass a given set of cuts on several hardware-related quantities. Only data passing these cuts are used for the analysis. Images from the data passing the run selection criteria are then calibrated and 'cleaned' to remove noise from the image. As was mentioned in Section 2.3.5, the noise is likely to be caused by photomultiplier noise or the night sky background. The image cleaning is done using a two stage *tail-cut* procedure which requires a pixel to have a signal greater than 5 p.e. and a neighbouring pixel to have a signal greater than 10 p.e.

Once this image cleaning is performed, the width and the length of the elliptical shower image are parametrised using a Hillas type analysis (see Section 2.3.9 for full description).

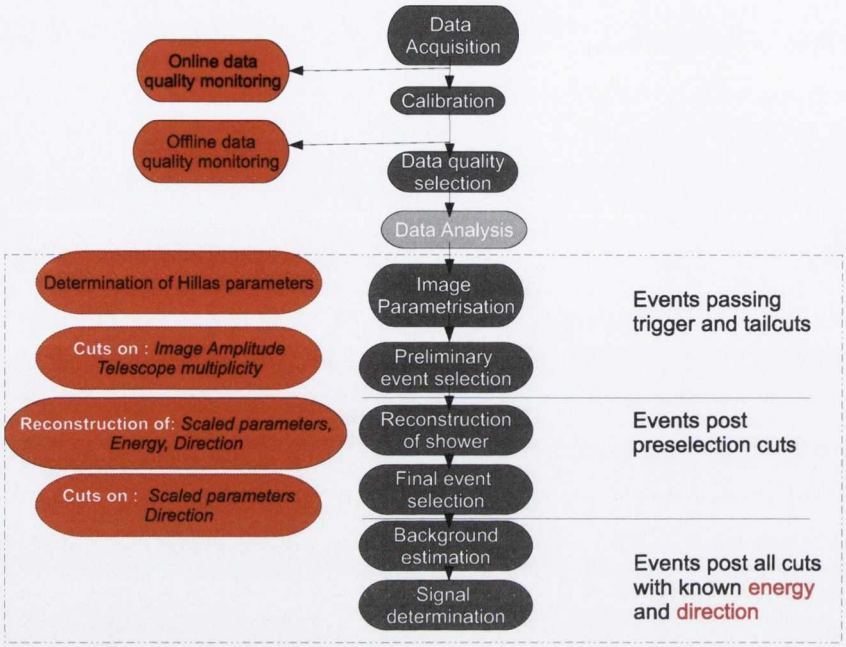

Figure 2.11: *Schematic view of the H.E.S.S. dataflow. The top part depicts the general data flow. The lower inset shows the data flow in the standard analysis chain, described in the text. Figure adapted from Nedbal (2008).*

2.3.6.1 Online Data Quality Monitoring

Each observation run lasts 28 minutes. Once each run is finished, it undergoes a series of online checks. The run is calibrated using an automatic preliminary calibration procedure (described above), using the most recent calibration coefficients. Afterwards, the run is processed using the standard analysis chain and various quality-related quantities are checked in order to identify malfunctions of individual subsystems of the telescope array. All checks are summarised and posted on one of the H.E.S.S. internal web pages, for everyone within the collaboration to access.

After the calibration chain has completed, the data has to pass a set of cuts on several hardware-related quantities. Only data passing these cuts are used for analysis. The data flow of the H.E.S.S. experiment is depicted in Figure 2.11. It can be split into the general flow of the data and the analysis dataflow. The former includes data acquisition, calibration of the data and the quality monitoring after each step, while the latter focuses on γ-ray event reconstruction.

2.3.6.2 Offline Quality Selection

After the data is transferred to Europe from Namibia, it is calibrated using the standard calibration chain described in 2.3.4 and is sorted based on its quality. The difference, as opposed to the on-line calibration is that here, the various calibration coefficients are merged over an entire period to ensure full calibration of all pixels and remove problematic calibration coefficients. The subsequent quality selection is based on a system of cuts on several indicators of malfunctioning hardware or bad atmospheric conditions.

These quality cuts were used in Aharonian et al. (2006d) for analysing the Crab Nebula. The resulting systematic error on the flux was estimated to be $\sim 20\%$.

2.3.7 Event Reconstruction

A discriminating procedure is applied to the camera to select only the pixels that belong to the shower image. The direction of the origin of the shower can be easily reconstructed by simply transforming the two (or more) images of the shower into a common coordinate system. The shower direction is given by the intersection point of the two main axes (more advanced mechanisms are discussed in Hofmann et al. (1999); Hofmann (2000)). Angular resolutions achieved with this method are typically in the order of 0.1° per event.

To conduct stereoscopic observations, a central trigger unit is needed. The central trigger system of the H.E.S.S. telescopes requires a minimum of two telescopes to be triggered by the Cherenkov light from an EAS. The cameras send their triggers to a central trigger unit. The event will only be recorded if two or more telescopes trigger in a certain time interval (Funk et al. 2005). Thanks to this stereoscopic trigger system, the background from single muons can be greatly reduced and it allows for the stereoscopic reconstruction of the particle parameters. For each event that meets the trigger criteria, the current signals from all PMTs of the triggered cameras are read out and stored on mass storage devices. The signal is not usually sampled in time but is integrated over a certain short time period (16ns).

2.3.8 Data Taking

Observations with Cherenkov telescopes are taken on clear, moonless nights, due to the need for darkness to be able to detect the faint flashes of Cherenkov light. Therefore each month, the observation period lasts $\sim$ 24 days, with the length of available observing time peaking on the night of the new moon. Each observation run lasts for 28 minutes approximately, during which time the telescope system tracks a specific astrophysical target or position in the sky. In an ideal scenario, all configuration parameters of the system are kept constant during a run. The

simplest observation strategy consists of ON/OFF observations of the source in question. Runs with the telescopes pointing at the source (ON runs) and runs with the system pointing at on "off region" (OFF runs) are alternately performed. These OFF runs are then used to derive the estimation of the background. The elevation of the telescope system should be the same for the ON and OFF runs, to reduce the influence of systematic errors. In the case of H.E.S.S., which has a large field of view, it is possible to use an observation technique called *wobble*-mode. In this case, the pointing direction of the system is offset from the astronomical object by a small amount (typically between 0.5° and 1°) alternating in different directions in consecutive runs. The background estimation can then be taken from the same data set, i.e. from a position mirrored with respect to the pointing direction of the system. For further details, see Section 2.3.14.

2.3.9 Image Parametrisation

The Hillas Parameters (Hillas 1985) are a set of characteristics which are used as a standard method for parametrisation of the light intensity distribution. After a set of images of an air shower have been recorded, they are processed to measure Hillas parameters based on the second moments of the image. These parameters are then used for event selection and reconstruction (see Figure 2.12).

The image parameters contain key information about the shower. The width and length of the shower image differ depending on the source particle of the shower, therefore allowing gamma/hadron separation. The amount of light collected by the telescopes is related to the energy of the primary particle, allowing us to use the size parameter for energy reconstruction. The incident direction and the shower impact position on the ground can be determined on the basis of these image parameters. A straightforward geometrical reconstruction technique is applicable as soon as more than one image of a shower is available.

The most important parameters for the H.E.S.S. analysis are :

- *Width (W)* – this represents the minor axis of the ellipse. A cut on a width-related parameter can be very efficient in background rejection, as γ-ray induced showers are significantly narrower than hadronic showers.

- *Length (L)* – this is the length of the major axis of the ellipse.

- *Centre of gravity (CoG)* – the centre of gravity of the shower. It is calculated in the

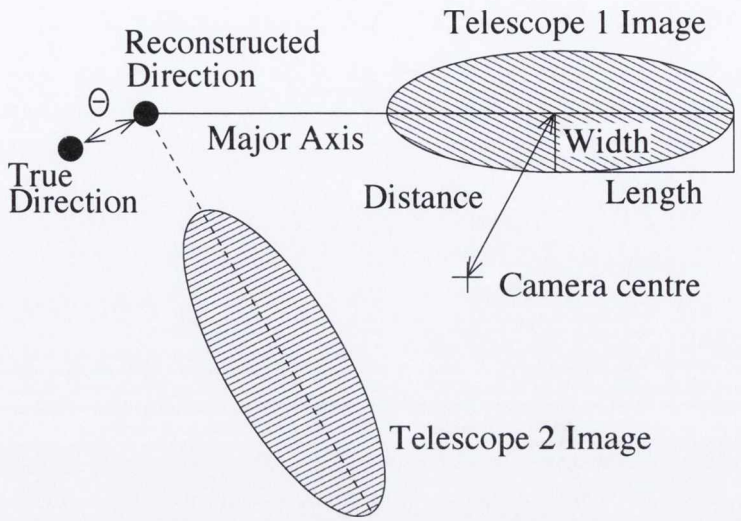

Figure 2.12: *Hillas parametrisation of the γ-ray induced shower images. The distance of the CoG to the camera center, the width and the length of the Hillas ellipses are used in the event selection. The intersection of the major axes in the correct coordinate system determines the origin of the primary particle and the impact position of the shower core on the ground. For simulated showers: the distance between the simulated and the reconstructed shower direction is called θ and determines the angular resolution of the instrument. Image taken from Aharonian et al. (2006d).*

camera coordinates x and y as :

$$x_{cog} = \frac{1}{A}\sum_{i=1}^{N_{pix}} a_i x_i,$$

$$y_{cog} = \frac{1}{A}\sum_{i=1}^{N_{pix}} a_i y_i,$$

where $A = \sum_{i=1}^{Npix} a_i$, a_i is the amplitude of the pixel i and (x_i, y_i) are its coordinates in the camera plane.

- *Displacement (δ)* – the distance between the CoG and the reconstructed direction.

- *Amplitude (A)* – the summed amplitude in all pixels in the cleaned image.

After the parametrisation, the first pre-selection cuts are applied to reject events with less than 2 participating telescopes and with a total image amplitude lower than a specified value (depending on the set of cuts - typically in the range of 40 – 200 p.e.).

2.3.10 Shower Reconstruction

The geometric parameters of the shower image are used to reconstruct the direction of the shower and the *impact parameter* – the distance of the main shower core axis from the telescope. This parameter is very important for reconstructing the shower properties because of its strong influence on all of the image parameters. Along with the image amplitude, it is used to reconstruct the energy and as well as the *scaled shape parameters*.

2.3.10.1 Scaled Shape Parameters

These are entities derived from the width and the length that are later used by event selection cuts. They were introduced in order to allow one to apply one set of cuts under any observation conditions, i.e. the zenith angle θ_Z and the target offset θ_{off}. The width and length of the observed EM shower depend on θ_Z, θ_{off} and on the impact parameter. Thus, for each event, these parameters are scaled by the mean expected value for the given zenith and offset angle (calculated from Monte Carlo simulations). As a result, a *mean reduced scaled width* (**MRSW**) is produced as:

$$MRSW = \frac{1}{N_{tel}} \sum_{i=1}^{N_{tel}} \frac{W_i - \langle W_i(\theta_Z, \theta_{off}, A, IP) \rangle}{\sigma_i(\theta_Z, \theta_{off}, A, IP)}, \tag{2.15}$$

where N_{tel} is the number of participating telescopes in the event, $\langle W_i(\theta_Z, \theta_{off}, A, IP) \rangle$ is the mean width for a given θ_Z, θ_{off}, amplitude A and impact parameter (distance) IP obtained from simulations. σ_i is the appropriate RMS of the parameter distribution. Both of these values are stored in lookup tables, with one 2-dimensional lookup for each combination of (θ_Z, θ_{off}). In the same way, the *mean reduced scaled length* (**MRSL**) is calculated. Note that the mean reduced scaled parameters are constructed in such way that the their value reflects the number of standard deviations, by which it differs from the expectation value for a given set of parameters. This number is averaged over the number of telescopes participating in the event.

2.3.11 Selection Cuts

To achieve a good gamma-hadron separation, a set of cuts have been defined on the geometrical parameters of the event, whose values are summarised in Table 2.3.

In this work, a system of standard cuts on image parameters is used, as described in Aharonian et al. (2006d). Several sets of cuts were produced, each optimised for a different spectral type and γ-ray source strength. When searching for a signal from a candidate target, the set has to be defined a priori in order to avoid unnecessary statistical trial factors. The cuts are optimised for individual source classes by means of maximising the telescope performance $(S/\sqrt{T})$, where S is the significance of a signal. The following sets are used:

Cut	MRSL min	MRSL max	MRSW min	MRSW max	θ^2(deg.) max	Size (p.e.) min	Distance (deg.) max
Standard	-2.0	2.0	-2.0	0.9	0.0125	80	2.0
Hard	-2.0	2.0	-2.0	0.7	0.01	200	2.0
Loose	-2.0	2.0	-2.0	1.2	0.04	40	2.0

Table 2.3: *Cuts on the geometrical reconstructed Hillas parameters.*

- *Standard Cuts :* These cuts are optimised for a source with a flux at the level of ~10 % of the Crab Nebula[2] and with a spectrum similar to the Crab Nebula, i.e. a spectral index of $\Gamma \sim 2.6$.

- *Hard Cuts :* Optimised for a weak source exhibiting ~1 % of the Crab Nebula and with a relatively hard spectrum of $\Gamma \sim 2.0$. Although hard cuts are useful for so-called 'hard sources', they are unfavourable in our analysis due to their stricter cut on image amplitude which leads to an increased energy threshold.

- *Loose Cuts :* Optimised for a strong source with an integral flux comparable to the Crab, but with a steeper spectrum of $\Gamma \sim 3.0$. The steeper spectrum requires a lower energy threshold, which is achieved by lowering the cut on the image amplitude. This set of cuts in the loosest in the sense of rejecting the smallest number of events.

The MRSL and MRSW are a measure of the major and minor axis respectively of the elliptical reconstructed image. The θ^2 cut is a cut on the angular distance between the event reconstructed direction and the true source location. The distance cut refers to the angular distance between the centre of gravity of the reconstructed event and the centre of the field of view.

2.3.12 Energy Reconstruction

In order to estimate the energy E_0 of a primary γ-ray, IACTs use the Earth's atmosphere as a calorimeter. In the simple Heitler model, $E_0 \propto N_{max}$, where N_{max} is the number of particles in the maximum of the electromagnetic shower in the atmosphere. The integrated image amplitude (IA) measured by an IACT therefore depends only on E_0 (to a first order) and on the impact parameter, which is defined as the distance between a telescope and the shower core. The

[2]The integral flux of the Crab Nebula as measured by Aharonian et al. (2006d) is $F_\gamma(> 1TeV) = (2.16 \pm 0.03) \times 10^{-11} cm^{-2} s^{-1}$

dependency on E_0 is linear, to a good approximation. Using this fact, the energy is therefore reconstructed using two-dimensional lookup histograms. For each telescope and selected zenith angles and offsets, a lookup was produced with energy as a function of image amplitude and impact parameter. The energy is interpolated between the closest values of zenith and offset angle.

2.3.12.1 Estimating the error of the energy reconstruction

The energy estimation is tested on simulated Monte Carlo events. For each event of a given simulated energy E_{true}, the energy E_{reco} is constructed using the energy lookups described above.

The energy reconstruction performs well over an energy range of approximately two decades ($\approx 0.3 - 30$ TeV) but it strongly depends on the set of cuts and the zenith angle involved. The regions around the energy threshold E_{th} and at the highest energies are problematic however. All shower images are subjected to fluctuations caused mainly by the changing atmosphere and may lead to an incorrect shower reconstruction. Around E_{th} only events subjected to upward fluctuations of an image amplitude are selected, hence creating a positive bias.

2.3.13 Signal Determination

Once the events are safely reconstructed, in order to estimate an underlying excess due to an astrophysical source, it is crucial to reliably estimate the remaining background of γ-ray like events in the region of interest. The procedure adopted in the present work is described in the next section. The excess is calculated to be:

$$N_\gamma = N_{ON} - \alpha N_{OFF}, \tag{2.16}$$

where N_{ON} is the number of events detected in the ON region, N_{OFF} is the OFF region and the parameter α is the ratio between the exposure in the ON and OFF regions. The exposure in this case is defined as the expected number of γ-ray events during a dead-time corrected observation time T in a region Ω of the field of view :

$$Exp = \int_\Omega dS \int_0^T dt \int_0^\infty dE A_\gamma(r, \phi, E), \tag{2.17}$$

where $A_\gamma(r, \phi, E)$ is the acceptance of the system for a γ-ray like event with a reconstructed energy E at a given position (r, ϕ) of the field of view. The term "γ-ray like event" means any event that passes the event selection cuts and is thus a part of the post-selection background.

The ON region is taken to be a circular region of the same size of the adopted θ^2 cut around

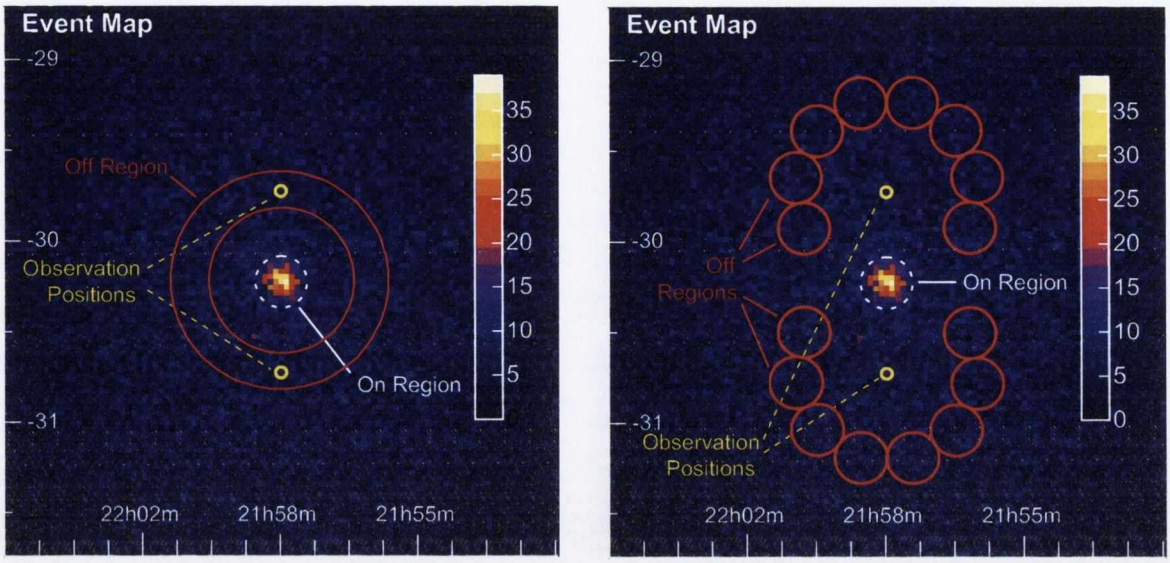

Figure 2.13: *Background estimates - Left: Ring Method, Right: Reflected Region Method. Figure taken from Berge et al. (2007).*

the position of interest. The properties of the OFF region(s) are described in Section 2.3.14, along with the background estimation procedure. The significance of the excess is then calculated using the Li-Ma approach. From Eqn. 17 in Li & Ma (1983) :

$$S = \sqrt{2}\left\{N_{ON}\ln\left[\frac{1+\alpha}{\alpha}\left(\frac{N_{ON}}{N_{ON}+N_{OFF}}\right)\right] + N_{OFF}\ln\left[(1+\alpha)\left(\frac{N_{ON}}{N_{ON}+N_{OFF}}\right)\right]\right\}^{1/2}. \quad (2.18)$$

2.3.14 Background Estimation

Thanks to the large field of view of the H.E.S.S. system, the background rejection technique was an improvement on the classical approach previously used. It is well known that after a thorough cleaning has been performed and a strict cut applied, a fraction of hadron initiated events will remain. Such events constitute the background of γ-ray like events. In the first generation of Cherenkov telescopes, this background was estimated by the so-called ON-OFF procedure. This means that the OFF events were estimated by pointing the telescope in an "empty" part of the sky with similar characteristics (i.e. the same zenith angle and close in time). This was obviously very time consuming and not very efficient.

In the H.E.S.S. field of view, the events in the OFF region can be estimated in the same pointing. This is achieved thanks to "wobble" mode, pioneered by the HEGRA collaboration. This method involves keeping the source inside the field of view, but with a slight offset from

the centre of the field of view. The OFF counts can then be taken from the opposite side of the field of view. The offset is then alternated in declination, so as to smooth the gradients in the field of view.

The main background estimations used by H.E.S.S. are described as follows:

- *Ring Method*: A ring shaped region around the ON region is used to estimate the background, with the configuration shown in Figure 2.13 (left panel). The parameter α corresponds to the ratio of areas of the ON and OFF regions and is typically $\alpha \sim 1/7$. The main advantage of this method is its strength in cancelling linear gradients across the field of view. However, one must be careful to apply a correction for the change in acceptance along the ring.

- *Reflected-Region Method*: In this method, a number N of OFF regions is considered, all of which have the same offset from the centre of the field of view that the ON region has. The configuration is shown in Figure 2.13 (right panel). The OFF regions all have the same size as the ON region, so $\alpha = 1/N$. This ensures that the acceptance is the same in all of the ON and OFF regions, thus making this method well suited for determining the spectrum of a source.

- *Template Method*: This method does not estimate the background from a different portion of the sky, but from a different portion of the parameter space of MRSW. So all the information is extracted from the ON region. As can be seen in Figure 2.14, the distribution of the MRSW of γ-rays and cosmic rays are distinctly different.

In this work, the *ring method* is used for producing skymaps and significance maps (see Chapter 4) and the *reflected-region method* is used to determine the γ-ray signal at a given position and for determining the flux, spectra and the upper limits.

2.3.15 Spectral Analysis and Upper Limits

Once the shape recognition and background subtraction have been completed, the energy determination, which is directly related to the size of the event image in the camera, is performed. In order to determine the spectrum of a source, only events with an energy above a certain threshold are considered. This energy threshold is defined as the peak of the distribution of the γ-rays differential rate. It depends primarily on the configuration cuts used in the analysis and on the zenith angle and degree of offset of the observation. This gives a spectrum of :

$$F(E) = \frac{1}{\mathrm{A_{eff}}} \frac{dN_\gamma}{dEdt}, \tag{2.19}$$

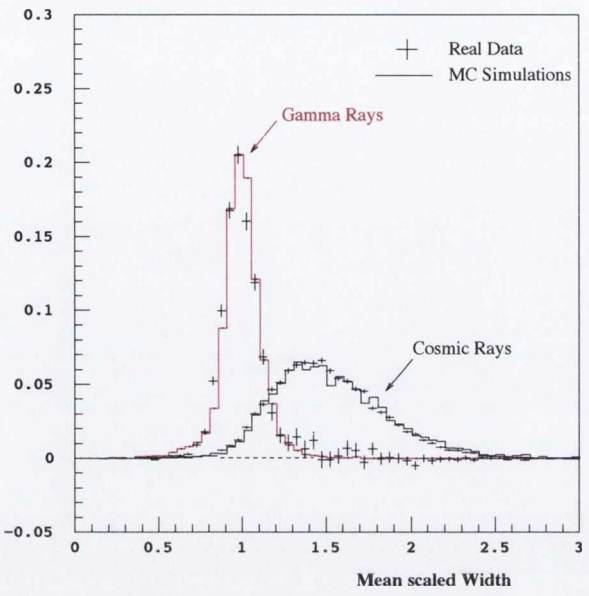

Figure 2.14: *In the Template method, we utilise the fact that the distribution of the MSRW from γ-ray events is distinct from hadronic events. Figure taken from Rowell (2003).*

where N_γ is a γ-ray excess at energy E and A_{eff} is the effective area of the system, which depends on the reconstructed energy of the event (using Monte Carlo simulations). It ranges in value from $\sim 10^3$ m^2 at 100 GeV, to more than 10^5 m^2 at 1 TeV for an observational zenith angle of 20°.

2.3.15.1 Upper Limits

In the case of no excess being detected, an upper limit is calculated. This is done assuming a spectral index Γ for the power-law distribution of the differential spectrum:

$$\left(\frac{dN}{dE}\right) = I_0\left(\frac{E}{1\ \text{TeV}}\right)^{-\Gamma} \tag{2.20}$$

Only events with a reconstructed energy above the energy threshold are considered. Confidence intervals are constructed following the approach by Feldman & Cousins (1998) in order to determine the maximum excess possible for a given N_{ON}, N_{OFF} and α. The confidence interval is therefore [Exc(min), Exc(max)], where Exc(min) = 0.

The maximum excess is then used to calculate the normalisation I_0 = Exc(min) / $A_{eff,tot}$ which will then be substituted into Eqn. 2.20.

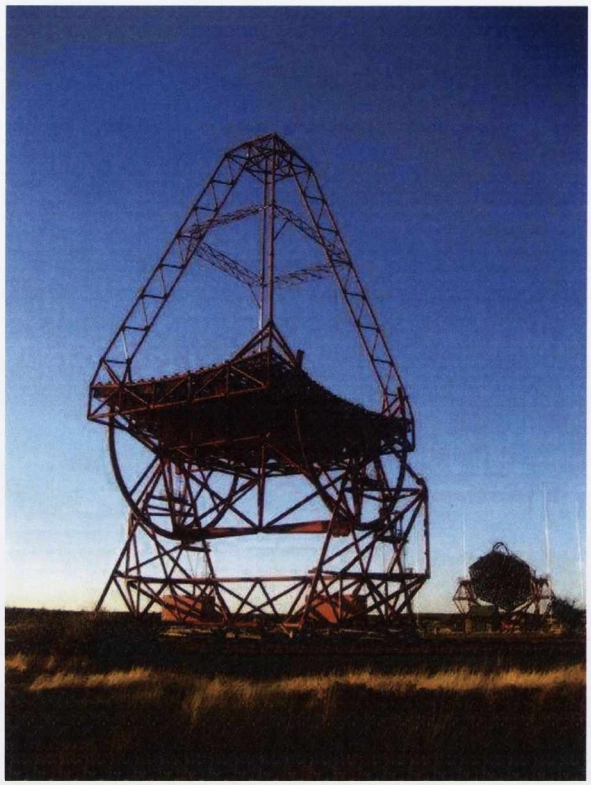

Figure 2.15: *A recent photograph of H.E.S.S. II under construction in Namibia. Note the observer standing at the base to give a sense of scale.*

2.4 H.E.S.S. Phase II

An extension to the H.E.S.S. system consisting of a very large (28 m diameter) telescope is currently under construction at the H.E.S.S. site in Namibia. This Phase-II telescope is aiming for first light in June of this year, with the inauguration ceremony taking place in September.

This new addition to the array will have a parabolic tessellated mirror consisting of over one thousand hexagonal mirrors (90 cm diameter each) to produce a light collecting area of 600 m^2. It contains a very high resolution camera (0.07°) which is positioned at the centre of the present configuration. This upgrade will lower the triggering threshold of the H.E.S.S. array to about 20 GeV, thus broadening the energy window in which γ-rays can be observed.

With its improved angular resolution and lower energy threshold, the new and improved H.E.S.S. system increases our chances of observing pair halo emission in the future.

3

Pair Halos and Beam Broadened Cascades

In this Chapter, details on the formation and the main physical properties of pair halos are presented. A brief description of Monte Carlo simulations performed by Eungwanichayapant & Aharonian (2009) is discussed, as well as the influence of the EBL on pair halo formation.

Following this, the importance of the Intergalactic Magnetic Fields and the phenomenon of so called "Beam Broadened Cascades" are discussed. This is the scenario where an isotropic halo has not formed around the source but the cascade emission continues to propagate along the initial beam direction, broadening the beam width as it does so.

3.1 Physical Processes

The two principal processes which initiate the formation of pair halos around extragalactic objects are photon-photon pair production (PP) and inverse Compton Scattering (IC). Both processes are also important in beam broadened cascade emission and will be described below.

High energy γ-rays have a limited mean free path in the universe. This is due to the fact that these photons will interact with the surrounding soft (low energy) photon radiation, resulting in pair production. When a γ-ray of energy E collides (head on) with a photon of wavelength λ, the pair production threshold is crossed if $\lambda < 2.4$ E (μm / TeV). Depending on the energy of the initial γ-ray, it will pair produce with different background radiations. For example, a

PeV photon can interact with the microwave background light so that its mean free path is very short, ~ galactic distance scales. For lower energy photons, in the TeV range, infrared or optical photons are required to cross the pair production threshold. In this case, the mean free path grows rapidly with decreasing energy, extending to Mpc scales and even further.

When very energetic γ-rays interact with these background photons, their energy is not lost. The two interacting photons convert into an electron-positron pair (e^+e^-). These new pairs will create new γ-rays by inverse Compton scattering on the background field photons. Again, these new γ-rays can pair produce and this process continues, developing an electromagnetic cascade. The cascade ends when the compton-upscattered photons no longer have enough energy to pair-produce on the background photons. Essentially, from your first very high energy γ-ray, through the cascading process, the energy of the initial photon is transformed into many photons of a much lower energy.

3.1.1 $\gamma\gamma$ Pair Production

Pair production is the creation of an elementary particle and its antiparticle, from the interaction of two γ-rays giving the reaction :

$$\gamma + \gamma \longrightarrow e^+ + e^- \tag{3.1}$$

In the relativistic regime, this process is quite similar to inverse Compton scattering, which will be discussed in the next section. Photon-photon pair production has a strict kinematic threshold given by :

$$\varepsilon\omega(1 - cos\theta) \geq 2(m_e c^2)^2 \tag{3.2}$$

where ε and ω are the energies of the two photons, colliding at an angle of θ in the laboratory frame (Aharonian 2004). The threshold condition is derived by assuming that the photons collide head-on and produce an $e^{\pm}$ pair at rest:

$$\varepsilon_{th} = \frac{1}{\omega} \tag{3.3}$$

Photon-photon pair production is one of the most relevant elementary processes in high energy astrophysics, due to its large cross-section. Several approximations for the total cross-section of this process in an isotropic radiation field have been proposed by Gould & Schréder (1967), Aharonian, Atoian, & Nagapetian (1983) and Coppi & Blandford (1990). The cross section is defined as:

$$\sigma_{\gamma\gamma} = \frac{3}{8}\sigma_T f(q) \tag{3.4}$$

where

$$f(q) = q\left[\left(1 + q - \frac{q^2}{2}\right)\ln\frac{1+\sqrt{1-q}}{1-\sqrt{1-q}} - (1+q)\sqrt{1-q}\right] \tag{3.5}$$

and

$$q = \frac{\left(m_e c^2\right)^2}{\varepsilon \cdot \omega}\frac{2}{1-\cos\theta} \tag{3.6}$$

where $\sigma_T = 6.67 \text{ x } 10^{25} \text{ cm}^{-2}$ is the Thomson scattering cross section.

To quantify the opacity (or absorption probability) to high energy photons, the optical depth ($\tau_{\gamma\gamma}$) can be defined. When the VHE photon propagates in an isotropic low-energy photon field, with spectral density $dn(\varepsilon)/d\varepsilon$, $\tau_{\gamma\gamma}$ per unit path length dl has the following form :

$$\frac{d\tau_{\gamma\gamma}}{dl} = \frac{3}{8}\sigma_T \int_{\frac{(m_e c^2)^2}{E}}^{\infty} \frac{dn(\varepsilon)}{d\varepsilon} F\left(\frac{m_e c^2}{\varepsilon \cdot \omega}\right) d\varepsilon \tag{3.7}$$

and

$$F(q) = 2q^2 \int_q^1 f(x)\, x^{-3}\, dx \tag{3.8}$$

For photons above the threshold energy $m_e c^2 = 511$ keV, the optical depth for pair production of a source of size R is given by :

$$\tau_{\gamma\gamma} = n_\gamma \sigma_{\gamma\gamma} R, \tag{3.9}$$

where n_γ is the photon density and $\sigma_{\gamma\gamma}$ is the cross section for pair production, as discussed in Collmar (2001). For detailed equations see Gould & Schréder (1967) or Vassiliev (2000).

The maximum of $F(q)$, which corresponds to a maximum opacity of the isotropic low-energy photon field to VHE photons, happens when $q = 0.28$ (Vassiliev 2000). This results in the following energy and wavelength relation between the two photons :

$$\varepsilon = 0.93\,\text{eV}\,\frac{\text{TeV}}{\text{E}} \tag{3.10}$$

$$\lambda = 1.3\,\mu\text{m}\,\frac{\text{E}}{\text{TeV}} \tag{3.11}$$

which means that the main source of opacity for a 1 TeV photon is the interaction with photons in the near-IR band ($0.7 - 5\,\mu$m). Above 1 TeV, γ-rays are most attenuated by near- and mid-IR ($5 - 35\,\mu$m) photons from the EBL. Between 300 GeV and 1 TeV, γ-rays are sensitive to near-IR and optical light ($0.38 - 0.75\,\mu$m). Below 300 GeV only UV photons ($\lambda < 400$ nm) will have a large enough cross section to attenuate γ-rays. Finally, below 20 GeV, the absorption is almost negligible due to the very low density of EBL photons below 0.2μ (see Figure 3.3).

Generalising Equation 3.7, one obtains the optical depth for a very high energy photon of energy E travelling from a cosmic source at redshift z :

$$\tau_{\gamma\gamma}(\mathrm{E},\mathrm{z}) = \frac{3}{8}\sigma_{\mathrm{T}}\frac{\mathrm{c}}{\mathrm{H}_0}\int_0^{\mathrm{z}} \sqrt{1+z}\,\mathrm{dz} \int_{\frac{(\mathrm{m_e c^2})^2}{\mathrm{E}(1+\mathrm{z})^2}}^{\infty} \frac{\mathrm{dn}(\varepsilon,\mathrm{z})}{\mathrm{d}\varepsilon}\,\mathrm{F}\left(\frac{\mathrm{m_e c^2}}{\varepsilon\cdot\omega(1+\mathrm{z})^2}\right)\mathrm{d}\varepsilon \tag{3.12}$$

where H_0 is the Hubble constant. If a γ-ray source at redshift z is emitting photons with a given intrinsic flux $F_0(E)$, the flux measured by the observer will be distorted by the EBL absorption in the following way :

$$Flux(E) = Flux_0(E)\cdot e^{-\tau_{\gamma\gamma}(E,z)} \tag{3.13}$$

The mean free path length Λ_{PP} of a gamma-ray of energy ε travelling through an isotropically distributed photon gas of differential energy density $n(\omega)$ is :

$$\frac{d\tau_{\gamma\gamma}}{dl}(\varepsilon) = \Lambda_{PP}^{-1}(\varepsilon) = \int_{1/\varepsilon}^{\infty} \bar{\sigma}_{PP}\, n(\omega)\, d\omega \tag{3.14}$$

where $\tau_{\gamma\gamma}$ is optical depth, Λ_{PP} is the PP mean free path length of the hard photon, with an angle-averaged cross section:

$$\bar{\sigma}_{PP} = \frac{1}{2}\int_{-1}^{1-2/s_0} (1-\mu)\,\sigma_{PP}\,d\mu \tag{3.15}$$

Here $\mu = \cos\theta$ and $s_0 = \varepsilon\omega$. The quantity $(1-\mu)/2$ represents the relative velocity of the soft photon along the direction of propagation of the hard photon.

3.1.2 Inverse Compton Scattering

The up-scattering of photons of low energy through collisions with energetic particles is known as the 'Inverse Compton process'. In this process, a γ-ray photon will collide with an electron, transferring some of its energy to the electron. If photons with lower energy collide with energetic electrons, these photons may gain energy in the collisions, thus promoting them in energy, e.g. from X-rays to γ-rays.

Inverse Compton scattering is very important in regions of high photon densities and can be divided into two regimes : the Thomson regime and the Klein-Nishina regime. The only parameter that regulates the transition is the product of the energies of the incident electron E_e and the up-scattered photon E_γ. In the limiting case, in which $E_e E_\gamma \ll (m_e c^2)^2$ (i.e. the Thomson regime), the Compton cross-section can be approximated by the Thomson cross-section and it is independent of the energy of the photon.

In the case in which $E_e E_\gamma \gg (m_e c^2)^2$ (i.e. the Klein-Nishina regime), the cross-section depends inversely on the energy of the photon. It can be shown that (Rybicki & Lightman 1979):

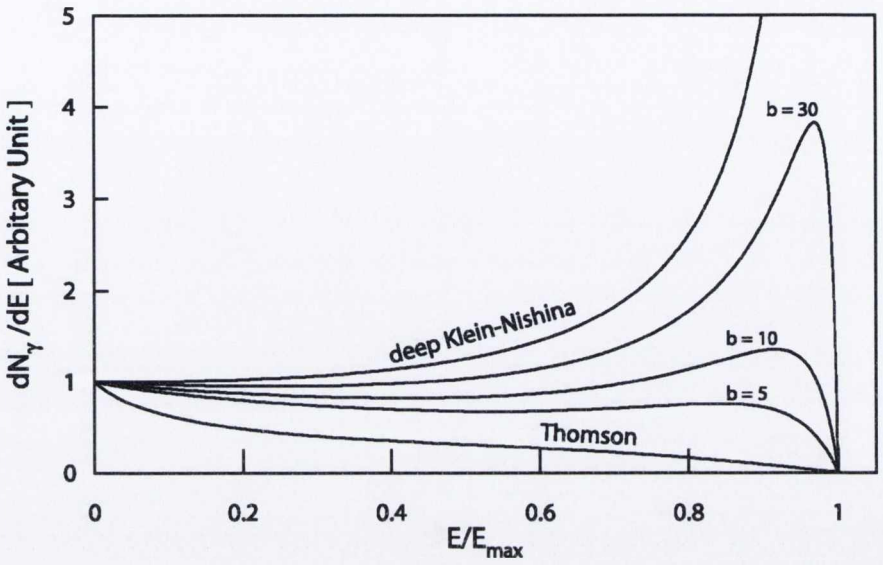

Figure 3.1: *The Spectral Energy Distribution of upscattered photons (in arbitrary units) for different values of the parameter b: $b \to 0$, $b = 5, 10, 30$ and $b \to \infty$. Reproduced from Eungwanichayapant & Aharonian 2009.*

- Thomson regime [$E_e E_\gamma \ll (m_e c^2)^2$]: $E_{\gamma,\mathrm{IC}} \approx \left[\frac{\epsilon}{10^{-2}\mathrm{eV}}\right] \left[\frac{E_e}{10\,\mathrm{TeV}}\right]^2$ TeV
- Klein-Nishina Regime [$E_e E_\gamma \gg (m_e c^2)^2$]: $E_{\gamma,\mathrm{IC}} = E_e$

The cooling time in the Thomson regime is :

$$t_{\mathrm{IC}} = \frac{3}{16\pi c} \frac{(m_e c^2)^3}{q^4} \gamma^{-1} U_{ph}^{-1}, \tag{3.16}$$

where U_{ph} is the energy density of the soft photon field, decreases for increasing energies of the electron. In equation 3.17, q represents the charge of the particle. It should be noted that in the Klein-Nishina regime, the cooling time $t_{\mathrm{IC}} \propto E_e (ln E_e)^{-1}$ increases with the energy of the electron. However, the electron loses a small fraction of its energy in each Compton scattering in the Thomson regime, while it loses a sizable fraction of its energy in the Klein-Nishina regime.

The mean free path of an electron due to the inverse compton scattering, Λ_{IC}, for an electron propagating through the isotropically distributed photon gas density $n(\omega)$ is :

$$\Lambda_{IC}^{-1} = \frac{1}{\beta} \int_0^\infty \bar{\sigma}_{IC}\, n(\omega)\, d(\omega), \tag{3.17}$$

where the cross section averaged over the angular range is :

$$\bar{\sigma}_{IC} = \frac{1}{2}\int_{-1}^{1} (1 - \beta\mu)\, \sigma_{IC}\, d\mu. \tag{3.18}$$

In the Thomson regime, the total cross section is energy independent. In the Klein-Nishina regime however, the $e^{\pm}$ total cross section is a decreasing function of the $e^{\pm}$ energy, i.e. $\propto \chi_0^{-1}$, where $\chi_0 = \frac{E_e}{m_e c^2}\,\omega$.

The spectra of the upscattered photons depend only on the parameter b, where $b \equiv 4\omega\gamma$, as illustrated in Figure 3.1. If the value of b is small, as is the case in the Thomson regime, the upscattered photon population is predominantly in the low energy regime. If the value b is large, corresponding to the Klein-Nishina regime, the population is shifted towards high energies.

TeV electrons cool via inverse compton interactions with background photons. Since this process has no threshold, this occurs with all background photons indescriminately. However, since cosmic microwave background photons are the most numerous, they dominate the cooling. In terms of energetics

$$E_g = \frac{4}{3}\left(\frac{{E_e}^2}{m_e}\right) \cdot E_g^{BG}, \tag{3.19}$$

where E_g^{BG} is the energy of the background photon being scattered.

In the case of E_e = TeV and $E_g^{BG} = E_g^{CMB}$ ($\sim 6 \times 10^{-4}$ eV), we obtain a value of $E_g \approx 3 \times 10^9$ eV. In terms of how frequently these interactions take place, the cross section for the interaction is σ_T (i.e. the Thomson cross-section). So, the interaction time is :

$$t_{IC} = \frac{1}{c \cdot n_{CMB} \cdot \sigma_T}, \tag{3.20}$$

Since $\sigma_T \sim 650$ mb (mb = 10^{-27}cm^2) and $n_{CMB} \sim 400$ cm^{-3}, so $t_{IC} \sim 4000$ yrs. Therefore, each 4000 yrs a TeV electron IC scatters a CMB photon and loses 3×10^9 eV. For it to lose all of its energy (TeV), it must propagate for :

$$t_{IC}^{cool} = \frac{\text{TeV}}{E_g}\, t_{IC} \sim 10^6\, yrs \tag{3.21}$$

3.2 Introduction to Pair Halos

Pair Halos are giant electron-positron structures which are formed due to the development of pair cascades, initiated by interactions of primary multi-TeV photons from high energy extra-galactic sources with the extragalactic background photon fields.

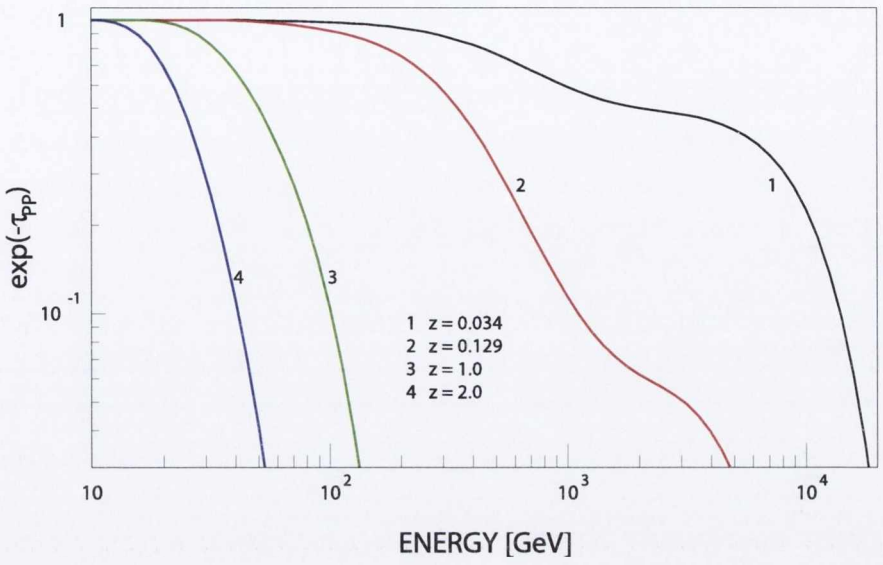

Figure 3.2: *The attenuation factor exp(-τ_{PP}) for γ-rays emitted from sources at different redshift values, as a function of energy for a specific EBL model proposed by Primack et al. (2001). Reproduced from Eungwanichayapant & Aharonian (2009).*

The physical model for pair halos was originally presented by Aharonian, Coppi & Völk in 1994. For distant extragalactic sources which emit γ-rays in the PeV (10^{15} eV) energy range, interactions of the γ-ray photons with the intergalactic diffuse radiation fields will initiate a pair cascade. Depending on the magnetic fields in the vicinity of the source, the cascade can result in an isotropic halo around an initially beamed source.

3.2.1 The Physical Model of Pair Halos

The formation of a pair halo depends on two criteria. First of all, the source must have an extended spectrum up to TeV energies. The initial γ-rays must have a sufficiently high energy to interact with the Extragalactic Background Light. Secondly, there must be a relatively high magnetic field ($B \geq 10^{-11}$G) within ~10 Mpc of the source, to facilitate isotropic emission and create the "halo effect". If these two requirements are met, cascade radiation emitted isotropically from the source should be observable at energies below a few TeV.

The preferred distance for observation of a pair halo with the H.E.S.S. experiment, due to its field of view, is in the range of several mega-parsecs (Mpc) to around 1 giga-parsec (Gpc). This would allow for a reduction in the emission angle and still maintain a high enough flux for detection. If the source is too close, it becomes almost impossible to distinguish between the halo photons and background radiation.

The radiation of a pair halo can be recognised by its distinct variation in intensity with angular distance from the centre. This variation depends weakly on the orientation and beaming/opening angle of a possible emitting jet, but depends more on the total luminosity and duty cycle of the source at energies $\geq$ 10 TeV. Due to the extended emission of pair halos, which can be up to several degrees, this makes it quite a challenge to observe these features with the current ground based Cherenkov telescopes.

The detection of a halo would give us two observables - the angular and spectral distributions of γ-radiation which might make it possible to disentangle the diffuse extragalactic background radiation density (μ_r) and the Hubble constant (H_0). The angular size of a pair halo depends on the density of the background radiation in the vicinity of the source. This means that by observing a pair halo for a source with a given redshift, z_0, i.e. at the epoch z_0, we have an important probe for the cosmological evolution of the associated background radiation.

Although many VHE γ-rays are absorbed by pair production on the intergalactic background radiation fields, much of this emission may not be directly visible. However, the electromagnetic cascades initiated by these absorbed γ-rays may be visible.

3.3 Monte Carlo Simulations of Pair Halo emission

Here the details of the work performed by Eungwanichayapant & Aharonian (2009) are discussed. In Chapter 5, we make comparisons between the observational data and the theoretical predictions based on this model. In Chapter 6, further studies were undertaken to make predictions for pair halo emission for the next generation CTA, as well as re-running this code for new parameters and a more recent EBL model.

The key features of pair halo emission are seen in their spectral energy distributions and their angular distributions. There are three main parameters that can affect the energy and angular distribution of a pair halo :

- $\mathbf{E}_\gamma$: the initial primary VHE gamma photon energy distribution ,

- The background photon field : also known as cosmic background radiation (**CBR**) composed of the cosmic microwave background (CMB) and the cosmic infrared background (CIB),

- z : the distance between the γ-ray source and the observer, indicated by the redshift.

The first two quantities are not easily measured and are especially uncertain.

A major obstacle in the practical realisation of this method is our poor knowledge of the

primary (intrinsic) γ-ray spectrum produced in the source. It is believed that well coordinated observations of γ-ray blazars in different energy bands should allow the identification of the radiation mechanisms, placing strong constraints on the blazar parameter space based on the spectral and temporal properties of these objects.

Nevertheless, these Monte Carlo simulations were conducted to study the dependence of the radiation of pair halos on several key parameters. In particular, the energy spectrum of the primary γ-rays, the influence of the redshift of the source and the importance of the EBL flux.

As discussed in Chapter 5, a differential angular distribution of a pair halo at $z = 0.129$ and $E_\gamma > 100$ GeV, taken from Figure 6 of Eungwanichayapant & Aharonian (2009) was used as our halo profile model for calculating upper limits with *Fermi* and H.E.S.S. observations. This was approximated with a functional form: $dN / d\theta^2 \propto \theta^{-5/3}$.

These calculations were performed for a monoenergetic spectrum of primary γ-rays with E_0 = 100 TeV and an assumed luminosity of $L_0 = 10^{45}$ erg/s. Whenever the energy of the injected photon is large enough to interact with the CMB for a given redshift, the cascade develops in the proximity of the source and quickly converts the injected monoenergetic photon distribution into a power-law distribution with photon index of 1.5. For lower energy injection, the mean free path length for the interaction with the CIB is considerably larger than that for the interaction with the CMB. Here, a widening of the halo with decreasing energy, E_0, is observed.

3.4 Extragalactic Background Light

One of the main motivations for studying distant blazars in the VHE regime is to observe the effects of propagation on their flux. The starlight emitted by galaxies throughout the history of the Universe has accumulated in the infrared (IR) to ultraviolet (UV) wavelengths. It may also have an important contribution from the first stars, which may have formed before galaxy formation began. This radiation is commonly referred to as extragalactic background light. The EBL is the second largest isotropic radiation field, in terms of contained energy, after the 2.7 K cosmic microwave background.

Direct measurements of the EBL are difficult due to strong foregrounds from our solar system and within our galaxy. Therefore, as the measured spectra of distant VHE sources have the imprint of the absorption due to the EBL, the observation of these objects using ground-based Cherenkov telescopes provides constraints on the EBL density (Aharonian 2001). These observations allow the attainment of a better understanding of the origin and properties of the EBL. In recent years, the precision of the EBL constraints set by VHE γ-ray observations of blazars have improved remarkably. In addition, there has been rapid progress in resolving a significant fraction of this background light with deep galaxy counts at IR wavelengths using

satellite detectors such as Spitzer and the Infrared Space Observatory (ISO).

The knowledge of the EBL photon density and its evolution with redshift is important since it carries information about the galaxy and star formation history of the universe. The spectral energy distribution of the EBL can be schematically described as a two-peak distribution (see Figure 3.3). The first component, the optical background, has a peak around 1 μm and is believed to have originated directly from the redshifted radiation from stars. The second component, the infrared background, peaks at $\sim$ 100 μm and results from starlight which has been absorbed by dust inside galaxies and reemitted at longer wavelengths.

It is also important to note that the evolution of the EBL density with time (i.e. in redshift) is critical to test star formation and galaxy evolution models.

3.4.1 Absorption of VHE photons by the EBL

The flux of VHE γ-rays from distant sources is attenuated because γ-rays interact with optical and IR photons from the EBL producing electron-positron pairs. The pair production process between a very high energy photon and an EBL photon happens only when the energy of both photons is enough to produce an $e^{\pm}$ pair is discussed in detail in Section 3.1.

The effective energy-dependence of the interaction (via electron-positron pair production) of primary γ-rays with EBL photons provides an unique tool for probing the EBL. The observed and intrinsic energy spectra of γ-rays are related as $J_{\rm obs}(E) = J_0(E)\exp[-\tau(E,z)]$, where $\tau(E,z)$ is the pair production optical depth (as described previously). This relationship depends on the redshift of the source z and the z-dependent flux of the EBL, $F(\lambda,z)$. For sources located at non-cosmological distances ($z \ll 1$), $d \approx cz/H_0$, with the optical depth for a given distance to the source depending only on the EBL flux at the present epoch, $F_0(\lambda) = F(\lambda,0)$. Thus the observed VHE γ-ray fluxes detected from relatively nearby AGN contain information about the local level of the EBL.

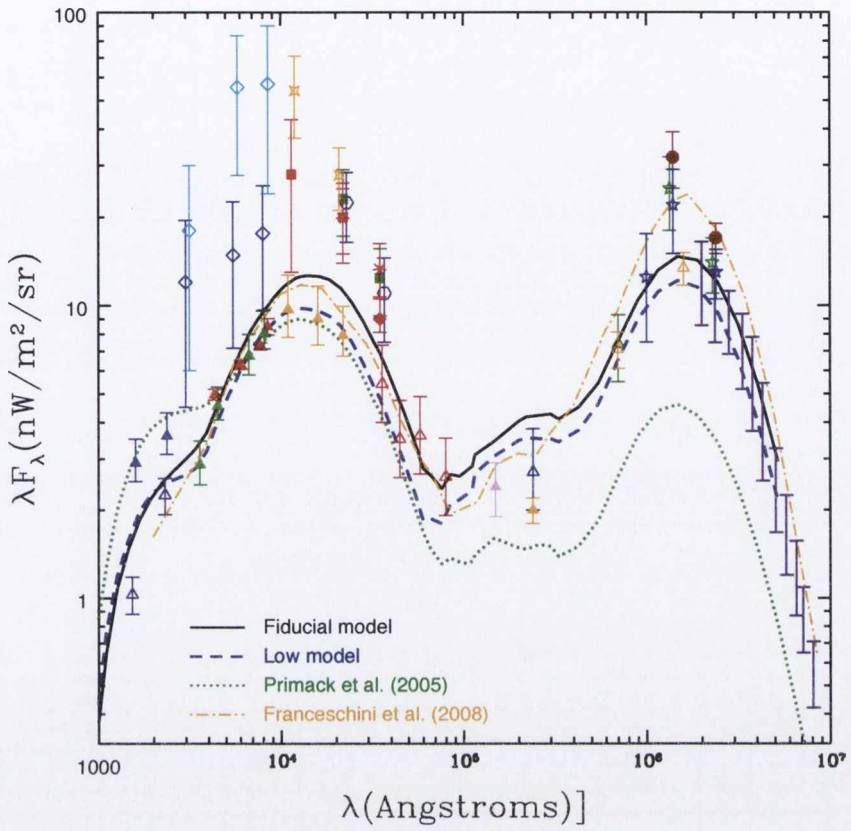

Figure 3.3: *Measurements and model predictions of the spectral SED of the EBL at $z = 0$. Lower limits: The open blue-violet triangles are results from Hubble and STIS (Gardner et al. 2000), while the magenta triangles are from GALEX (Xu et al. 2005). The green and red triangles from Hubble Deep Field (Madau & Pozzetti 2000) and Ultra Deep Field, combined with ground based-data. Gold triangles are also from Madau & Pozzetti (2000). Open red triangles are from IRAC on Spitzer (Fazio et al. 2004), and the pink point at 15 μm is ISOCAM (Elbaz et al. 2002) on ISO. The remaining lower limits are from MIPS at 24, 70, and 160 μm on Spitzer (Papovich et al. 2004; Chary et al. 2004; Frayer et al. 2006; Dole et al. 2006). Direct measurements: The higher open blue triangles are from Bernstein (2007), while the lower points are the original determinations from Bernstein et al. (2002). The high-reaching cyan points in the near-IR are from Matsumoto et al. (2005). The rest of the points in this region are based upon DIRBE data with foreground subtraction, namely Wright (2001) (dark red squares), Cambrésy et al. (2001) (orange crosses), Levenson & Wright (2008) (red diamond), Gorjian et al. (2000) (purple open hexes), (Wright & Reese 2000) (green square) and Levenson & Wright (2008) (red asterisks). In the far-IR, direct detection data is shown from DIRBE: Wright (2004) (blue stars) and Hauser et al. (1998)(green stars), and also purple bars showing the detection of FIRAS Fixsen et al. (1998). Models: Black and dashed blue lines stand respectively for the fiducial and low models from Primack et al. (2008). A previous model Primack et al. (2005) is also shown for comparison (dotted curve). The recent model of Franceschini et al. (2008) is also shown (dash-dotted orange line). Figure taken from Primack et al. (2008).*

3.4.2 EBL models and Direct Measurements of the EBL

The detection of very high energy γ-rays from more than 40 AGN[1], with redshifts ranging from 0.03 to 0.5 provides a unique tool for the exploration of both the Extragalactic Background Light and Extra-galactic Magnetic Fields (EGMF).

As was noted in Vovk et al. (2012a), the limit on the EBL depends on the strength of the EGMF and vice versa. Constraints on the intrinsic slope of the energy spectra of blazars can be obtained from the observations by the *Fermi* Large Area Telescope (LAT) (Atwood et al. 2009) in the energy band below $\sim$ 100 GeV. However, the blazars used for the derivation of constraints on the EBL are characterised by hard spectra, which makes it very difficult to observe their flux below 100 GeV.

Various different methods have been used to calculate the EBL density and its redshift evolution. A forward evolution approach relies on a parametrisation of the evolving stellar populations and calculates the emission spectra of galaxies as a function of time, starting at the beginning of star formation. This semi-analytic model of galaxy formation yields luminosity functions for different galaxy types that are in reasonable agreement with the observations. This is the approach followed by Primack et al. (2005), (updated to Primack et al. (2008)) to avoid under-predicting the EBL level in the far infrared band. On the other hand, backward evolution models start with the existing galaxy population and evolve it backward in time to obtain the EBL level and spectrum (e.g. Stecker et al. 2006). Finally, models like the ones proposed in Kneiske et al. (2002) and Franceschini et al. (2008) exploit relevant cosmological survey data – including number counts, redshift distributions, luminosity functions – fitting and interpolating it with a multiwavelength backward evolutionary model, allowing an estimate of the background photon density and its redshift evolution.

More recently, Meyer et al. (2012), provided new limits on the EBL based on *Fermi* observations. The EBL density was constrained at $z = 0$ over a broad wavelength range, between 0.4 and 100 μm. At optical wavelengths, the EBL density is constrained below 24 nWm^{-2}sr^{-1} and below 5 nWm^{-2}sr^{-1} between 8 μm and 31 μm.

3.5 Intergalactic Magnetic Fields and Beam Broadened Cascade (BBC) Emission

Following pair production in the extragalactic environment, the development of the subsequent cascade is dictated by the strength of the extragalactic magnetic field present.

For strong magnetic fields ($> 10^{-12}$ G), the pairs are quickly isotropised and their energy

[1] See http://tevcat.uchicago.edu for an up-to-date list.

flux accumulates as electron energy density within a volume surrounding the source. Within a B-field range of $\sim 10^{-7}$ and 10^{-12} G, isotropisation will occur and the CMB dominates electron cooling, leaving the angular size of the pair halo to depend mainly upon the pair production length of the γ-rays and the distance to the blazar. Thus, within the above mentioned B-field range the angular size of the pair halo does not change dramatically. To an observer at a given distance outside such a volume, the inverse Compton TeV γ-rays emitted from this accumulated multi-TeV electron population has an angular size approximately independent of the actual EGMF.

The total flux from such a halo thus contains useful information about the total content of multi-TeV electrons accumulated in the vicinity of the source over the period,

$$t_{\rm cool} \sim 10^6 \ (1 \ {\rm TeV}/E_{\rm e}) \ {\rm yr}.$$

This allows an estimate of the time-averaged TeV γ-ray luminosity of the AGN over this time period. Since the production of secondary γ-rays proceeds in the "saturation regime", the halo emission flux at an energy E, provides information about the average luminosity of primary γ-rays at higher energies, namely $E_0 \sim 10(E/1{\rm TeV})^{1/2}$ TeV. For example, with the sensitivity of a γ-ray detector at 1 TeV of about 10^{-12} erg/cm^2/s, one can expect the detection of a pair halo around a source at a distance 300 Mpc, if the average luminosity of the primary radiation above $E \geq 10$ TeV exceeds 10^{43} erg/s. This is quite important information, especially given the highly variable γ-ray emission of AGN which does not tell us about the VHE power of the source on timescales larger than years.

For sufficiently strong magnetic field values (i.e B $> 10^{-12}$ G), there is little doubt that all VHE γ-ray blazars should be surrounded by pair halos. Unfortunately however, the detectability of these halos in VHE γ-rays cannot be guaranteed. This is due to the limited power of the source in γ-rays, and/or a possible cutoff in the γ-ray spectra below 10 TeV, combined with the sensitivity of current generation γ-ray telescopes. This could be the case for many blazars. Due to strong Doppler boosting, the apparent γ-ray luminosities of these objects can significantly exceed the intrinsic (source) luminosity. Furthermore, leptonic models for many of the currently observed blazars do not require many γ-rays beyond 10 TeV.

For weaker magnetic field values ($< 10^{-12}$ G), the cascade energy flux continues to propagate along the initial beam direction, broadening the beam width as it does so. With the angular size of this beam broadened cascade dictated by the EGMF strength, a measurement of the beam width can provide a strong constraint on the EGMF value. Complimentary to this probe, as was demonstrated in Taylor et al. (2011), the combined TeV and GeV emission observed from a blazar can also be used as a probe to the intervening EGMF.

Ultimately for these cascades, the energy of primary γ-rays is released into the intergalactic

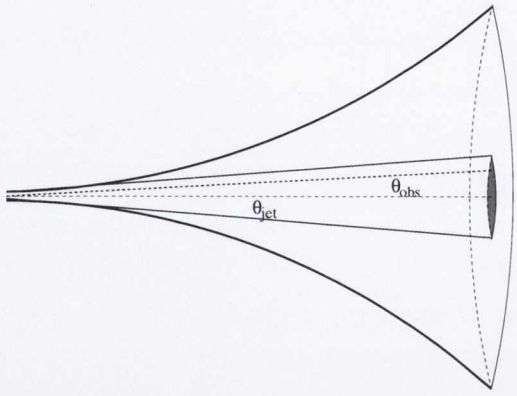

Figure 3.4: *A diagram depicting the flaring of the electromagnetic cascade development in the presence of extragalactic magnetic fields. The initial (conical) jet emission whose power feeds the electromagnetic cascade is shown, with the inner shaded region on the right representing the region filled by the intrinsic cone emission. Reproduced from Taylor et al. (2011).*

medium, contributing to the diffuse extragalactic γ-ray background (Coppi & Aharonian 1997; Huan et al. 2011; Wang et al. 2011). This diluted emission is difficult to detect from individual sources, unless the intergalactic magnetic field is extremely small. Although generally the intergalactic magnetic field in the interstellar medium is expected to have a much higher value, the current observations and cosmological concepts cannot exclude that in some regions, in particular the so-called "voids" with linear sizes as large as 100 Mpc, the magnetic field can be arbitrarily small. In the case of the location of an AGN in such a "void", instead of persistent isotropic pair halo emission, the observer would see direct cascade emission almost rectilinearly penetrating cosmological distances. For such small EGMFs, the propagation of high energy γ-rays cannot be reduced to the simple effect of absorption described by the optical depth (Aharonian et al. 2002; Essey et al. 2011; Taylor et al. 2011). In this case, we deal with a mixture of primary and secondary γ-rays. If the spectrum of γ-rays is hard and extends up to energies beyond 10 TeV, then at lower energies the secondary radiation can dominate over the primary γ-rays. Thus, one cannot apply the standard approach of calculating the deformation of the γ-ray spectrum due to absorption. In a very small magnetic field, the cascade effectively transfers energy towards the cascade propagation, and thus "moves" the source closer to the observer (Aharonian et al. 2002; Essey et al. 2011). As a result the observer can see γ-rays at energies for which $\tau_{\gamma\gamma} \gg 1$.

On the other hand, due to deflections in the EGMF, the original γ-ray beam is broadened, and even extremely small EGMF values are expected to produce detectable extended γ-ray emission[2]. Over cosmological distances, these tiny deflections of electrons can lead to signif-

[2]This radiation should be clearly distinguished from that of pair halos. The origin of the extended emission

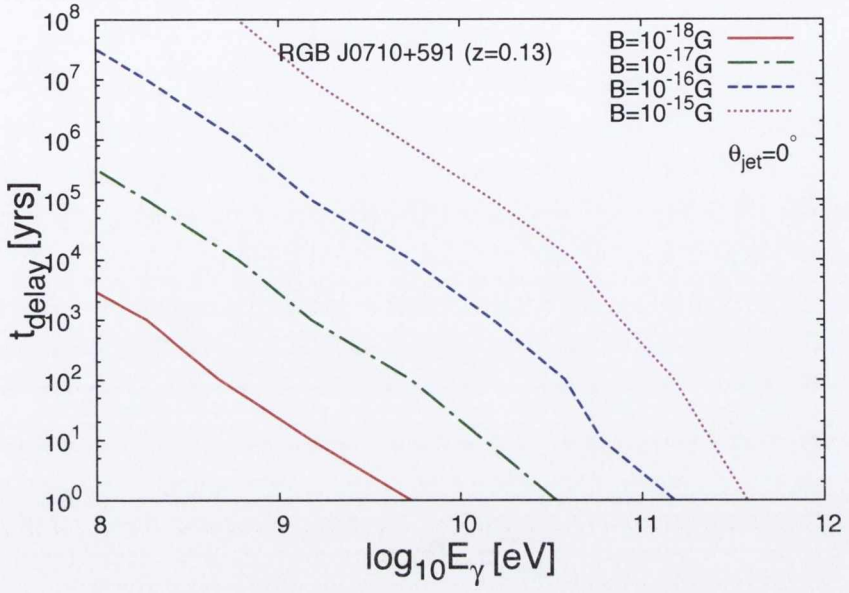

Figure 3.5: *The mean time delay incurred by a photon energy flux following its injection at 10^{14} eV from a sample source, RGB J0710+591, with a redshift z=0.13. The results for different EGMF values are shown, in the range 10^{-18} – 10^{-15} G. Reproduced from Taylor et al. (2011).*

icant delays of radiation (e.g. Plaga 1995). For a certain range of EGMF (depending on the distance to the source), this should allow effective separation of the primary and cascade components based on the studies of angular and temporal features of the detected γ-ray emission. Even from upper limits on the secondary flux emission, one can derive meaningful constraints on the intergalactic magnetic field (see e.g. Taylor et al (2011) and references therein). As can be seen in Chapter 5, a search for extended γ-ray emission in the form of both giant pair halos and broadened γ-ray cascade emission from a few distinct AGN detected by the H.E.S.S. telescope array is conducted.

The preferred distance for the observation of both pair halos and beam broadened cascades with the H.E.S.S. experiment, due to its field of view, is in the range of several hundred mega-parsecs (Mpc) to around 1 giga-parsec (Gpc), i.e. in the range of ~ 0.1 to ~ 0.24 in redshift. The far limit is set by the reduction in flux with distance down to that only just sufficient for detection. On the other hand, the near limit for pair halos results from the fact that for sources too close, it becomes impossible to distinguish between their halo photons and background radiation, as the halo would take up the entire field of view, which for H.E.S.S. is 5°. For beam

in these two cases is quite different, with pair halos producing extended emission isotropically whereas beam broadened cascades producing extended emission only in the jet direction.

broadened cascades, which develop in weaker EGMF, similar near and far limits are also found. In this case, however, the near limit originates purely from a lack of cascade luminosity, which becomes significant only for distances beyond the pair production length, which for multi-TeV γ-rays from the sources we consider, has a typical value of ~ 10 Mpc.

The radiation from both pair halos and beam broadened cascades can be recognised by a distinct variation in intensity with angular distance from the centre of the blazar. This variation is expected to depend weakly on the orientation and beaming/opening angle of the emitting jet, depending more on the total luminosity and duty cycle of the source at energies ≥ 10 TeV (Aharonian et al. 1994). For the beam broadened case, to a 1st order approximation, the radiation deflection angles remain small in comparison to the angular size of the jet. Since we ensure the observer remains "within the jet", the angles (relative to the blazar direction) from which the observer can receive the beam broadened emission remain roughly independent of the observers exact position within the jet cone. This result however, only holds true if the observer isn't too close to the edge of the jet (Figure 3.4).

Since this extended emission can be up to several degrees, it becomes quite a challenge to observe these features with the current ground based Cherenkov telescopes. Much of the flux emitted directly from the source may not be visible, as many VHE γ-rays are absorbed by pair production on the intergalactic background radiation fields. However, the electromagnetic cascades initiated by these absorbed γ-rays may be visible.

4

H.E.S.S. Observations and Data Analysis

During its years of operation, more than 70 γ-ray sources, 30 of which are extra-galactic have been discovered by the H.E.S.S. Cherenkov telescope array. This chapter is devoted to the three AGN chosen for this study, justifying our reasons for their selection. Although the results presented here have not been published, they are in strong agreement with previously published H.E.S.S. data. A detailed analysis of these three objects, PKS 2155-304, 1ES 1101-232 and 1ES 0229+200 is presented in this chapter. Detailed morphological and spectral analyses are performed for all three AGN, as well as coalescing information on these sources to give a complete picture of their characteristics and to demonstrate their suitability for this study.

4.1 PKS 2155-304

The active galactic nucleus PKS 2155-304 located at a redshift of $z = 0.117$, has been detected by the H.E.S.S. array with high significance ($> 100\sigma$) at energies greater than 160 GeV (Aharonian et al. 2005b). PKS 2155-304 is now known to be one of the brightest extragalactic X-ray sources in the southern sky and has been detected on a regular basis over many years in γ-rays. The observed flux of VHE γ-rays shows variability on time scales of months, days, hours and even minute timescales (Aharonian et al. 2007b). It is associated with a compact, flat-spectrum radio source and exhibits an essentially featureless continuum from radio to X-ray frequencies.

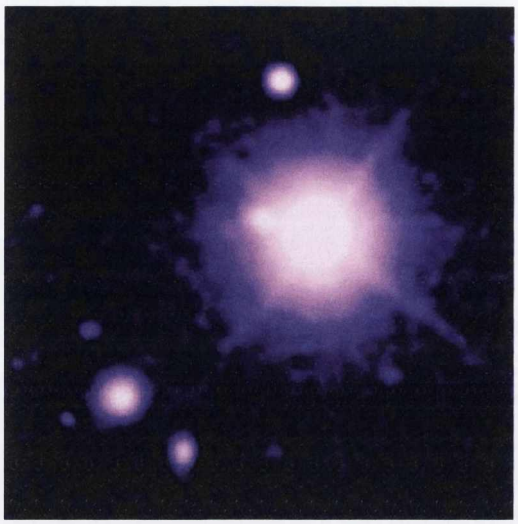

Figure 4.1: *Optical image of the BL Lac object PKS 2155-304 (brightest object) obtained in an R-filter observation with ESO-NTT (European Southern Observatory New Technology Telescope).*

γ-ray emission in the energy range 30 MeV to 10 GeV was detected from PKS 2155-304 by the *EGRET* detector aboard *Compton Gamma Ray Observatory* satellite (Vestrand et al. 1995). The *EGRET* observations indicated a hard energy spectrum with an integral power-law photon index of 1.71 ± 0.24. At TeV energies, PKS 2155-304 was first detected by the Durham telescopes in 1999, with a statistical significance of 6.8 standard deviations (Chadwick et al. 1999).

PKS 2155-304 was among the first targets of observation with the H.E.S.S. system and after the first months of operation, revealed a clear TeV signal. At the moment, there are more than 250 hours of data collected by the H.E.S.S. experiment for this source and it is regularly on the observation schedule with more time dedicated to it. PKS 2155-304 has a level of minimal activity which seems to be steady on a several-year time scale. Hence, this state will be referred to as the "quiescent state" of the source.

PKS 2155-304 is one of the few blazars which can be detected by H.E.S.S. during its quiescence state in short (hour-scale) exposures. The other TeV detected blazars are typically much dimmer at VHE γ-rays energies and therefore can only be observed with H.E.S.S. during their flaring states. In the high energy range (MeV to GeV) the situation is similar. Only a few TeV BL Lacs are bright enough at GeV photon energies for *Fermi*-LAT to detect them at high significance on daily timescales. PKS 2155-304 is quite exceptional in this regard.

The fact that PKS 2155-304 is located at the relatively large distance of $z = 0.117$, the TeV radiation is significantly attenuated due to interactions of TeV γ-rays with the extragalactic background light, resulting in electron-positron pair creation. Depending on the assumption

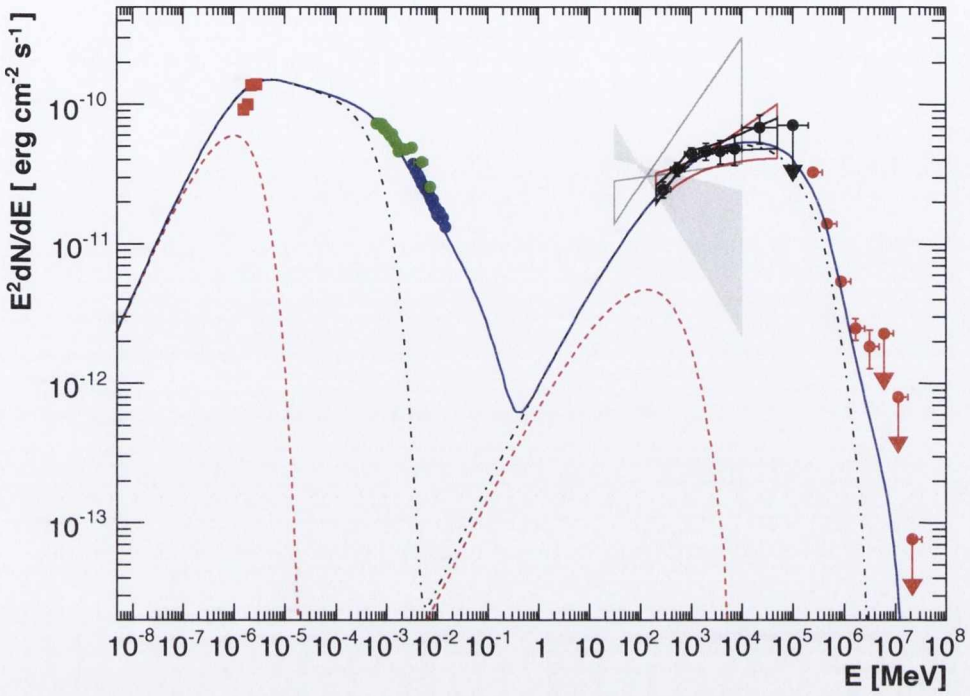

Figure 4.2: *Multiwavelength spectral energy distribution for PKS 2155-304. Simultaneous observations were made with H.E.S.S. (red circles), Fermi (red butterfly), and EGRET (grey butterflies). Reproduced from Aharonian et al. (2009a)).*

of the EBL intensities (our knowledge of the EBL at various wavelengths is still very poor), attenuation at TeV energies ranges from a factor of 10 to 100. The relatively steep TeV γ-ray energy spectrum measured by H.E.S.S., with a spectral index of 3.3 ± 0.1, we assume, partially reflects the attenuation with increases in energy. This well measured spectrum will help to constrain EBL models. Until now, the only objects which have been studied with comparable precision are the AGN Markarian 501 and 421, which are much closer, located at a redshift of ~ 0.03.

4.1.1 An exceptional flare from PKS 2155-304

The physical processes in the central engines of AGN and their jets are usually considered the main candidates for the origin of their observed variability. On July 28th 2006 (MJD 53944), an extreme flare from this source was observed by H.E.S.S. Causality requires that PKS 2155-304 is a point-like source for H.E.S.S. during the flare state. This powerful flare emission is very compact and therefore cannot be associated with the halo emission. This exceptional flare

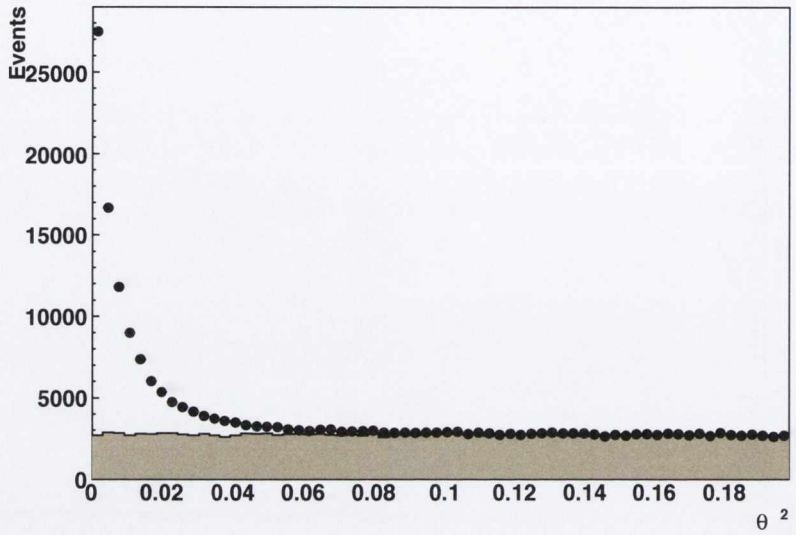

Figure 4.3: *The θ^2 distribution of on-source events (points) and normalised background events (shaded) for PKS 2155-304.*

(Aharonian et al. 2009a), which was looked at separately from the rest of the data for this study, creates two data sets for PKS 2155-304 : high state and low state.

The fact that the PSF is comparable to the halo size, the halo can be concealed by flare events, so it is best to exclude the flare from the pair halo analysis. Considering that the time of the flare, $t_{flare} << t_{total}$, the total time spent observing this source, it is not problematic to exclude this part of the data set. The flare data set proves to be very useful for probing the PSF, which will be discussed in Section 4.4.

PKS 2155-304 has been studied in detail, especially the flare, for many different purposes. One such study involved searching for constraining limits on an energy dependence of the speed of light from a flare from this source (Aharonian et al. 2008a). Since no significant time lag was found, lower limits on the energy scale of the speed of light modifications were derived. Studies of spectral and temporal variability have also been performed (HESS Collaboration et al. 2010), derived on time scales ranging from 3 years down to 4 minutes, with very interesting results. Variability studies using detailed light curves obtained from PKS 2155-304 have placed strong constraints on blazar parameter space. VHE γ-ray emission is usually thought to originate from a relativistic jet, emanating from the vicinity of the super-massive black hole (SMBH). The physical processes in play are still poorly understood, but continued studies of the γ-ray flux spectral and temporal characteristics will help to provide deeper insight.

4.1.2 H.E.S.S. Data Set and Data Reduction

PKS 2155-304 was first observed by H.E.S.S. in July 2004,with the most recent observations used for this study taken in July 2009. This data set comprises of 451 runs in total, amounting to ~ 210 hours of good quality data, for 4 telescopes. These observations were performed at zenith angles ranging from 18° to 24°, with a mean angle of ~ 21°. The analysis energy threshold for these observations was ~ 200 GeV. The data was taken in *wobble mode* with a pointing offset of ± 0.5° in declination relative to the centre of the field of view of the camera during the observations. The data has been analysed based on the so-called standard Hillas parameters as described in Aharonian et al. (2006d).

Taking the whole data set, an immense excess of 54,736 γ-ray candidates were found corresponding to a statistical significance of 320 σ (Figures 4.4 and 4.3).

The differential energy spectrum of the source is shown in Figure 4.5. It is fitted by a power law $dN/dE = \Phi_0(E/1\text{TeV})^{-\Gamma}$ with a normalisation $\Phi_0 = (8.02 \pm 0.68_{stat} \pm 1.0_{sys}) \times 10^{-14}$ $\text{cm}^{-2}\text{s}^{-1}\text{TeV}^{-1}$ and a photon index $\Gamma = 3.3 \pm 0.1_{stat} \pm 0.1_{sys}$. It should be noted that in Figure 4.5 the entire data set for PKS 2155-304 has been used. For this reason, a simple power law is not an ideal fit, but has been used here for demonstrative purposes only. The spectral energy distrubutions shown in Chapter 5 are more representative of the varying states of this source.

The integral flux above 200 GeV taken from the spectral fit is $\Phi(E > 200\text{ GeV}) = (1.4 \pm 1.9) \times 10^{-12}\text{cm}^{-2}\text{s}^{-1}$. A sharp peak in variability was detected ~ MJD 53926 (Figure 4.6), which corresponds to the exceptional VHE γ-ray flare observed in July 2006 which was described previously.

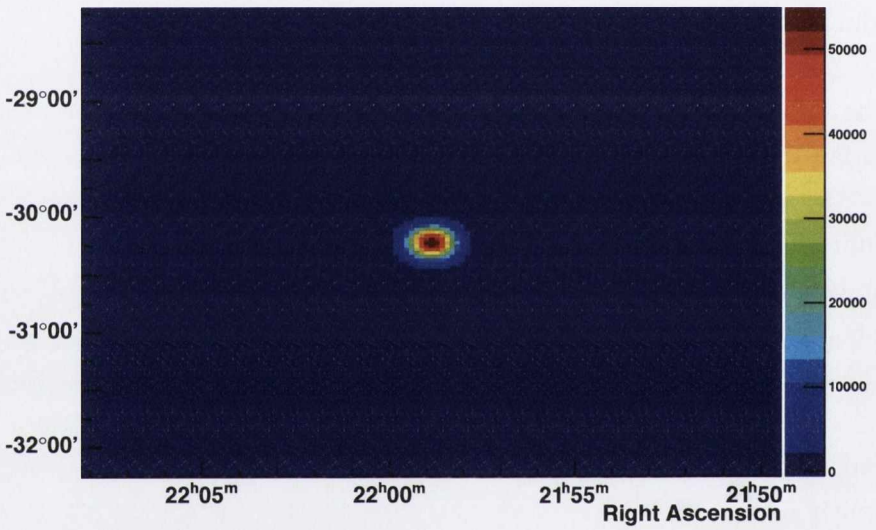

Figure 4.4: *The two-dimensional distribution of the excess events in the direction of PKS 2155-304. A very strong, clear excess is visible at the centre of the map, which has co-ordinates of Right Ascension and Declination. The right-hand scale is the number of excess events.*

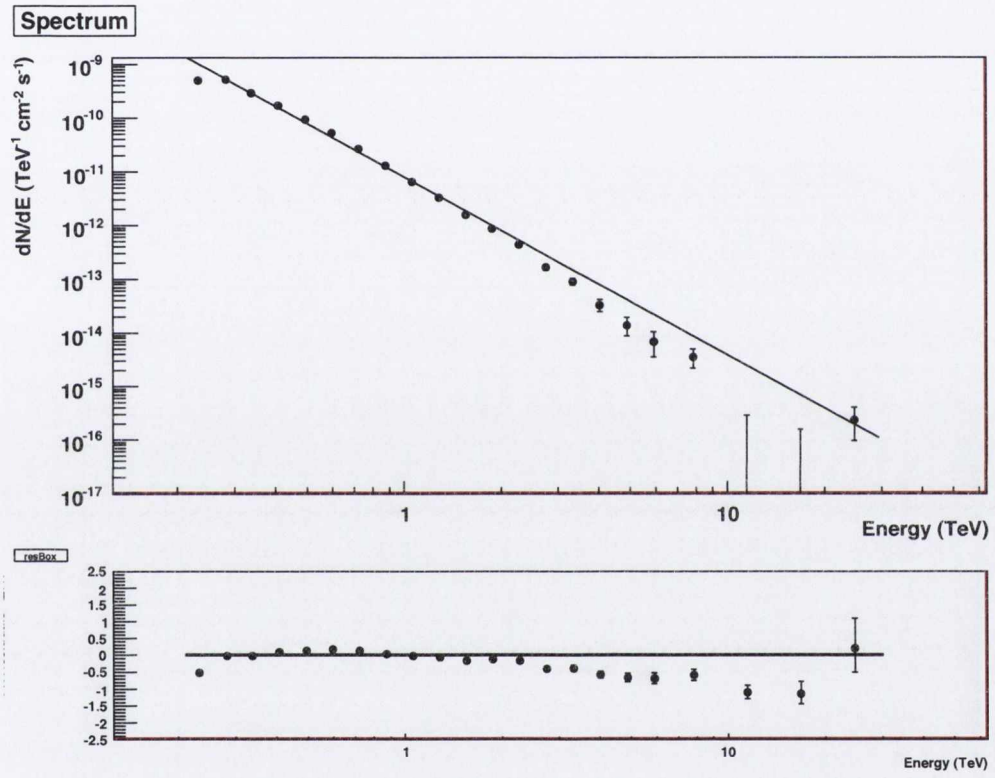

Figure 4.5: *Top panel: Differential energy spectrum of PKS 2155-304 for the complete data set. The spectrum is fitted with a power law of photon index* $\Gamma = 3.3 \pm 0.1_{stat} \pm 0.1_{sys}$ *(black line). Bottom panel: The residuals to the power law fit.*

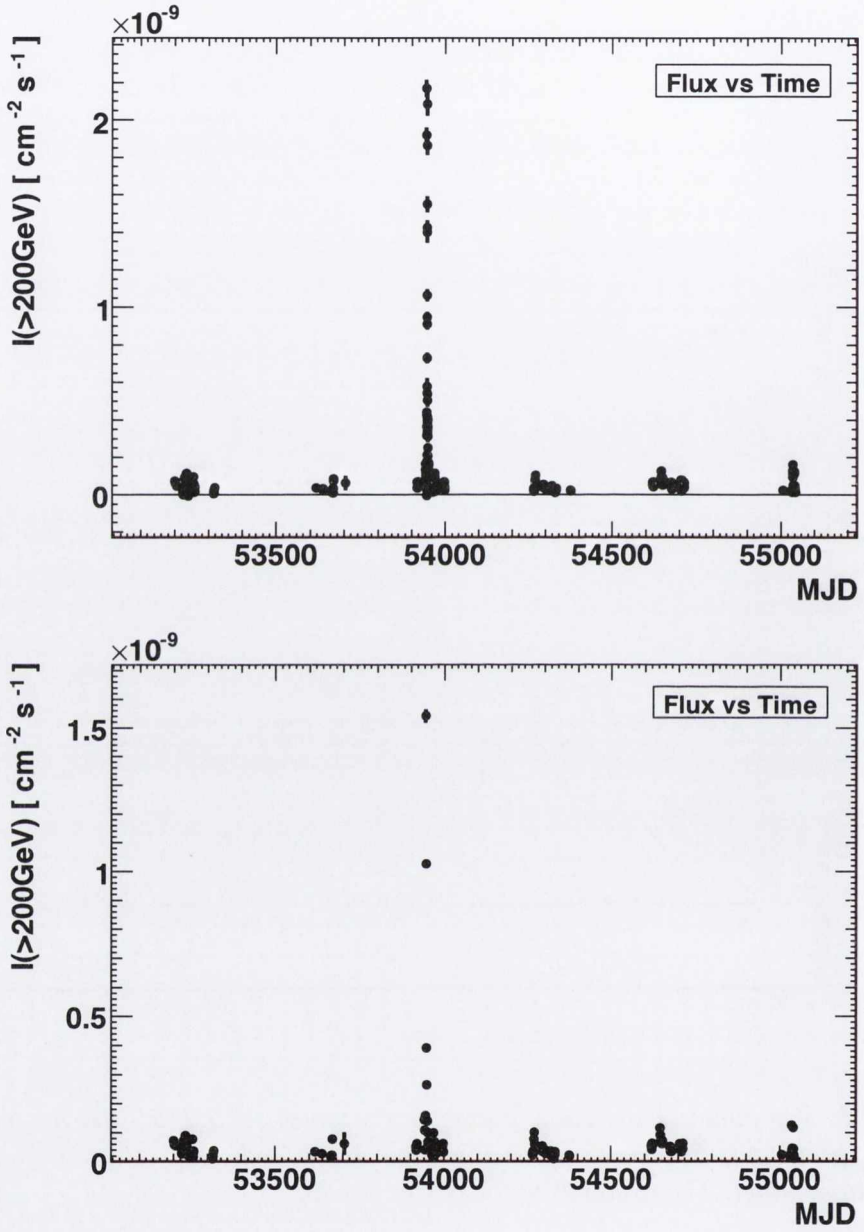

Figure 4.6: *Integral flux of PKS 2155-304 above an energy of 200 GeV versus time (lightcurve) for different time-scales. Upper Panel: 28 min/run. Lower Panel: Nightly averaged. The exceptional flare from this source is clearly visible ~MJB 53946.*

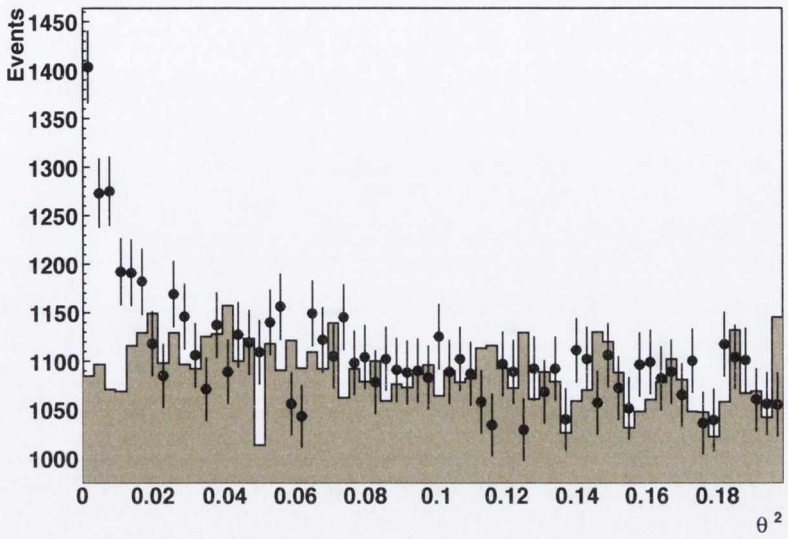

Figure 4.7: *The distribution of θ^2 for on-source events (points) and the normalised off-source events (shaded) from observations of 1ES 1101-232.*

Conclusions:
This well studied BL Lac object has provided vast amounts of good quality data over the past number of years for the H.E.S.S. collaboration. Given the possibility to divide this tremendous data set into quiescent and flaring states, a more detailed analysis was possible, as well as the opportunity to conduct systematic studies. These systematic studies are described in Section 4.4.

Due to the vast amount of data available (> 200 hours), we have excellent statistics for PKS 2155-304. Although not the most ideal candidate for a pair halo search, this source proves to be very beneficial in constraining the intergalactic magnetic fields, as will be shown in Chapter 5.

4.2 1ES 1101-232

Emission from 1ES 1101-232 was first detected by the Ariel-5 X-ray satellite in the late 1970's. The HEAO-1 source H 1101-232 was later correctly identified as a BL Lac object, using the optical and radio counterparts (Buckley et al. 1985; Remillard et al. 1989). The name 1ES 1101-232 comes from the Einstein slew survey (Elvis et al. 1992) and is now the most commonly used name for this source.

This blazar was first observed with the H.E.S.S. array in 2004 at VHE energies (E > 10^{11} eV) (Aharonian et al. 2007c). Its redshift was determined to z = 0.186 (Falomo et al. 1994),

hosted by an elliptical galaxy with an estimated magnitude $m_R = 16.41$, one of the brightest BL Lac hosts known so far. It is also one of the very few with significantly boxy isophotes (Falomo & Ulrich 2000), which indicates extra dust components or a possible merger process. The optical emission from 1ES 1101-232 has typically varied on a monthly timescale (Remillard et al. 1989). Optical flares on daily timescales have also been claimed to be observed (Romero et al. 1999).

The VHE Spectral Energy Distribution (SED) of 1ES 1101-232 exhibits a very hard spectrum, with emission into the > TeV regime. A standard emission scenario can be used to essentially explain the broadband data of 1ES 1101-232, if the EBL used to de-absorb the VHE data is at or below a value (Aharonian et al. 2006c) :

$$\nu F_\nu(1.5\mu\text{m}) = 14\text{nWm}^{-2}\text{sr}^{-1}.$$

4.2.1 H.E.S.S. Data Set and Data Reduction

The H.E.S.S. observations of 1ES 1101-232 were carried out between February 2004 and January 2008. This amounts to a total of 67.2 hours (144 runs) of good quality data for this source, recorded at zenith angles ranging from 0° to 60°, with a mean zenith angle of ~ 22°. The analysis energy threshold for these observations is ~ 200 GeV. The data was recorded in *wobble mode* with a pointing offset of ± 0.5° to the nominal source position to allow simultaneous background estimation. As with the other two sources, the data has been analysed with a standard Hillas analysis as described in Aharonian et al. (2006d).

An excess of 785 γ-ray candidates was found corresponding to a statistical significance of 10.87 standard deviations (see Figures 4.7 and 4.9). The extension of the excess is reasonably point-like. The differential energy spectrum of the source is shown in Figure 4.10. It is well described (χ^2/d.o.f = 2.6/4) by a power law $dN/dE = \Phi_0(\text{E}/1\text{TeV})^{-\Gamma}$ with a normalisation $\Phi_0 = (4.06 \pm 0.58_{stat} \pm 1.0_{sys}) \times 10^{-13}$ cm^{-2}s^{-1}TeV^{-1} and a photon index $\Gamma = 2.98 \pm 0.17_{stat} \pm 0.1_{sys}$. The integral flux above 200 GeV taken from the spectral fit is $\Phi(\text{E} > 200\text{ GeV}) = (4.9 \pm 1.2) \times 10^{-12}$cm^{-2}s^{-1}. No significant variation of the VHE γ-ray flux on any time scale was found (Figure 4.11).

Conclusions:

The distant VHE blazar 1ES 1101-232 with a confirmed redshift of $z = 0.186$, exhibits a hard spectrum with a photon index of $\Gamma \approx 2.9$ between 0.2 and 0.4 TeV. Both of these facts taken together make this source a very suitable candidate for this study.

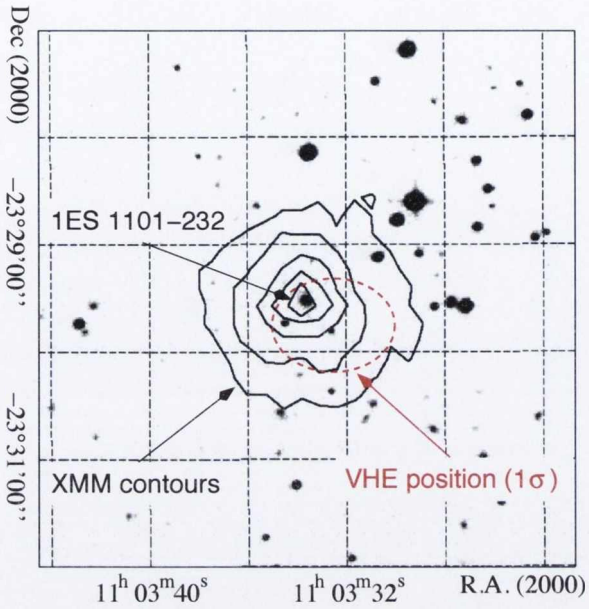

Figure 4.8: *Sky map of the region surrounding 1ES 1101-232. An R-band image made by the Anglo-Australian observatory with the UK Schmidt telescope is shown in grey-scale. The host galaxy (labelled 1ES 1101-232 in the image) of the BL Lac is resolved as an elliptical galaxy, with boxy isophotes at larger radii (see Falomo & Ulrich 2000).*

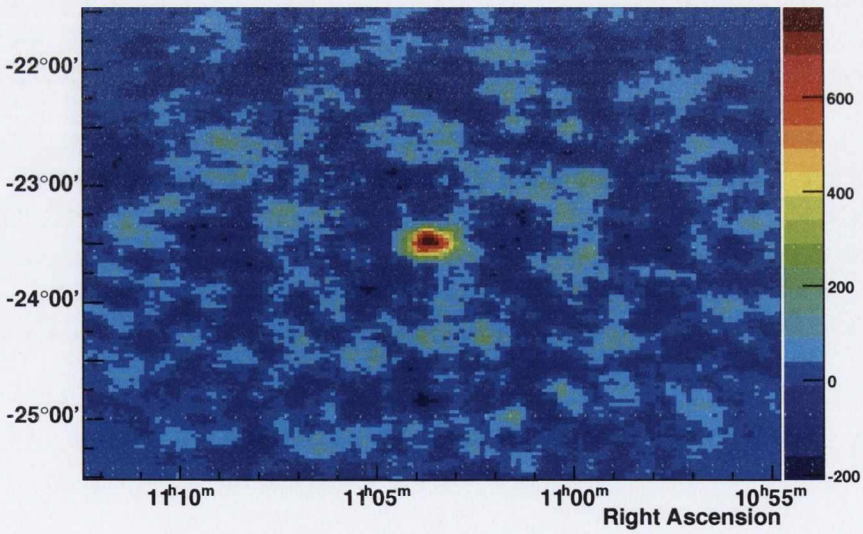

Figure 4.9: *Sky map of the VHE γ-ray excess events centred on the position of 1ES 1101-232. A clear excess is visible at the centre of the map, which has co-ordinates of Right Ascension versus Declination. Right-hand scale is the number of excess events.*

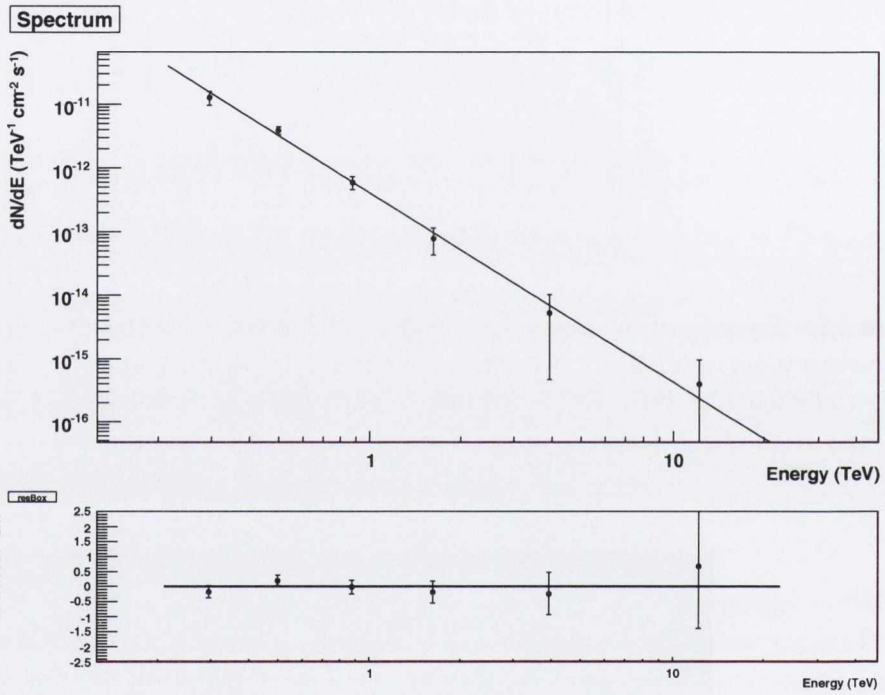

Figure 4.10: *Top Panel: Differential energy spectrum of 1ES 1101-232. The spectrum is well described by a power law with a photon index of* $\Gamma = 2.97 \pm 0.17_{stat} \pm 0.1_{sys}$ *(black line). Bottom panel: The residuals to the power law fit.*

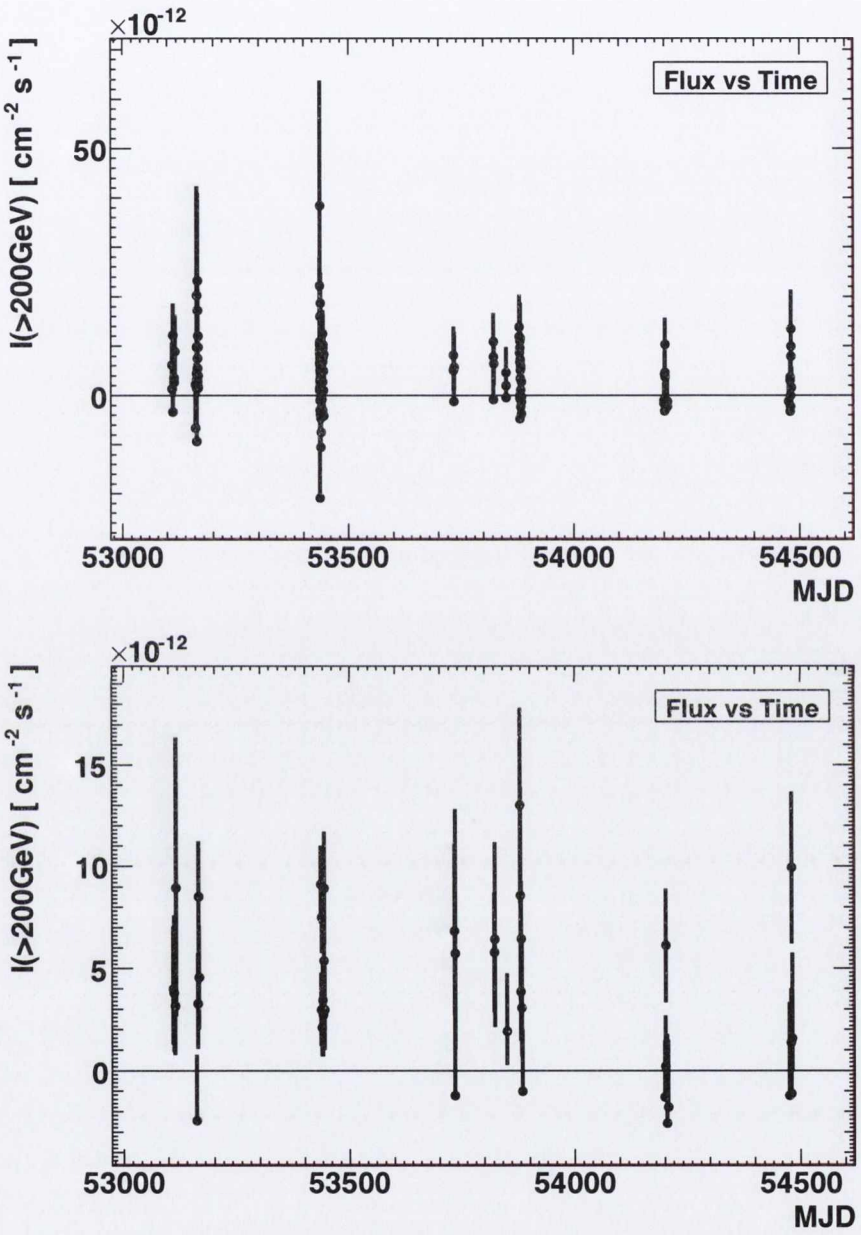

Figure 4.11: *Integral flux of 1ES 1101-232 above an energy of 200 GeV versus time (lightcurve) for different time-scales. Upper Panel: 28 min/run. Lower Panel: Nightly averaged.*

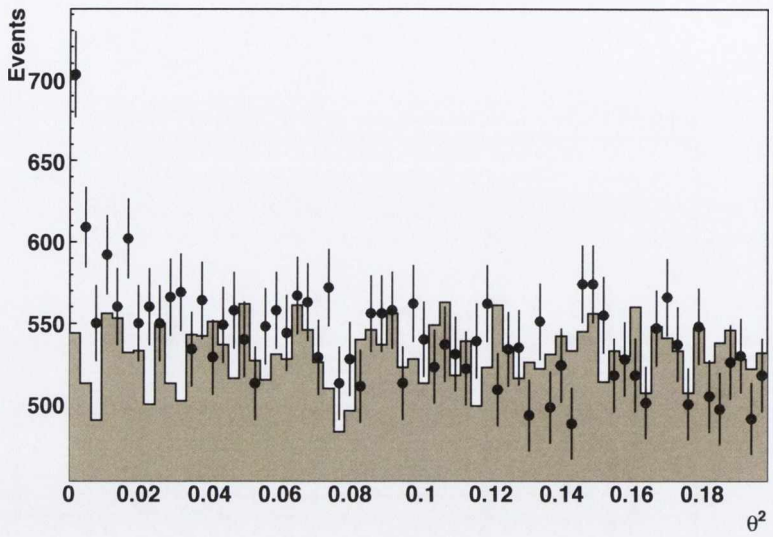

Figure 4.12: *The distribution of θ^2 for on-source events (points) and normalised off-source events (shaded) from observations of 1ES 0229+200.*

4.3 1ES 0229+200

This Active Galactic Nucleus was initially discovered by the Einstein Slew Survey (Elvis et al. 1992) and it was later identified as a BL Lac object (Perlman et al. 1996). It is located at $\alpha_{J2000} = 2^h32^m48.62^s$, $\delta_{J2000} = 20°17'17.45"$ (Rector et al. 2003) and has a redshift of $z = 0.139$ (Woo et al. 2005). This source was first observed by H.E.S.S. in late 2004 and was detected with a signal of 6.6σ (Aharonian et al. 2007a). This was the first confirmed detection of VHE γ-rays from this source. It is interesting to note that the blazar 1ES 0229+200 is not listed in the *Fermi* LAT two-year catalogue of detected sources (The Fermi-LAT Collaboration 2011), with only upper limits on the source flux derived from the LAT data (Taylor et al. 2011) and a weak detection reported by Orr et al. (2011).

Apart from 1ES 1426+428 (Aharonian et al. 2003a), 1ES 0229+200 is the only source at redshift $z > 0.1$ whose spectrum has been measured up to 10 TeV. The H.E.S.S. data shows no evidence for significant variability on any time scale. Similarly to 1ES 1101-232, this source also exhibits a very hard intrinsic spectra, which implies heavy absorption at higher energies, hinting at possible pair halo formation. The observed spectrum is characterised by a hard power law from 500 GeV to $\sim$ 15 TeV.

Due to the very high energy range observed and the hardness of the spectrum, along with

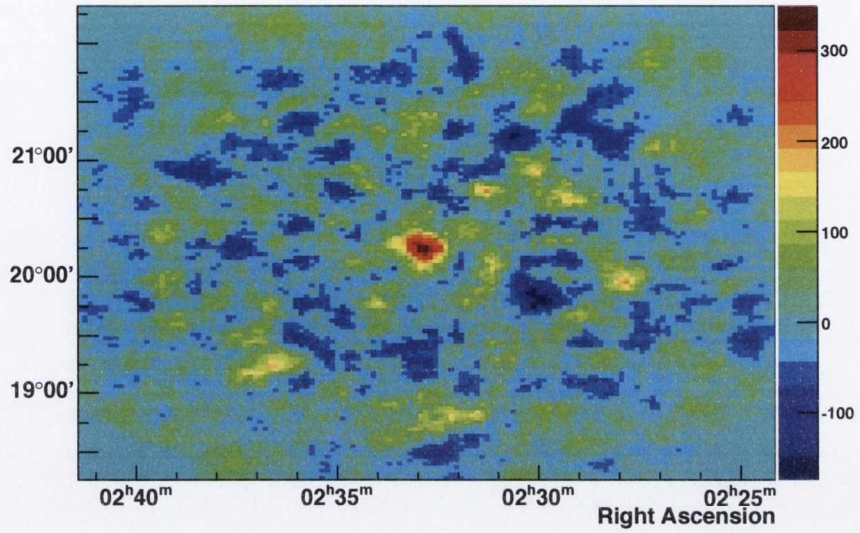

Figure 4.13: *Sky map of the VHE γ-ray excess events centred on the position of 1ES 0229+200 in Right Ascension and Declination co-ordinates. A clear excess is visible at the centre of the map.*

the relatively large redshift of the source, it was possible to develop the strongest constraints to date on the density of the Extragalactic Background Light in the mid-infrared band (Aharonian et al. 2007a). that for all EBL models, the intrinsic spectrum of 1ES 0229+200 is hard, therefore locating the high-energy peak of its spectral energy distribution above a few TeV.

As well as being used for EBL studies, 1ES 0229+200 has been an essential source used to probe the strength of the intergalactic magnetic fields (e.g. Taylor et al. 2011; Neronov & Vovk 2010; Tavecchio et al. 2010). At the same time, these hard spectra observations are challenging for blazar models and on-going studies are being carried out (see Zacharopoulou et al. 2011; Aharonian et al. 2008b and the references therein). The spectra of TeV blazars such as 1ES 0229+200, once corrected for absorption in the EBL, appear unusually hard, which poses some serious challenges to conventional acceleration and emission models.

1ES 0229+200 is defined as a high-frequency peaked BL Lac object and the measured synchrotron emission peaks at higher frequencies (> 100 keV) than usual for HBL and belongs therefore to the class of extreme blazars. The exact frequency peak cannot be determined since the hard X-ray spectrum does not show any significant cut-off. However, 1ES 0229+200 has the highest Inverse Compton peak frequency among extreme blazars known to date.

Here the analysis of VHE γ-rays with energies above 200 GeV from 1ES 0229+200 with the H.E.S.S. Cherenkov telescope array is reported.

4.3.1 H.E.S.S. Data Set and Data Reduction

The H.E.S.S. observations of 1ES 0229+200 were carried out between September 2004 and November 2009. This amounts to a total of 79.3 hours (170 runs) of good quality data for this source, recorded at zenith angles ranging from 42° to 52°. The analysis energy threshold for these observations is 200 GeV. The data was recorded in *wobble mode* with a pointing offset of ± 0.5° to the nominal source position to allow simultaneous background estimation. The data has been analysed with a standard Hillas analysis as described in Aharonian et al. (2006d).

An excess of 320 γ-ray candidates was found corresponding to a statistical significance of 6.3 standard deviations (Figures 4.13 and 4.12). The extension of the excess is reasonably point like. The differential energy spectrum of the source is shown in Figure 4.14. It is well described (χ^2/d.o.f = 7.9/4) by a power law $dN/dE = \Phi_0(\mathrm{E}/1\mathrm{TeV})^{-\Gamma}$ with a normalisation $\Phi_0 = (4.96 \pm 0.84_{stat} \pm 1.0_{sys}) \times 10^{-13}$ cm^{-2}s^{-1}TeV^{-1} and a photon index $\Gamma = 2.66 \pm 0.17_{stat} \pm 0.1_{sys}$. The integral flux above 200 GeV taken from the spectral fit is $\Phi(\mathrm{E} > 200\ \mathrm{GeV}) = (4.3 \pm 1.1) \times 10^{-12}$cm^{-2}s^{-1}. No significant variability was detected on run-wise or nightly time scales (see Figure 4.15).

Conclusions:

With its location at a redshift of $z = 0.139$, its capacity to emit VHE γ-rays in the > TeV regime and its very hard intrinsic spectrum, 1ES 0229+200 is one of the most suitable candidates available to the H.E.S.S. system in a search for extended pair halo emission.

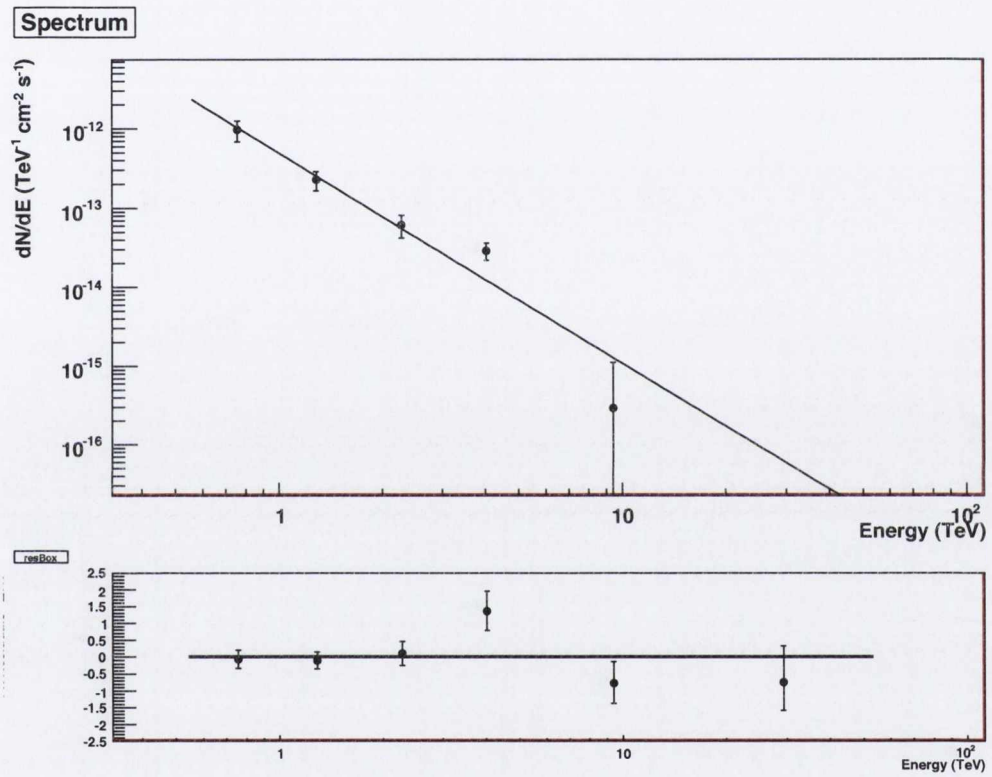

Figure 4.14: *Top Panel: Differential energy spectrum of 1ES 0229+200. The spectrum is well described by a power law with a photon index of* $\Gamma = 2.66 \pm 0.17_{stat} \pm 0.1_{sys}$ *(black line). Bottom panel: The residuals to the power law fit.*

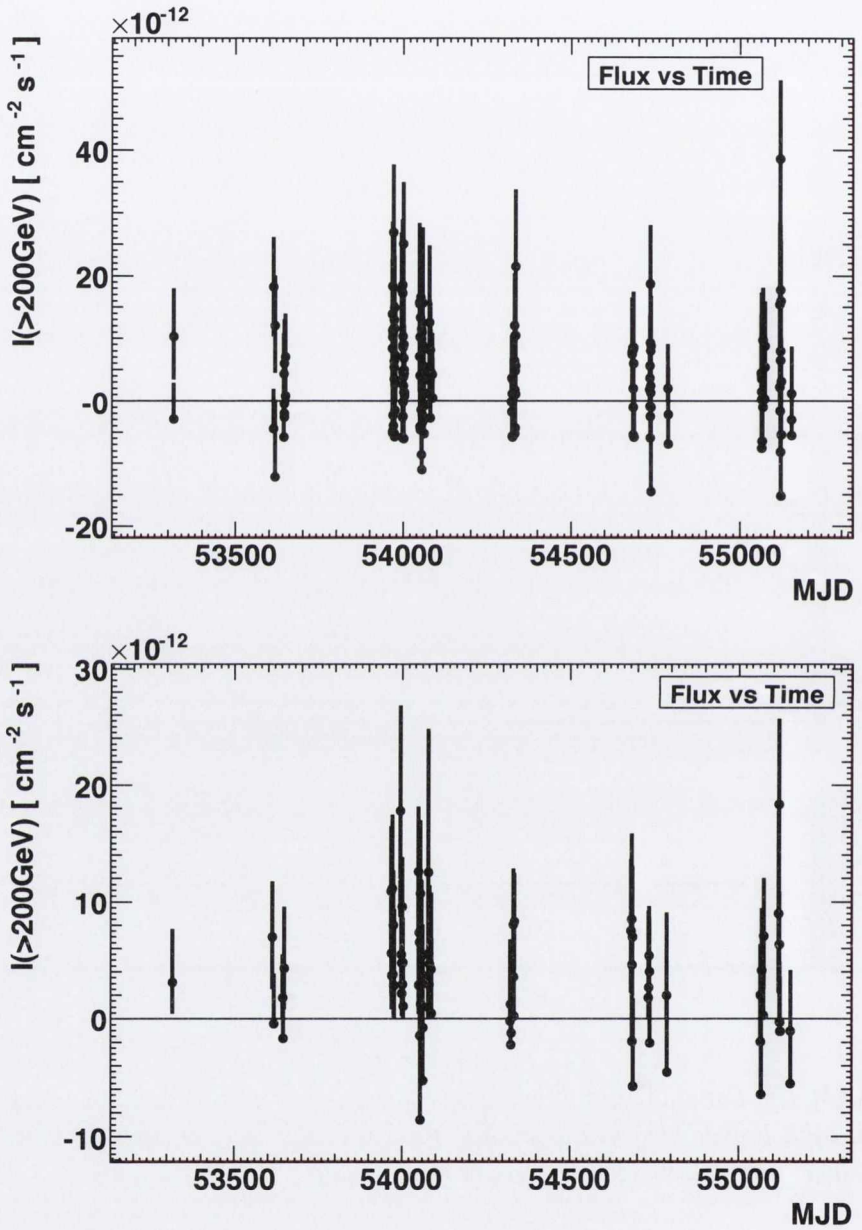

Figure 4.15: *Integral flux of 1ES 0229+200 above an energy of 200 GeV versus time (lightcurve) for different time-scales. Upper Panel: 28 min/run. Lower Panel: Nightly averaged.*

4.4 Systematic Study Of The H.E.S.S. Point Spread Function (PSF)

In our search for extended Pair Halo emission, one of the prime sources studied in detail was PKS 2155-304. In 2006, there was an exceptional flare from this source, (Aharonian et al. 2007b) where the average VHE flux observed by H.E.S.S. was more than 10 times its typical value and varied on minute timescales. Causality requires that PKS 2155-304 is a point-like source for H.E.S.S. during the flare state, which makes it an ideal candidate for this study. Another advantage of using the flare to study systematics, is the exceptionally good signal/noise ratio we obtained for this data set.

4.4.1 Efficiency Effects

The optical efficiency of the H.E.S.S. telescopes changes over time, due to the degradation of the mirror reflectivity, as well as other effects. This effect is seen as a reduction in the image intensity for each event, compared to the intensity expected from the Monte Carlo simulations. This leads to a shift in the absolute energy scale of the detector, as events are reconstructed with energies which are too low. This effect is then corrected for spectral studies by incorporating a scaling factor in the energy estimation for each event (seeAharonian et al. 2006d). Phase 1 of the H.E.S.S. system was completed in late 2003. In the H.E.S.S. analysis framework, the set of selection cuts and Monte-Carlo simulations which represent the efficiencies of this era of operation are the "0510" cuts with a mean muon efficiency factor of 0.1054 photoelectrons/photon. To account for the reduced optical efficiency of the telescope mirrors and light cones, by around 2007 a new set of simulations which have a reduced muon efficiency (0.07249) were introduced. These cuts/simulations are known as "phase 1b" or "_1b". These Monte Carlo angular distributions are our best estimate of the H.E.S.S. PSF. As part of our systematic checks the H.E.S.S. PSF was compared for both the phase 1 and phase 1b simulations.

If no reconstructed energy cut is made, then the primary difference between the two simulated data sets is the intrinsic fluctuations of showers at the two slightly different mean energies. Assuming $N_e \sim E$ and fluctuations to scale as $1/\sqrt{N_e}$ one might expect an improvement in the PSF as the energy scale is shifted upwards by $\sim \sqrt{\epsilon_{1b}/\epsilon_1} \sim 0.82$ (or an 18% improvement).

The 68% containment radius for the PKS 2155-304 flare data set Phase 1 (blue) simulations is 0.118°, compared to a value of 0.104° for Phase 1b (red). This is close to the expected improvement due to the reduced shower fluctuations.

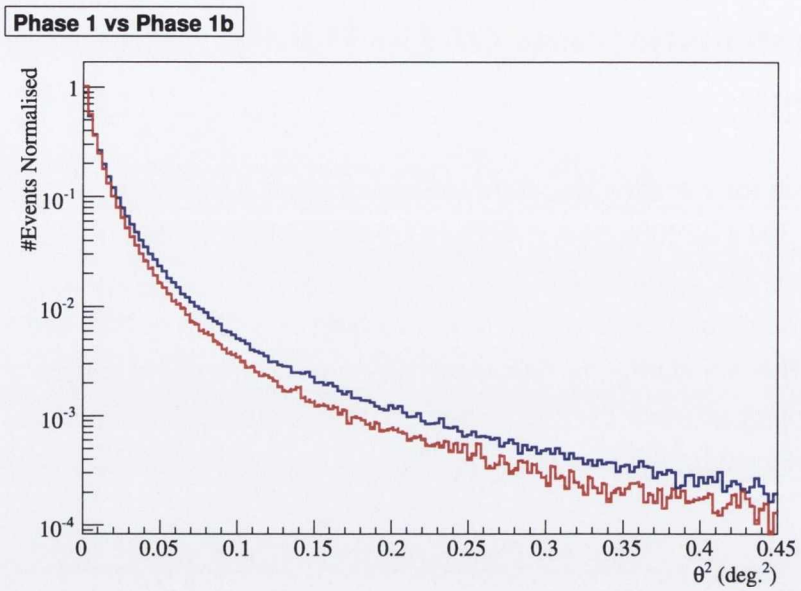

Figure 4.16: *The blue curve is the Monte Carlo Phase 1, with Phase 1b represented by the red curve.*

As can be seen in Figure 4.17, Phase 1b slightly over-estimates the reconstructed energies. A scaling factor of 0.961 was utilised, taken from Meyer, Horns & Zechlin (2010), to see if this would improve the fit. The dashed red line in Figure 4.17 is in much better agreement with the data points, consistent with the conclusions of Meyer et al.

Efficiency	Name	Photoelectrons/Photon
ϵ_1	M.C. Phase 1	0.1054
ϵ_{1b}	M.C. Phase 1b	0.0725
ϵ_{flare}	PKS 2155-304 flare	0.0741
ϵ_{low}	PKS 2155-304 low state	0.0721
ϵ_{1101}	1ES 1101-232	0.0785
ϵ_{0229}	1ES 0229+200	0.0675

Table 4.1: *Optical efficiencies for various Monte Carlo simulations.*

4.4.2 Broken Pixels

In an attempt to see if the data quality, namely the number of broken pixels in the data set, had a significant impact on the resulting point spread function, the PKS 2155-304 flare data was carefully analysed. Only data which had events for all 4 telescopes was used. Each telescope

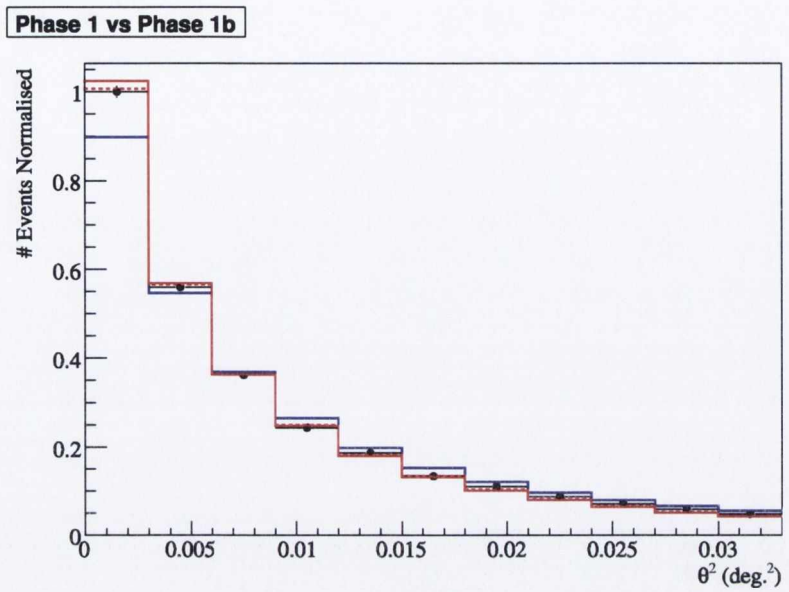

Figure 4.17: *The PKS 2155-304 flare data set is plotted (black dots), along with the Phase 1 and Phase 1b Point Spread Functions. The dashed red line represents a 4% scaling factor taken from Meyer, Horns & Zechlin Meyer et al. (2010)*

contains 960 photon detector elements (each one "pixel"). The maximum number of broken pixels allowed before the telescope is excluded from the run is 120 (or 12.5%).

Taking > 5% (or ~ 48 pixels) as a large number of broken pixels, with the data set divided accordingly. In Figure 4.18, it can clearly be seen that there is no considerable difference between the two distributions.

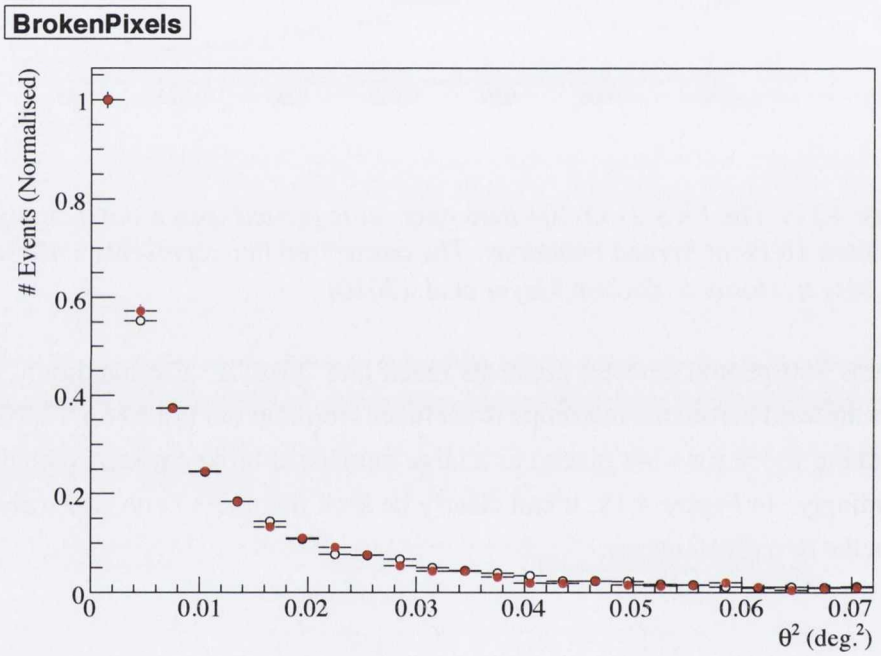

Figure 4.18: *Red points show the number of Broken Pixels < 5%, Black circles show > 5%.*

5

A Search for extended blazar emission with H.E.S.S.

Electron-positron pairs are inevitably produced following TeV γ-ray emission from blazar sources, through the interaction of these γ-rays with the Extragalactic Background Light. Depending on the magnetic fields in the proximity of the source, the cascade initiated from pair production can result in either an isotropic halo around an initially beamed source or a beam broadened cascade flux. We searched for both extended Pair Halo and Beam Broadened Cascade emission around the blazars 1ES 1101-232, 1ES 0229+200 and PKS 2155-304 using VHE data from the H.E.S.S. telescope array and HE data from the *Fermi*-LAT. By comparing the angular distributions of the reconstructed γ-ray emission to that of a point-like source, it is possible to investigate if extended emission is present. For pair halos, upper limits for extended emission calculated for each of the three sources are presented. For Beam broadened cascades, it is possible to exclude Extra-Galactic Magnetic Fields (EGMF) values in the range 3 to 9 $\times 10^{-15}$ G.

The beam broadened cascade analysis presented has been conducted in collaboraion with Andrew Taylor, based on his 3D Monte Carlo simulations. The *Fermi* analysis presented in this chapter has been carried out by Denis Malyshev.

5.1 Previous observational attempts

A first search for pair halo emission was conducted by the HEGRA collaboration (Aharonian et al. 2001b) using Mrk 501 (z = 0.033). This yielded an upper limit of 5 - 10 % of the Crab Nebula flux (at energies $\geq$ 1TeV) on angular scales of 0.5° to 1° from the source.

The MAGIC collaboration performed a similar search for extended emission using Mrk 421 and Mrk 501 (Aleksić et al. 2010a). From their analysis, they obtained upper limits on the extended emission around Mrk 421 at a level of < 5 % of the Crab flux and a value of < 4 % of the Crab was achieved for Mrk 501, both above an energy threshold of 300 GeV. They used these results to constrain the extragalactic magnetic field strength to be a few times 10^{-15} G. More recently, a new study was performed using data from the *Fermi*-Large Area Telescope (LAT) (Ando & Kusenko 2010). Images from the 170 brightest Active Galactic Nuclei in the 11 month *Fermi* source catalogue were stacked together. Evidence has been claimed for beam broadened cascades, in the form of an excess over the point-spread function with a significance of 3.5 σ. However, Neronov et al. (2011) indicated that the angular distribution of γ-rays around the stacked AGN is consistent with the angular distribution of the γ-rays around the Crab Nebula, which is a point-like source for *Fermi*.

From a theoretical perspective, a detailed study of very high energy γ-rays from pair halo emission was conducted by Eungwanichayapant & Aharonian (2009). A very comprehensive study which investigated the dependence of the radiation from pair halos, in relation to the energy spectrum of the primary γ-rays, the redshift of the source, as well as the flux of the extragalactic background light, is described.

In this chapter, a search for a TeV γ-ray pair halo and beam broadened cascade surrounding known VHE sources, using the H.E.S.S. experiment, is described. Three AGN have been chosen, 1ES 1101-232, 1ES 0229+200 and PKS 2155-304, using data from 2004 to 2009. These AGN were chosen because they show spectra with no clear upper energy cutoff. It is thus very likely that they have emission extending into the > TeV energy domain.

5.2 Data Sets and Analysis

5.2.1 H.E.S.S. Observations

The H.E.S.S. experiment has been in operation since June 2002 and is located in the Khomas Highlands of Namibia (23° 16' 18" S, 16° 30' 1" E), 1835 m above sea level (Hinton 2004). It is an array of four Imaging Atmospheric Cherenkov Telescopes (IACT) which detects cosmic γ-rays in the 100 GeV to 100 TeV energy range. The four H.E.S.S. telescopes are placed in a square formation with a side length of 120 metres. The effective mirror surface area per

telescope is 107 m^2. The total field of view of the detector is 5° in diameter.

For this analysis, the standard H.E.S.S. data quality selection criteria (Aharonian et al. 2006d) were applied to the dataset of each source. The further criterion that only runs which had data from all 4 telescopes was imposed, to improve the overall angular resolution. The Reflected-Region method (Aharonian et al. 2006d) was used for the estimation of the background.

For our analysis we have focused on the observations of three different VHE sources: 1ES 1101-232, 1ES 0229+200 and PKS 2155-304. Both 1ES 1101-232 and 1ES 0229+200 have been chosen for this study due to their very hard intrinsic spectra and their emission in the > TeV energy range. With ~ 170 hours of good quality data, a suitable redshift and very high energy γ-ray emission, PKS 2155-304 is also an excellent candidate for this search. A summary of the results from this analysis can be found in Table 5.1.

5.2.1.1 1ES 1101-232

This blazar was first discovered by the H.E.S.S. array in 2004 at VHE energies (Aharonian et al. 2007c). 1ES 1101-232 resides in an elliptical host galaxy at a redshift of $z = 0.186$ (Falomo et al. 1994). The luminosity of the host galaxy is very high, with an absolute magnitude, M_R = -24.45, classifying this galaxy among the brightest hosts of BL Lac objects (Falomo & Ulrich 2000). BL Lacs are often located in regions of higher than average galaxy density and on average are associated with groups or poor (Abell richness class 0) clusters (Falomo & Pesce 1994). A total of 66.3 hours (142 runs of ~ 28 min each) of good quality data have been analysed, taken between 2004 to 2008, resulting in a detection exceeding 10σ.

5.2.1.2 1ES 0229+200

This source was first observed by H.E.S.S. in late 2004 and was detected with a signal of 6.6σ (Aharonian et al. 2007a). The HBL is hosted by an elliptical galaxy, located at a redshift of z = 0.140 (Woo et al. 2005). A total of ~ 80h of data taken between 2004 and 2009 were used for this analysis. This is a prime source for such studies due to its hard intrinsic spectrum reaching beyond 10 TeV (Dolag et al. 2011; Tavecchio et al. 2010; Vovk et al. 2012b).

Source Name	Distance (z)	T_{live} (hours)	N_{ON}	N_{OFF}	Excess	σ	Z_{mean} (deg.)	ψ_{mean}	MJD–50000	U.L. (> 1TeV) ($cm^{-2}s^{-1}TeV^{-1}$)
1ES 1101-232	0.186	11	79426	78636	790	67	22	0.6	3110 – 4482	1.837e-12
1ES 0229+200	0.140	6.6	39569	38752	817	79	45	0.56	3316 – 5150	1.188e-12
PKS 2155-304$_{Lowstate}$	0.117	164.5	200374	168685	31689	52.2	19	0.56	3199 – 5042	2.239e-12
PKS 2155-304$_{Flare}$	0.117	5.6	17440	6041	11399	78	21	0.56	3945 – 3947	-

Table 5.1: *Summary of the standard H.E.S.S. analysis results for 1ES 1101-232, 1ES 0229+200 and PKS 2155-304. The redshift, live-time, the number of ON and OFF source events, the excess and its significance, mean Zenith angle, mean offset, the range of the Modified Julian Date (MJD) for the observations and the pair halo upper limits for each source are reported.*

5.2.1.3 PKS 2155-304

Located at a redshift of z = 0.117, PKS 2155-304 was first detected by the Durham telescopes in 1999, with a statistical significance of 6.8 standard deviations (Chadwick et al. 1999). This source is located in a poor cluster of galaxies (Falomo et al. 1993) and a companion galaxy is visible (Kotilainen et al. 1998). The H.E.S.S. array detected this source in 2003 with high significance ($> 100\sigma$) at energies greater than 160 GeV (Aharonian et al. 2005b). For this study, approximately 170 hours of good quality data have been analysed, taken between 2004 and 2009.

In 2006, this source underwent a giant outburst (Aharonian et al. 2009a), with a flux level (> 200 GeV) ~ 7 times that observed from the Crab Nebula. We have chosen to look at this exceptional outburst separately from the rest of the data, creating two data sets: high state (i.e. the flare) and low state. Removing the flare from the main data set allows us to focus on this source in a low state, where a halo should be more visible. The data set for the low state amounts to ~165 hours, only including data of good quality. Focusing solely on the exceptional flare from 2006, we have a data set of 34 runs (~16 hours). These observations were taken during the nights of July 29th to 31st 2006 (3 nights in total).

PKS 2155-304 Flare : In our search for extended pair halo emission, one of the prime sources we studied is the blazar PKS 2155-304. In 2006, the exceptional flare from this source exhibited an average VHE flux observed by H.E.S.S. more than 10 times its typical value and varied on minute timescales. Causality requires that PKS 2155-304 is a point-like source for H.E.S.S. during the flare state, which makes it an ideal candidate for the study of systematics. The flare data set, fitted with the H.E.S.S. point spread function (PSF) from Monte Carlo simulations, can be seen in Figure 5.1, with a $\chi^2/n_{d.o.f.} = 91/72$, with a $P(\chi^2)$ of 0.06. As can be seen from the residuals in the lower panel of Figure 5.1, only small systematics are involved. Another advantage of using the flare to study systematics, is the exceptionally good signal/noise ratio we obtained for this data set.

5.2.1.4 H.E.S.S. Analysis Methods

All H.E.S.S. data passing the quality selection criteria are processed using the standard H.E.S.S. calibration (Aharonian et al. 2004a). *Standard cuts* (Benbow 2005) are used for the event selection criteria and the data was analysed with the H.E.S.S. Analysis Program, version HAP-10-06. The *Reflected Region* method (Aharonian et al. 2006d) was used to estimate the cosmic-ray background. The significance (in standard deviations, σ) of the observed excess was calculated using Equation (17) in Li & Ma (1983). All upper limits are determined following the method of Feldman & Cousins (1998).

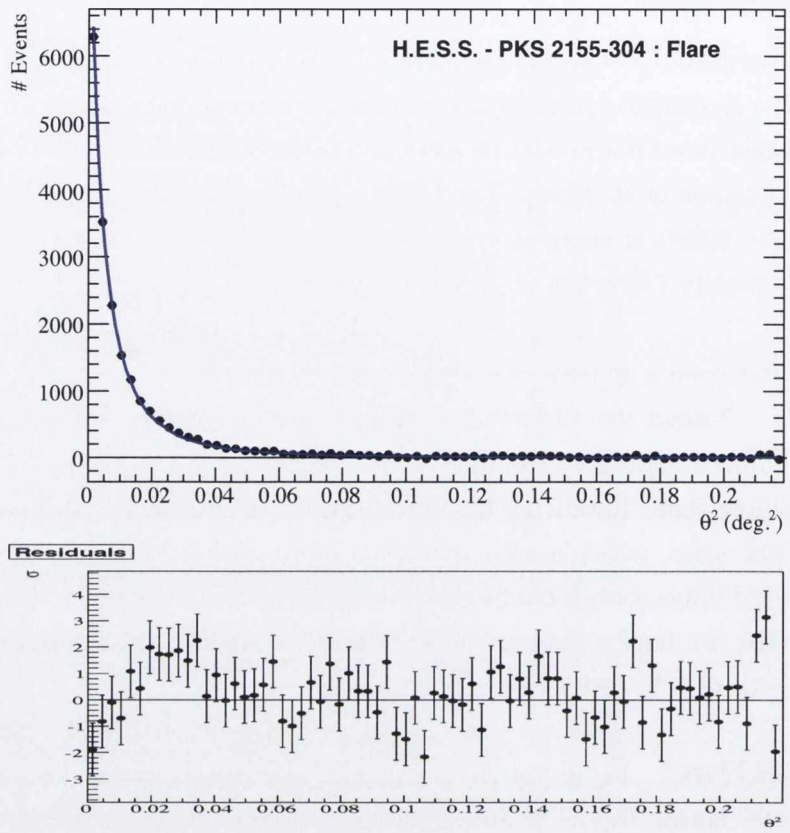

Figure 5.1: *PKS 2155-304 flare data set fitted with the H.E.S.S. point spread function (blue) from Monte Carlo simulations, resulting in a* $\chi^2/n_{d.o.f.} = 91/72$*, with a* $P(\chi^2)$ *of 0.06. The fit residuals are shown in the lower panel.*

The arrival direction of every event can be estimated quite successfully using stereoscopic arrays of multiple IACTs and can be reconstructed with a precision of ~ 0.1 degree. The distribution of the squared angular distance between the reconstructed shower position and the source position (θ^2) is narrow and peaked at $\theta = 0$, for a point-like source. However, for more extended emission, this distribution will be broader. From Figure 5.1, it can be seen that the angular distribution of the flare events are in excellent agreement with the PSF, and therefore consistent with a point-like source.

The results presented below have been successfully cross-checked with an independent analysis, *the Model Analysis* (de Naurois & Rolland 2009), which yields consistent results.

5.2.2 *Fermi* - LAT analysis

The *Fermi* Gamma-ray Space Telescope, launched in 2008, observes the 20 MeV to 300 GeV sky (Atwood et al. 2009). The *Fermi* data analysis performed in this work used the Large Area Telescope (LAT) Science Tools package v9r23p1 (updated on 1st August 2011 to include the new PSFs) with the P7SOURCE_V6 post-launch instrument response function. The standard event selection for a source analysis, resulting in the strongest background-rejection power (EVENT CLASS=2) was applied. The analysis was further restricted to the energy range above 100 MeV, where the uncertainties in the effective area become smaller than 10%.
The data used for this analysis corresponds to more than 3 years of observations (4th August, 2008- 1st September, 2011) for our three sources : 1ES 1101-232, 1ES 0229+200 and PKS 2155-304.
To produce the spectra and flux upper limit points, binnedAnalysis and UpperLimits Python modules were used, described in detail in the *Fermi* data analysis threads. To take into account a broad *Fermi* PSF at low energies, all sources from the 2 year *Fermi* point-like source catalogue (Abdo et al. 2010), closer than 10 degrees to the source position were included. Since the blazar halo is not a point-like source, but a diffuse source for *Fermi*, we used a spatial model ($\propto \theta^{-5/3}$) based on theoretical estimations of the halo angular profile (Eungwanichayapant & Aharonian 2009). The energy range was split into energy bands of 100 MeV – 300 GeV over 10 logarithmically equal energy bins and in each bin performed the spectral analysis, fixing the power law index of each source to be -2, but leaving their normalisation free. The normalisations for galactic and extragalactic backgrounds were also left free in each energy bin. PKS 2155-304 and 1ES 1101-232 are detected in the dataset above an energy threshold of 100 MeV which significances of 100 and 5.5 sigma respectively. 1ES 0229+200 yields a TS value of $\sim$ 10 which corresponds to a significance of about 3 sigma. The recent results on 1ES 0229+200 presented in Vovk et al. (2012b) are in the agreement with the results presented in this paper. The small discrepancy of the results at low ($\sim$ 1 GeV) energies can be explained by different size of the considered region. In this case this discrepancy should be treated as a systematic error. However, for a weak *Fermi* source 1ES 0229+200 this systematic is significantly smaller than statistical error and thus can be ignored.

The pair halo emission was modelled as an extended object with spatial profile as described above. The binned *Fermi* analysis was performed at energies 300 MeV – 300 GeV for the models with and without halo contribution. In all considered cases, the model with the halo have similar log-likelihood values to the model without a halo component. Thus we conclude that no significant indications for pair halo emission are found.

No significant indications for pair halo emission are found for any of the above sources and the upper limits for the fluxes are shown in Figure 5.7. The spectra of central sources can be

well fitted with a single power law model with an index of $\Gamma = 1.87 \pm 0.05$ for PKS 2155-304, $\Gamma = 1.82 \pm 0.05$ for 1ES 1101-232 and $\Gamma = 1.44 \pm 0.57$ for 1ES 0229+200, with only statistical errors given. These spectral indices are in good agreement with results from the Second Fermi LAT Catalog (2FGL).

5.3 Pair Halo Analysis

Two separate techniques have been used to calculate pair halo (PH) upper limits, a model independent method and a model dependent method.

5.3.1 Model Dependent

In the paper by Eungwanichayapant & Aharonian (2009), a detailed study of the formation of PH have been conducted. In particular, they investigated the spectral and angular distributions of PH in relation to the redshift of the central source, the energy spectrum of the primary γ-rays and the flux of the extragalactic background light. In this work, it is assumed that the magnetic field in the intergalactic medium was sufficiently small so that the synchrotron cooling of electrons could be neglected. However, it was also assumed that the magnetic field was sufficiently large so that the secondary electrons of all relevant energies were isotropised before they interacted with ambient photons. These two conditions are safely satisfied for a broad range of the intergalactic magnetic fields between 10^{-7} G to 10^{-12} G. Here, the theoretically predicted angular distribution is used to derive limits on a possible PH flux. The differential angular distribution of a PH at $z \approx 0.13$ and $E_\gamma > 100$ GeV, which best suits our data, was taken from Figure 6 of their paper. This profile is based on mono-energetic injected primary γ photons of energy $E_0 = 100$ TeV. This provides a PH gamma photon index similar to that coming from a power law index of $\Gamma = 1.5$. For these calculations, the Primack et al. (2001) EBL model was used.

The resulting angular distribution follows a profile of $dN/d\theta \propto \theta^{-5/3}$. Using this spatial model, the "maximum halo excess" for each source (i.e. how much of a halo component can we add to the overall shape) at the 95% confidence level, was estimated (with $n_{d.o.f.} = 72$).

A 'halo function' is created for the measured θ^2 distribution consisting of the PSF and the PH emission taken from Eungwanichayapant & Aharonian (2009) (i.e. $N(\theta^2) = N(\theta^2)_{PSF} + N(\theta^2_{PH})$). The PSF normalisation was left free and the number of excess events in the PH model were increased until the fit had a probability < 0.1. The differential limit was then calculated by dividing the maximum number of halo events by the overall exposure, which assumes a spectral index. This method was repeated for two different values of the spectral index, 2.5 (red lines)

and 1.5 (blue lines).

5.3.2 Model Independent

In the model independent approach, the residual emission after point source subtraction is used to derive an upper limit on the PH contribution. The region between the vertical dashed lines, $0.0125 < \theta^2 < 0.2$ (see Figure 5.2) is taken to be the region where the halo is most dominant. The expected contamination from the point-like source into the halo region is calculated, using the PSF as an estimation of a point-like source. The contamination is calculated by taking the integral of the region between the vertical dashed lines. The Feldman Cousins Confidence Intervals (Feldman & Cousins 1998) are used to calculate the maximum halo excess. Using this method, the halo limit is calculated by determining the maximum possible halo contamination, at a 95% C.L. Similarly to the model dependent case, the differential limit was calculated by dividing the maximum number of halo events (in this case, the contamination) by the overall exposure, and the method was repeated for two different values of the spectral index.

In Figure 5.2 the results for each of the three sources are shown. The resulting flux limits for each method are listed in Table 5.2.

The upper limit on the PH emission from the two methods are shown in Figure 5.7 together with the spectral energy distribution (SED) of the sources. The numerical results listed in Table 5.2 are typically in the order < 1% of the flux of the Crab Nebula above 1 TeV. The H.E.S.S. data shown in Figures 3 and 5 are previously published H.E.S.S. data taken from Aharonian et al. (2007c), Aharonian et al. (2007a) and Aharonian et al. (2009b) respectively.

The limits of the PH γ-ray energy flux for the three blazars, may be converted into limits on the accumulated electron energy density in their surrounding regions. As an example case, we consider 1ES 0229+200, whose energy flux at 1 TeV is 10^{-13} erg cm^{-2} s^{-1}. For sufficiently strong magnetic fields ($> 10^{-12}$ G) the parent $\sim$ 20 TeV electrons are both born into and isotropised within a region $\sim$ 10 Mpc from the blazar. For such fields an upper limit on the TeV γ-ray luminosity from these regions is $\sim 4 \times 10^{42}$ erg s^{-1}. Since the electron IC cooling time on the CMB is $t^{e}_{\rm cool}(20\ {\rm TeV}) \approx 10^5$ yr, a limit on the total energy content of the parent electrons is $\sim 10^{55}$ erg. Interestingly the equipartition magnetic field for such a density is 4×10^{-11} G.

Thus, the corresponding limit on the underlying 20 TeV electron density within the 10 Mpc source region is $\sim 5 \times 10^{-11}$ eV cm^{-3}.

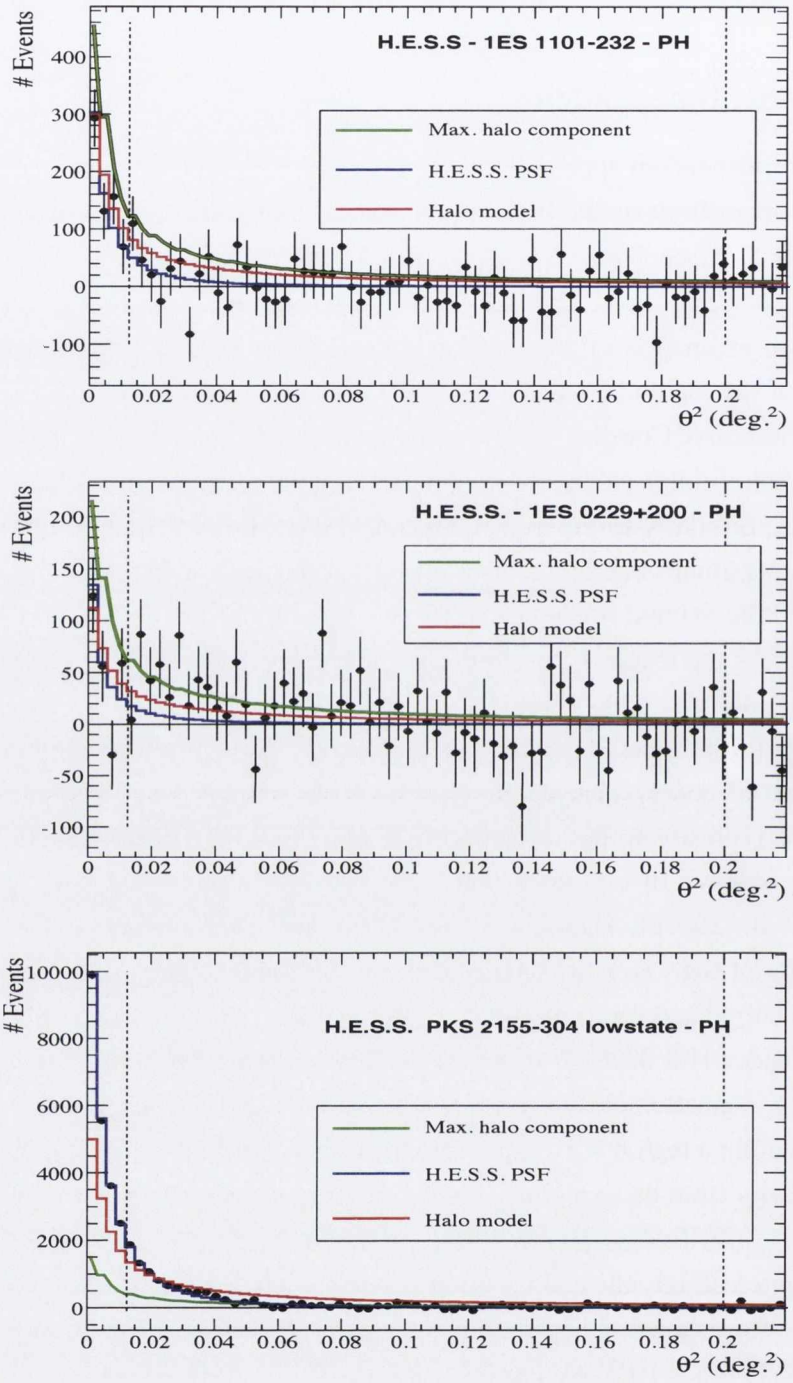

Figure 5.2: *Angular distribution of excess events of 1ES 1101-232 (top), 1ES 0229+200 (middle) and the PKS 2155-304 low state (bottom). The blue line is the H.E.S.S. PSF , the red line is the halo model and the green line is the maximum allowable halo component. The vertical dashed lines at 0.0125 denotes the standard selection cut for point-like sources used by H.E.S.S.*

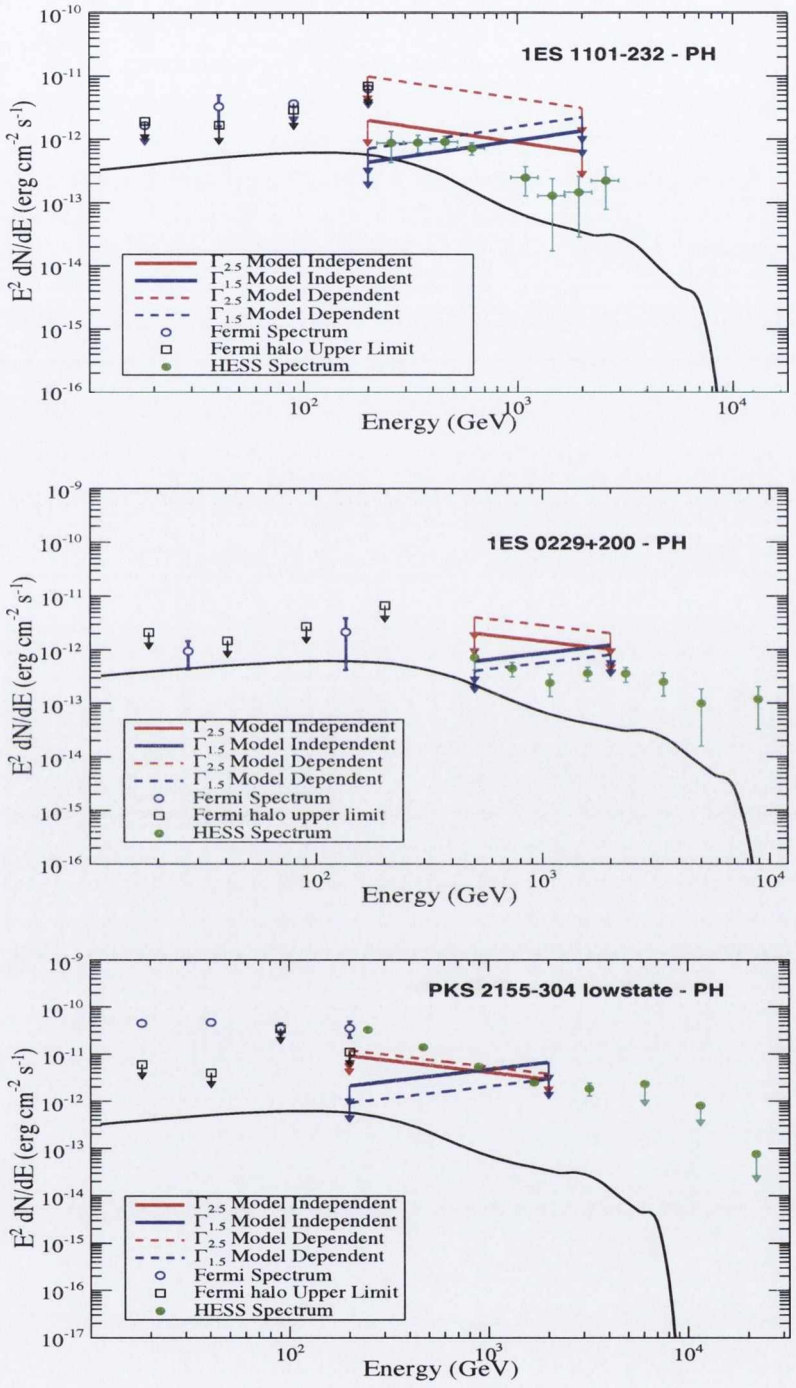

Figure 5.3: *Spectral energy distribution of 1ES 1101-232 (top), 1ES 0229+200 (middle) and PKS 2155-304 low state data sets (bottom). The H.E.S.S. data (green circles) and the Fermi data (empty circles) are shown. The upper limits on the flux contribution from a PH for the H.E.S.S. data are shown by blue and red arrows (solid lines are model independent, dashed lines are model dependent). The Fermi upper limits are shown as black squares. The black line corresponds to the halo model taken from Eungwanichayapant & Aharonian (2009).*

Source Name	Model Independent ($\Gamma_{2.5}$ / $\Gamma_{1.5}$) ($cm^{-2}s^{-1}TeV^{-1} > 1$ TeV)	Model Dependent ($\Gamma_{2.5}$ / $\Gamma_{1.5}$) ($cm^{-2}s^{-1}TeV^{-1} > 1$ TeV)
1ES 1101-232	(1.8 / 1.9) x 10^{-12}	(0.4 / 1.2) x 10^{-12}
1ES 0229+200	(1.2 / 0.7) x 10^{-12}	(0.6 / 1.1) x 10^{-12}
PKS 2155-304$_{Lowstate}$	(2.2 / 2.6) x 10^{-12}	(1.7 / 5.9) x 10^{-12}

Table 5.2: *Pair halo upper limits for 1ES 1101-232, 1ES 0229+200 and PKS 2155-304.*

5.3.3 Statistical Study

In this section, standard statistical methods are used to check the goodness of fit of the H.E.S.S. point spread function to the data. In the case of Figures 5.4 - 5.7, the top panel shows a simple log plot of the angular distributions, to enhance the visibility of the scatter. The fit residuals for each data set are presented in the middle panel. In the lower panel, the corresponding quantiles are given, fitted with a simple gaussian distribution. As can be seen from each of the quantiles, the data has a "normal" distribution in each case, with no significant deviations or signs of a notable excess.

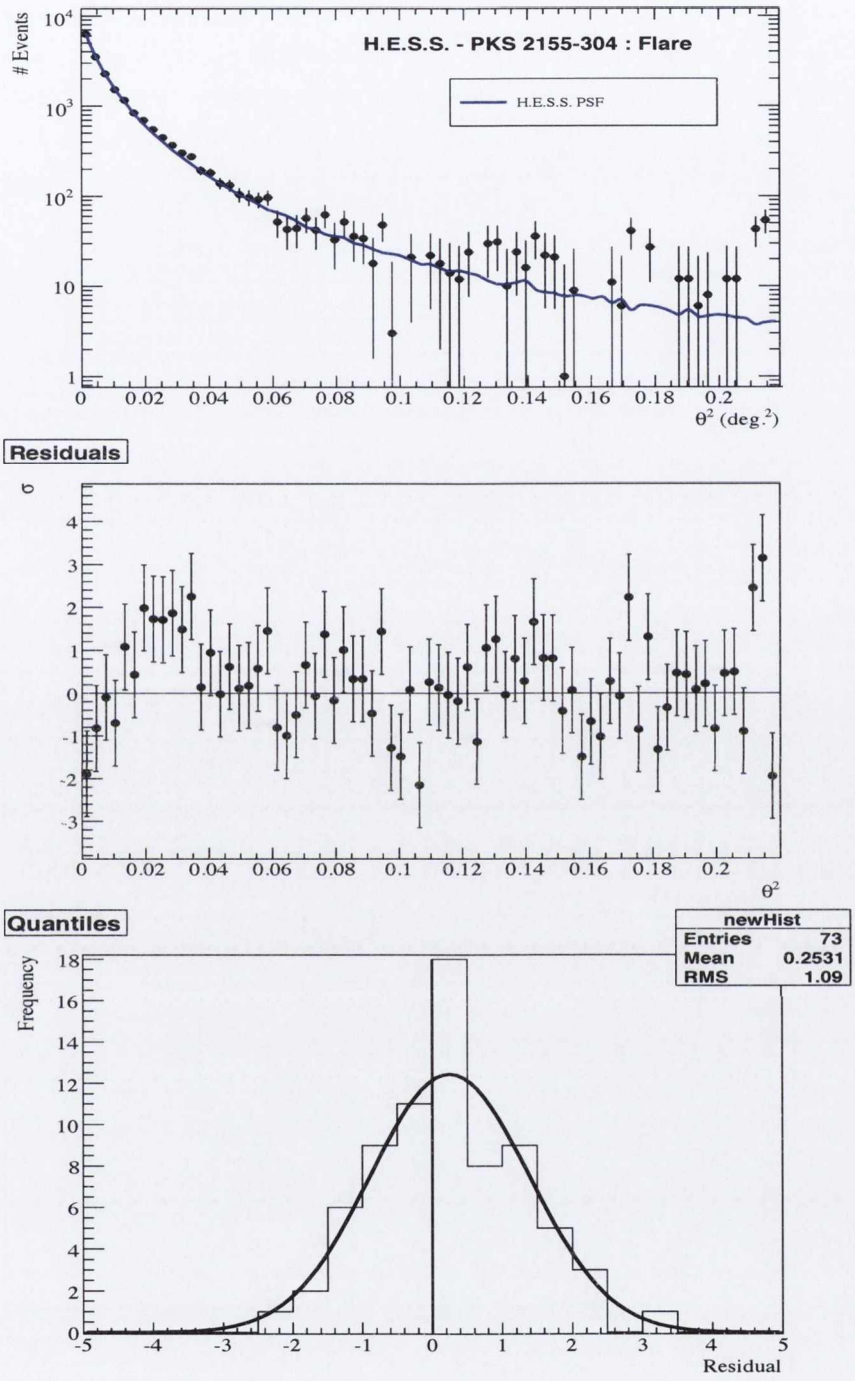

Figure 5.4: *Top Panel: The angular distribution of PKS 2155-304 flare data set, shown in a log scale, fitted with the H.E.S.S. point spread function. Middle Panel: The fit residuals are shown. Lower Panel: The distribution of the residuals are shown as quantiles, fitted with a simple gaussian function.*

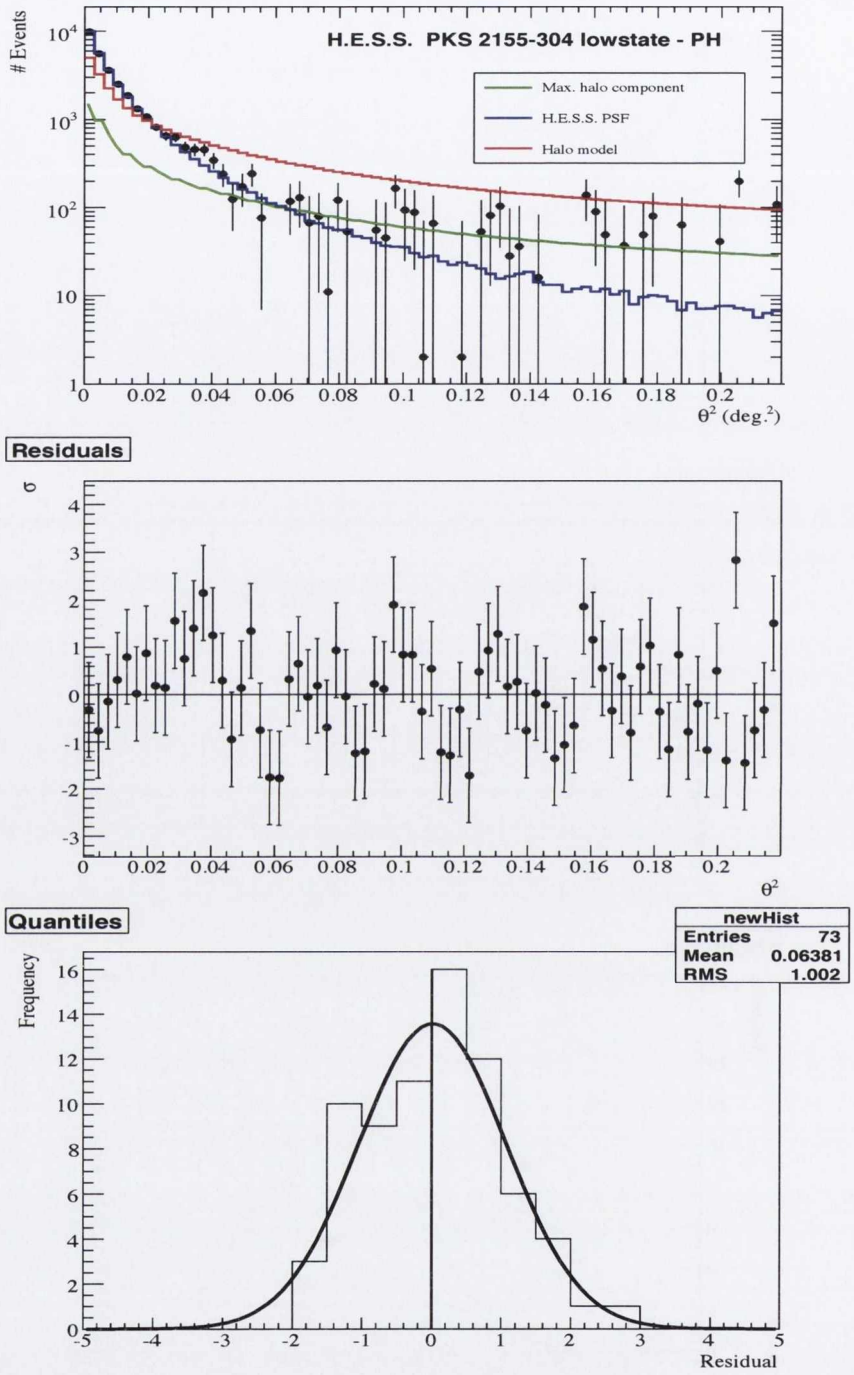

Figure 5.5: *Top Panel: The angular distribution of PKS 2155-304 low state data set, shown in a log scale, fitted with the H.E.S.S. point spread function. Middle Panel: The fit residuals are shown. Lower Panel: The distribution of the residuals are shown as quantiles, fitted with a simple gaussian function.*

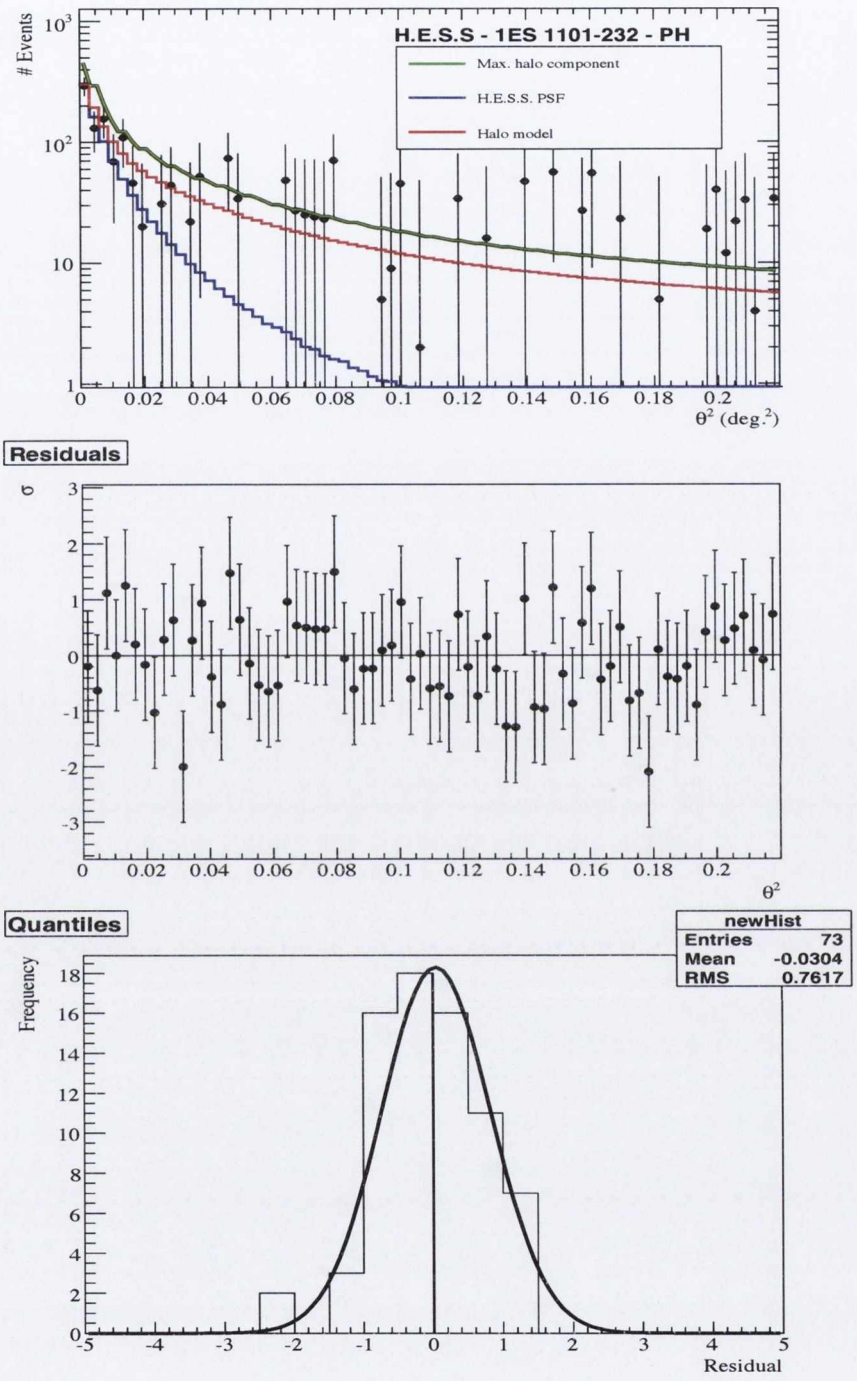

Figure 5.6: *Top Panel: The angular distribution of 1ES 1101-232 data set, shown in a log scale, fitted with the H.E.S.S. point spread function. Middle Panel: The fit residuals are shown. Lower Panel: The distribution of the residuals are shown as quantiles, fitted with a simple gaussian function.*

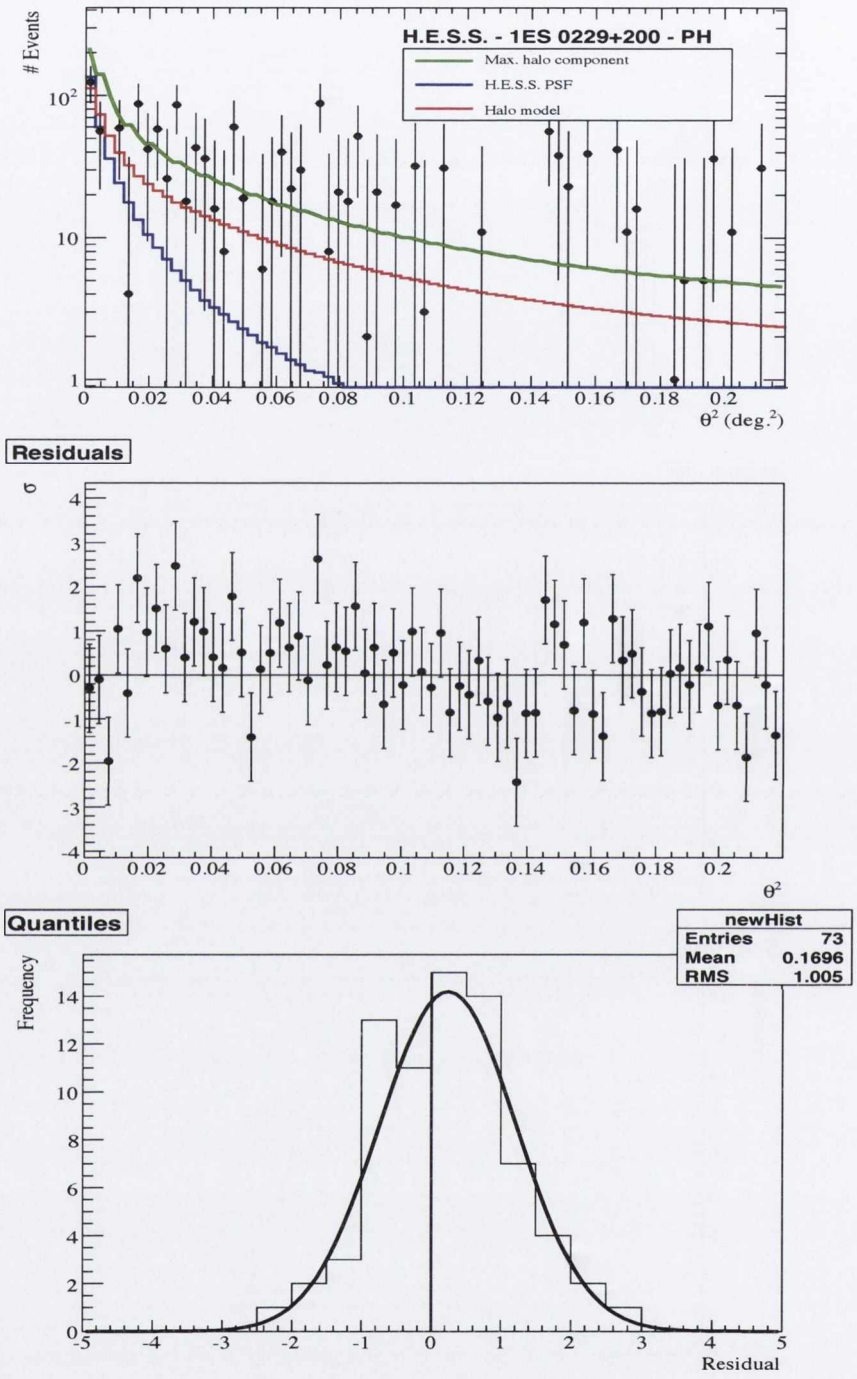

Figure 5.7: *Top Panel: The angular distribution of 1ES 0229+200 data set, shown in a log scale, fitted with the H.E.S.S. point spread function. Middle Panel: The fit residuals are shown. Lower Panel: The distribution of the residuals are shown as quantiles, fitted with a simple gaussian function.*

5.4 Beam Broadened Cascade Analysis

In this section a model dependent approach is applied in order to investigate whether evidence for a beam broadened cascade is found in the angular event distribution of blazar fluxes observed by H.E.S.S. We here utilise a 3D Monte Carlo description of beam broadened cascades developed in Taylor et al. (2011), in order to determine the expected angular profile of this emission for different EGMF strengths. For these calculations, the Franceschini et al. (2008) EBL model was used. Using this description, the range of EGMF values excluded by the present H.E.S.S. results were investigated . A method similar to the model dependent approach described in section **??** was used to obtain these constraints, i.e. $N(\theta^2) = N(\theta^2)_{PSF} + N(\theta^2)_{BBC}$.

For the beam broadened cascade scenario, both the observed SED and angular spread of the arriving flux depend significantly on the EGMF. The angular spreading effect is seen explicitly in Figure 5.8, for which the effect of 10^{-14} G, 10^{-15} G, and 10^{-16} G EGMF values, with a 1 Mpc coherence length, are considered.

All three of the blazars used in our study exhibit no evidence for any intrinsic cutoff of their source spectra at the highest energies observed. Instead, their spectra are consistent with a simple power-law, whose maximum energy must lie beyond the last H.E.S.S. data point. In order for our analysis to be conservative, for each of the sources an injection spectrum of the form $dN/dE \propto E^{-\Gamma} e^{-E/E_{\max}}$ with $\Gamma = 1.5$ and $E_{\max} = 10$ TeV was considered, with the exception of PKS 2155-304 which has an assumed spectrum $\Gamma = 1.8$.

In Figure 5.8, the 0.3 – 1 TeV angular profiles of the resultant beam broadened cascades are shown. Though the comparably low statistics for both 1ES 1101-232 and 1ES 0229+200 limit any constraint from their measured angular profiles, a strong constraint is provided by the angular profile of PKS 2155-304. For this object, a significant cascade contribution results from the required high energy cutoff for which a conservative value of 10 TeV was adopted. For this case, the beam broadening introduced by fields of strength 10^{-15} G or a factor of a few stronger is in conflict with the H.E.S.S. measurements, at the 99.5% C.L. However, for sufficiently strong fields, $> 3 \times 10^{-15}$ G, the cascade component calculated drops below the level of that expected from the direct emission component, reducing the subsequent angular spreading back to that of the H.E.S.S. PSF. Thus, for EGMF values such as those present in the PH scenario discussed in section **??**, the angular profile is expected to be smaller than those found for the case of a 10^{-15} G EGMF value. This strong EGMF suppression effect explains why the above derived 99.5% C.L. on the EGMF value constrains only half a decade of EGMF range. We note that for a larger cutoff energy than the conservative value we adopt in this study, the range of excluded EGMF would be a few times larger.

For the case in which no significant EGMF fields exists, the absorbed component of the injected spectrum photons, through their pair production interactions with EBL photons, is sim-

ply reprocessed through the development of the cascade to produce a relatively flat spectrum at energies below 200 GeV. This result is shown as the $B = 0$ G result in Figure 5.9. Larger EGMF values, however, lead to an energy dependent broadening of the initial jet beam. With the lower energy cascade electrons being more strongly deflected by the EGMF, the beam broadening is largest for these electrons. Indeed, for the 1ES 1101-232 and 1ES 0229+200 blazars, EGMF strengths stronger than 10^{-16} G improve the multi-wavelength SED fit of their cascade spectra to the combined multi-wavelength data, as has been noted in (Dolag et al. 2011; Neronov & Vovk 2010; Tavecchio et al. 2011; Taylor et al. 2011). From the combined SED measurements, EGMF values larger than 10^{-16} G are suggested to be necessary in order to prevent conflict with the *Fermi* blazar flux measurements. This result, however, carries with it an assumption that these blazars are steady sources over extremely long ($\sim 10^6$ yr) timescales (Huan et al. 2011). Relaxing the assumption on the source variability timescale to the level at which it has been observed to be steady (3 yr) reduces the SED derived constraint on the EGMF to $> 10^{-17}$ G (Taylor et al. 2011). Such time delay limitations, however, do not plague angular profile investigations, for which ~300 GeV γ-rays have been used. In this way, the constraints provided by the angular profile studies of blazars offer a complimentary new probe into the EGMF. Using this method, field strengths several orders of magnitude stronger than that probeable from multi-wavelength SED studies become accessible.

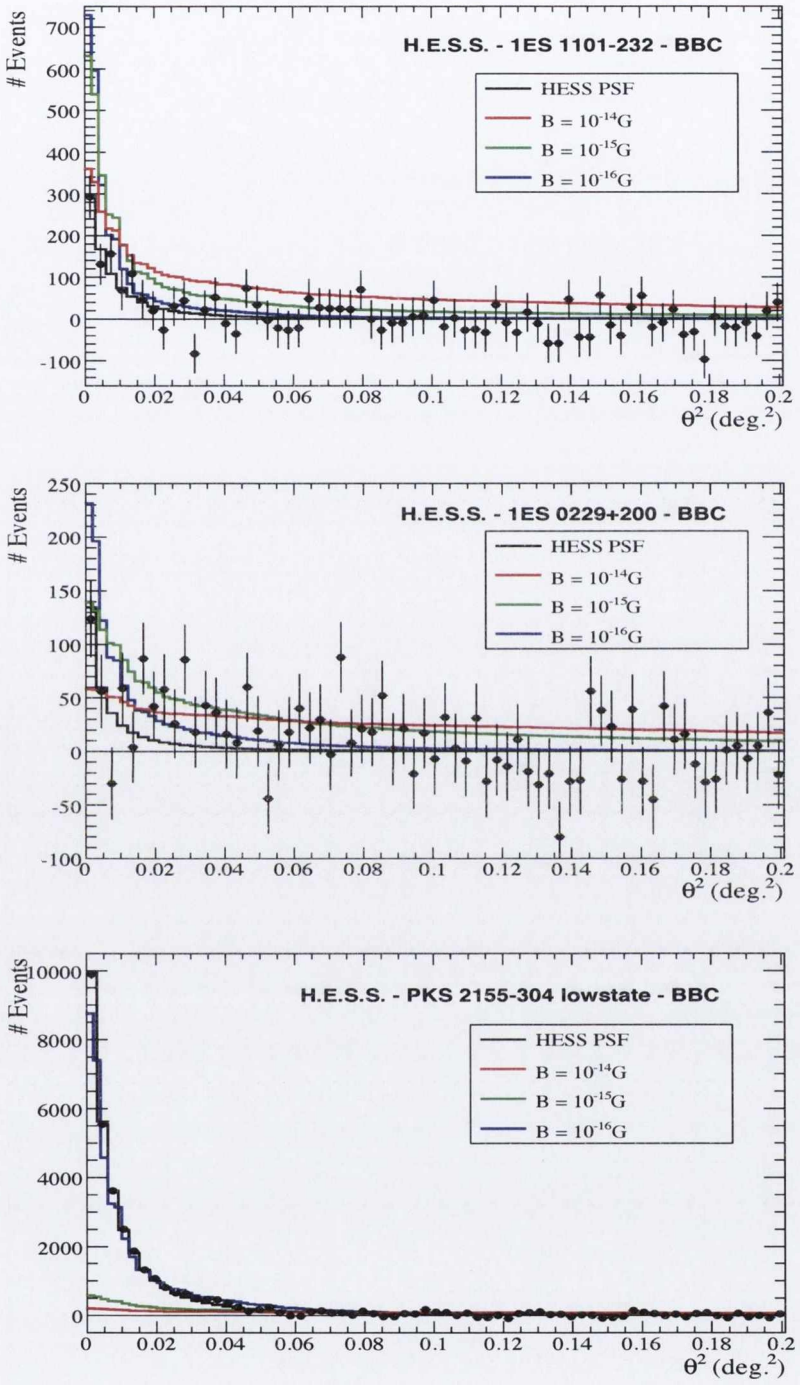

Figure 5.8: *Angular distribution of excess events of 1ES 1101-232 (top), 1ES 0229+200 (middle) and the PKS 2155-304 low state (bottom). The H.E.S.S. data (black points) is plotted against the beam broadened cascade model for varying magnetic field strengths. The red, green and blue lines correspond to the simulated cascade flux for magnetic field strengths of 10^{-14}, 10^{-15} and 10^{-16} G.*

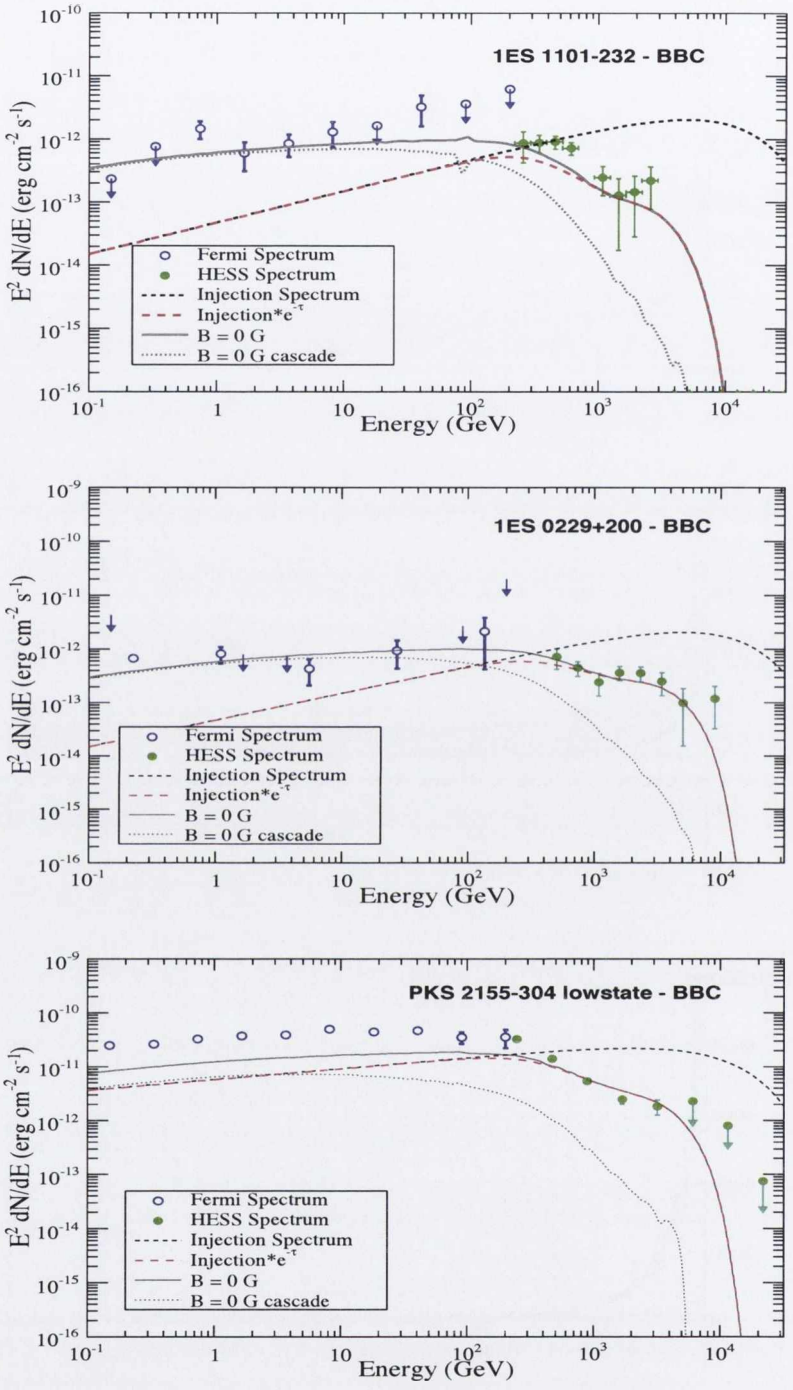

Figure 5.9: *The 1ES 1101-232 (top), 1ES 0229+200 (middle) and PKS 2155-304 (bottom) spectral energy distributions (Γ = 1.5, 1.5 and 1.8 respectively), including Fermi data (blue points) as well as the H.E.S.S. results (green arrows).*

5.5 Discussion & Conclusions

The search for a pair halo surrounding the respective VHE sources, 1ES 1101-232, 1ES 0229+200 and PKS 2155-304, show no indication of pair halo emission. From our analysis, the constraint on the extended emission from our three sources was found to be $< 1\%$, $< 1\%$ and $< 5\%$ of the Crab flux above 1 TeV, respectively. Though our limits are comparable to previous obtained values by other instruments for other blazars, we have here analysed specifically blazars with the strongest evidence for a lack of cutoff up to multi-TeV energies, a prerequisite for pair halo emission. Thus our results mark a significant improvement on previous limits. The limits obtained from this pair halo analysis can be used to set limits on the γ-ray output from these AGN for the past 10^6 years. If any of these AGN were more active in the past, more pairs would consequently have been produced, which would subsequently increase the strength of limit on the extended emission constraint.

A search for beam broadened cascade emission in the arriving flux from these blazars was also carried out. The fluxes from both 1ES 1101-232 and 1ES 0229+200 were found to contain too few statistics for any real constraint to be determined at present. However, a constraint was found to be obtainable using the PKS 2155-304 observational results. From H.E.S.S. observations of the angular profile for PKS 2155-304, the EGMF was excluded for the range $1 - 3 \times 10^{-15}$ G (for a coherence length of 1 Mpc), at the 99.5% C.L. For fields stronger than this range, the cascade component drops below the direct emission contribution and the angular profile tends towards that of a point-like source.

Furthermore, our bound on the EGMF is compatible with the analytic estimates put forward in Aleksić et al. (2010a), although the analysis presented here is the most robust to date due to the theoretical modelling that has been employed. Interestingly, the success proven by this method demonstrates the possibility of probing EGMF levels inaccessible by the previously employed multi-wavelength SED method.

We now look to CTA as our best chance to observe this elusive phenomenon. With a large array size and a wider field of view, the improved angular resolution of this system along with the greater sensitivity will allow for a deeper probing of extended halo emission and beam broadened cascade phenomena.

6

Theoretical Constraints & Future Prospects

In this chapter, the prospects of pair halo detection with future detectors is discussed. The potential of the next generation IACT array, CTA is explored, with the results from simulations presented. The Monte Carlo simulations performed by Eungwanichayapant & Aharonian (2009) have been adapted to reflect the improvements made in recent years in EBL modelling, as well as updating it using input parameters for a more distant source at $z \approx 0.2$ (1ES 1101-232 being a suitable example), facilitating an easier comparison to our work presented in Chapter 5.

A suitable source for future observations is suggested, the radio galaxy 3C 15, stating why this may provide an opportunity to detect pair halo emission.

It should be noted that the results in Section 6.1 (especially those from 6.1.1) have recently been submitted as part of the Special Issue of Astroparticle Physics dedicated to CTA. This work was done in collaboration with Jim Hinton and Richard White (University of Leicester).

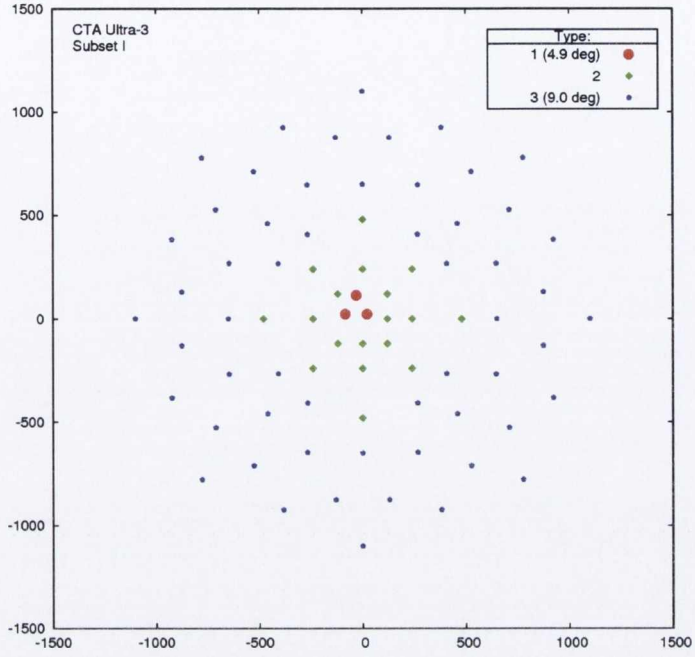

Figure 6.1: *Schematic of the sample configuration I which has 77 telescopes in total. The 23 m telescopes (red), 12 m telescopes (green) and the smaller 7 m telescopes (blue) are shown. The total diameter of the array is ~ 2200 m.*

6.1 CTA

The present generation of imaging atmospheric Cherenkov telescopes (H.E.S.S., MAGIC and VERITAS) have in recent years opened the realm of ground-based γ-ray astronomy for energies above a few tens of GeV. The CTA project is an initiative to build the next generation ground-based VHE γ-ray instrument. It plans to operate in the (E > 10 GeV) energy domain, in close cooperation with observatories operating at other wavelength ranges of the electromagnetic spectrum. CTA aims to be an order of magnitude more sensitive than the current generation of IACTs. It will have an unprecedented spectral coverage as well as superb angular and energy resolution. Besides many anticipated high-energy astrophysical results, CTA will have a large discovery potential in key areas of astronomy, astrophysics and fundamental physics research. We are hopeful that these discoveries will include extended Pair Halo emission.

The CTA consortium plans to operate from two separate sites, one in the southern hemisphere and one in the northern hemisphere (with exact locations still to be decided), allowing full-sky coverage. The southern site will cover the central part of the galactic plane, seeing most of the galactic sources and therefore will be designed to have sensitivity over a broad energy

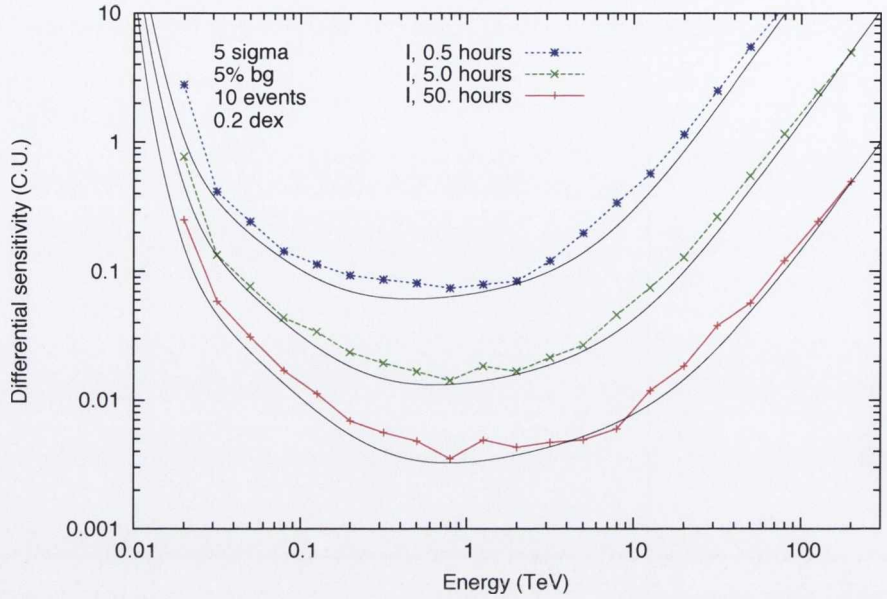

Figure 6.2: *Time and energy dependence of the differential sensitivity (in Crab Units) for configuration I. Exposure times of 0.5, 5 and 50 hours are shown. (Bernlöhr 2008)*

range. The northern site will be optimised for extragalactic astronomy, which is very important for the continuation of this study.

Determining the arrangement and characteristics of the CTA telescopes in the two arrays is a complex optimisation problem, balancing cost against performance in different spectral bands. An on-going design study is being performed and several candidate designs have been proposed (see Bernlöhr (2008)):

- *Low energy threshold* — Smaller number of telescopes (~ 10) with a large mirror area (~ 600 m^2) aimed at reaching very low energies (~ 20 GeV). A sample array, studied by Bernlöhr (2008), is an array consisting of 9 telescopes at 2000 m altitude.

- *High sensitivity* — Dozens of H.E.S.S. type telescopes (~ 40) with a mid-size mirror dish (~ 100 m^2). An example array would consist of 41 telescopes of a type similar to the H.E.S.S. Phase I telescopes.

- *Broad energy range* — An array combining both mid-size and large-area telescopes could combine the advantages of both techniques to extend the energy range and improve the sensitivity. An array of this type, studied in the cited work above, consists of 4 large telescopes

and 85 smaller ones.

- *High energy* — A larger number (~ 40) of small telescopes (~ 40 m^2) with an increased spacing that would aim for a large collection area, which is important for increasing the event statistics at higher energies.

The details of these studies will not be discussed here, only some estimates shown using five of the proposed configurations for the purpose of this study. A brief summary of the configurations are presented in Table 6.1. One of the most promising configurations, Configuration I utilises three telescope types : three 23 m telescopes with 5° field-of-view and 0.09° pixels, 18 telescopes of 12 m diameter with 8° field-of-view and 0.18° pixels, and 56 telescopes of 7 m diameter with a 10° field-of-view and 0.25° pixels. The telescopes are distributed over ~ 4 km^2 on the ground and the effective collection area of the array is considerably larger than this at energies beyond 10 TeV (see Figure 6.1).

An observation time of 50 hours (typical for the first generation of IACTs) is assumed for comparison to previously published sensitivity curves of current instruments. The sensitivity of IACTs are represented in terms of differential sensitivity, where a significant detection (above 5% of the background level, with a $\geq 5\ \sigma$ statistical significance and at least 10 events) is required in each energy bin. The differential flux sensitivity is multiplied by E^2 to show the minimum source flux in terms of power per logarithmic frequency interval and is given in units of erg $cm^{-2}s^{-1}$ for ease of comparison with other wavebands. Alternatively, the Crab nebula, as a strong γ-ray source with a rather typical spectral shape, can be used as a reference. In Figure 6.2, as an example for configuration E, the VHE spectrum as measured with the HEGRA telescope array as a reference, i.e. 1 Crab Unit, is used. (CU) = $2.79 \times 10^{-11}\ E^{-2.57}$ $cm^{-2}\ s^{-1}$ TeV^{-1}.

The superior sensitivity and the broad energy range possible with CTA will allow the discovery of a new class of VHE emitters.

Configuration	Total # of telescopes	Large tel. (23 m)	Medium tel. (12 m)	Small tel. (7 m)	Hemisphere
B	42	5	37	-	S
E	59	4	23	32	S
I	77	3	18	56	S
NA	21	4	17	-	N
NB	28	3	17	8	N

Table 6.1: *Summary of the telescope configurations used in this study.*

6.1.1 Pair Halo Expectations from CTA

The expected flux sensitivity for pair halo detection with CTA has been calculated for four separate approaches. In all cases a differential angular distribution of a pair halo at $z = 0.129$ and $E_\gamma > 100$ GeV, taken from Figure 6 of Eungwanichayapant & Aharonian (2009) was used as our model halo profile, with a functional form: $dN / d\theta^2 \propto \theta^{-5/3}$. The differential energy flux sensitivity for the four different approaches is shown in the upper panel of Figure 6.5.

Methods A and B rely on a 5 σ excess above the expected background, calculated using Equation 17 in Li & Ma (Li & Ma 1983). Method A searches for some overall extended emission with a halo profile for $\theta < 0.32°$. Method B probes a region in which a point-like central source would no longer be dominant ($0.11° < \theta < 0.32°$) and therefore provides the most basic method of establishing the detection of extended emission. For methods C and D the "goodness of fit" for a halo profile (convolved with the CTA PSF) fitted to simulated CTA data is used to determine the expected flux sensitivity. Method C compares a halo fit to the null hypothesis of background fluctuations only, and the optimal θ limit for the fitting was found to be $\approx 0.2°$. Method D however, tests how well a point-like source and a pair halo can be distinguished. This is done by assessing the difference between the likelihood obtained for a PSF hypothesis and that obtained for a pair halo function, with the limiting flux defined as that at which the point-source hypothesis can be rejected at the 5 σ level. The rather poor sensitivity for Method D in Figure 6.5 indicates the difficulty of identifying halo-like emission at this confidence level (CL). If a 95 % CL is taken instead of 5 σ, then the sensitivity of Method D is comparable to Method A and C. Therefore a potentially extended source detected at the sensitivity limit with a significance of 5 σ could be distinguished from a point source with about 95% confidence. Note that in Figure 6.5 the flux quoted is that within a 1° region of the source.

Estimating the total γ-ray luminosity for a source at $z = 0.129$ ($\sim$ 550 Mpc), we obtain a value of $L_0 = 3.3 \times 10^{43}$ erg/s. The lower panel of Figure 6.5 shows the pair halo sensitivity using Method A derived for a range of different CTA candidate configurations. Config. I appears to be the most suitable setup for pair halo studies.

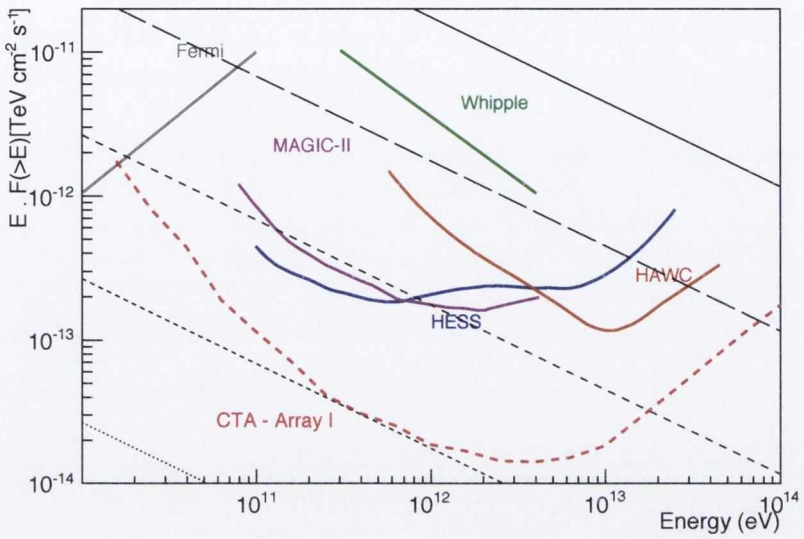

Figure 6.3: *The sensitivity of several high-energy observatories, with a sample curve given for CTA. Reproduced from Parsons (2011).*

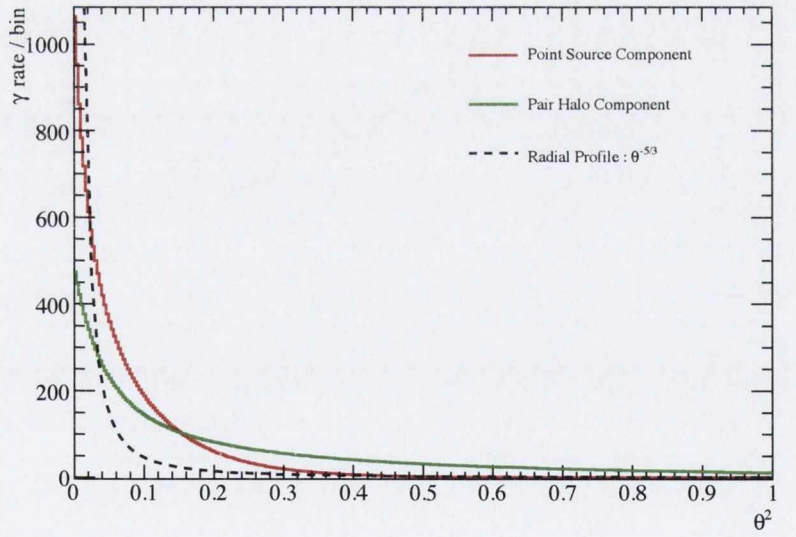

Figure 6.4: *Comparison of a point-like source and an extended pair halo component (assuming configuration E). The halo profile is based on the radial profile ($dN/d\theta^2 \propto \theta^{-5/3}$) which is shown as a dashed line.*

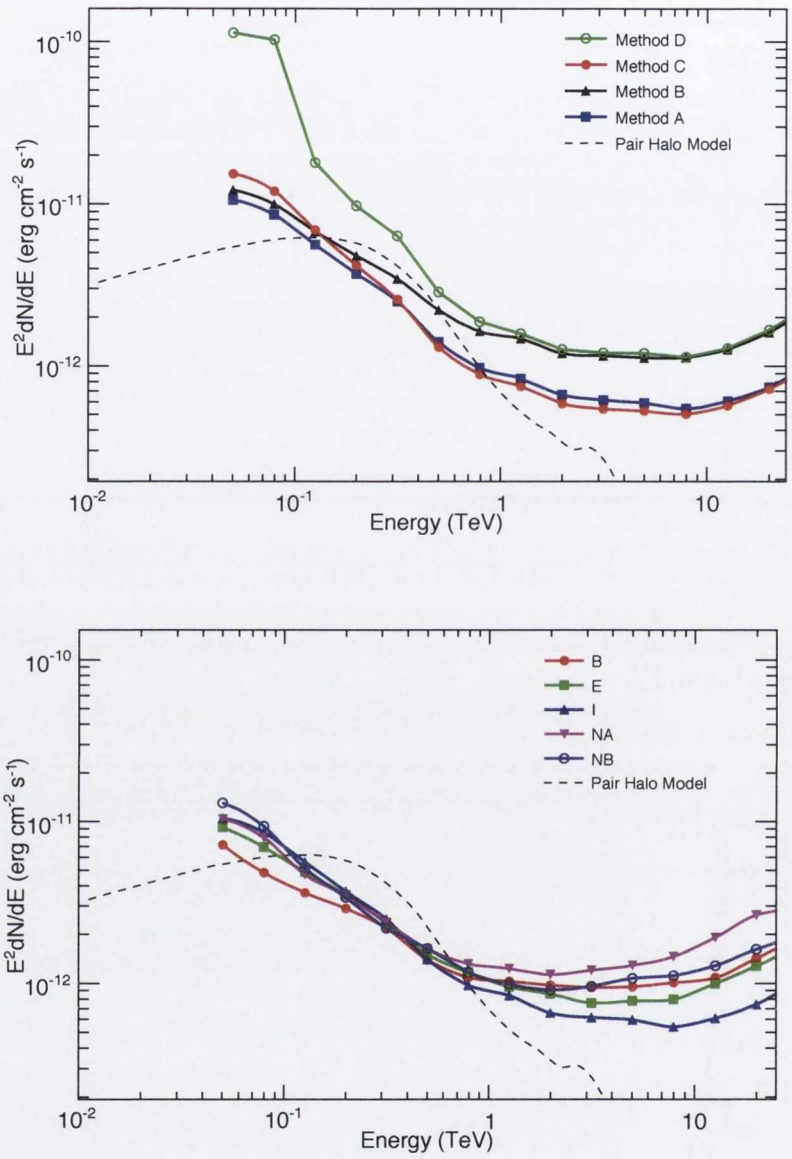

Figure 6.5: *Upper Panel: A comparison of the sensitivity of CTA configuration I to pair halo emission for four different analysis methods. These methods are described in the main text. Lower Panel: Flux estimates on the expected pair halo emission with CTA, for various CTA array configurations (50 hours observing time for each field, 20 degrees zenith angle observations), using analysis Method A. A differential angular distribution of a pair halo at $z = 0.129$ and $E_\gamma > 100$ GeV, taken from Figure 6 (Eungwanichayapant & Aharonian 2009) was used as our theoretical model (dashed black line).*

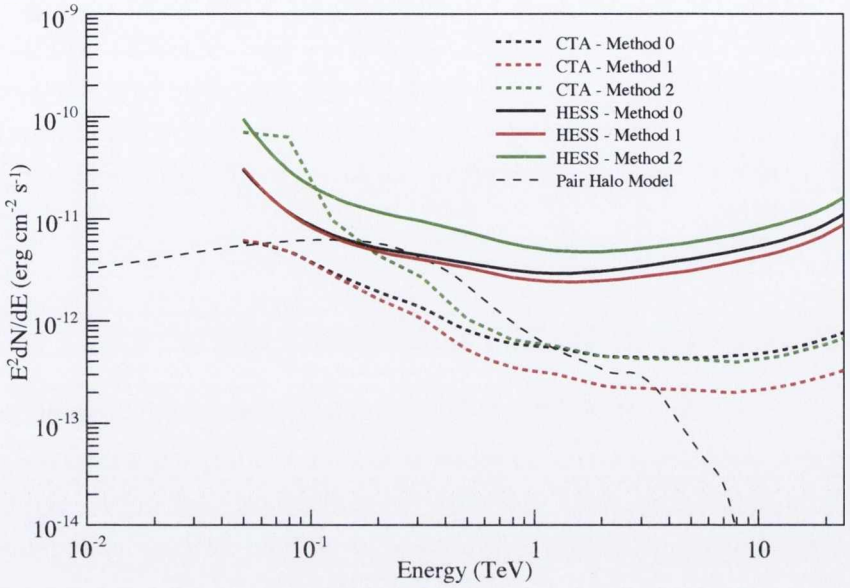

Figure 6.6: *A comparison of the sensitivity of H.E.S.S. and CTA to pair halo emission for three different analysis methods. A differential angular distribution of a pair halo at $z = 0.129$ and $E_\gamma > 100$ GeV, taken from Figure 6 (Eungwanichayapant & Aharonian 2009) was used as our theoretical model (dashed black line).*

The sensitivity of the H.E.S.S. experiment to pair halos compared to that of the expected sensitivity of CTA has been plotted in Figure 6.6, using configuration I. Three methods were used for this analysis, similar to those used in the previous case described above. For each method, a range in θ^2 was fixed to $(0.0125 < \theta^2 < 0.1)$. Method 0 relies on a 5 σ excess above the expected background, calculated using Equation 17 in Li & Ma (Li & Ma 1983) similar to method B described previously. The sensitivity curves shown for methods 1 and 2 (comparable to methods C and D as shown in the upper panel of Figure 6.5) and use the "goodness of fit" approach. It should be noted that the prediction of absolute fluxes contains large uncertainties. However, this figure clearly demonstrates that although CTA will improve our chances of observing Pair Halo emission, it will still be a very challenging task.

6.1.1.1 Optimised Observational Requirements of CTA for Pair Halos

To maximise our chances of observing pair halo emission, the following is the optimised requirements for the CTA array.

At least the current sensitivity of IACT is needed, with milliCrab sensitivity being favourable.

Long observations with a wide field of view would improve the signal/noise ratio, significantly boosting the chance of detection. An overlap in energy range with Fermi would be very interesting and would facilitate the search into the lower energies of the γ-ray spectrum.

If there was a successful detection of pair halo emission, the next step would be to obtain samples from AGN at varying redshifts to constrain the EBL density and distribution. It would also allow for more stringent constraints on the strength of the Intergalactic Magnetic Fields (IGMF).

6.2 Updated Pair Halo Simulations

In this section, the details of the Monte Carlo simulations of pair halo emission performed by Eungwanichayapant& Aharonian (2009) are discussed. Throughout the course of this study, the main results from the above work to make a comparison between our observational results and those from theoretical predictions have been utilised. The differential angular distribution for the $E_\gamma > 100$ GeV case, at $z = 0.129$, was approximated. This was the result most compatible to our sources energy range and redshift and has the functional form: $dN / d\theta^2 \propto \theta^{-5/3}$.

However, in the case of 1ES 1101-232, this comparison is not ideal. Direct access to the Monte Carlo code developed by A. Eungwanichayapant during his PhD (2003) was given, to facilitate a new study. This was considered an ideal opportunity to produce some new results from these simulations, implementing some changes to reflect advances in the understanding of the EBL in recent years, as well as optimising the parameters used for the case of 1ES 1101-232. The results are presented below.

6.2.1 Pair Halos for different EBL models

Since these simulations were first presented in 2003, a concentrated effort has been given to the modelling of the EBL. Although direct measurements of the EBL have proven to be a difficult task due to the dominant foregrounds, indirect constraints on its density can be derived through observations of VHE γ-rays from distant sources. As stated previously, this is a field that has flourished in the past decade. For this reason, the outcome of the results for a more recent EBL model were especially interesting to us. The attenuation factor, $\exp(-\tau)$ for γ-rays as a function of their energy in the case of three different EBL models is shown in Figure 6.10 (upper panel).

In Figure 6.9, the angular distribution of the H.E.S.S. point spread function to that of the pair halo models is compared. The original results using the Primack model (2001) are noticeably more extended than those for the updated Franceschini model (2008).

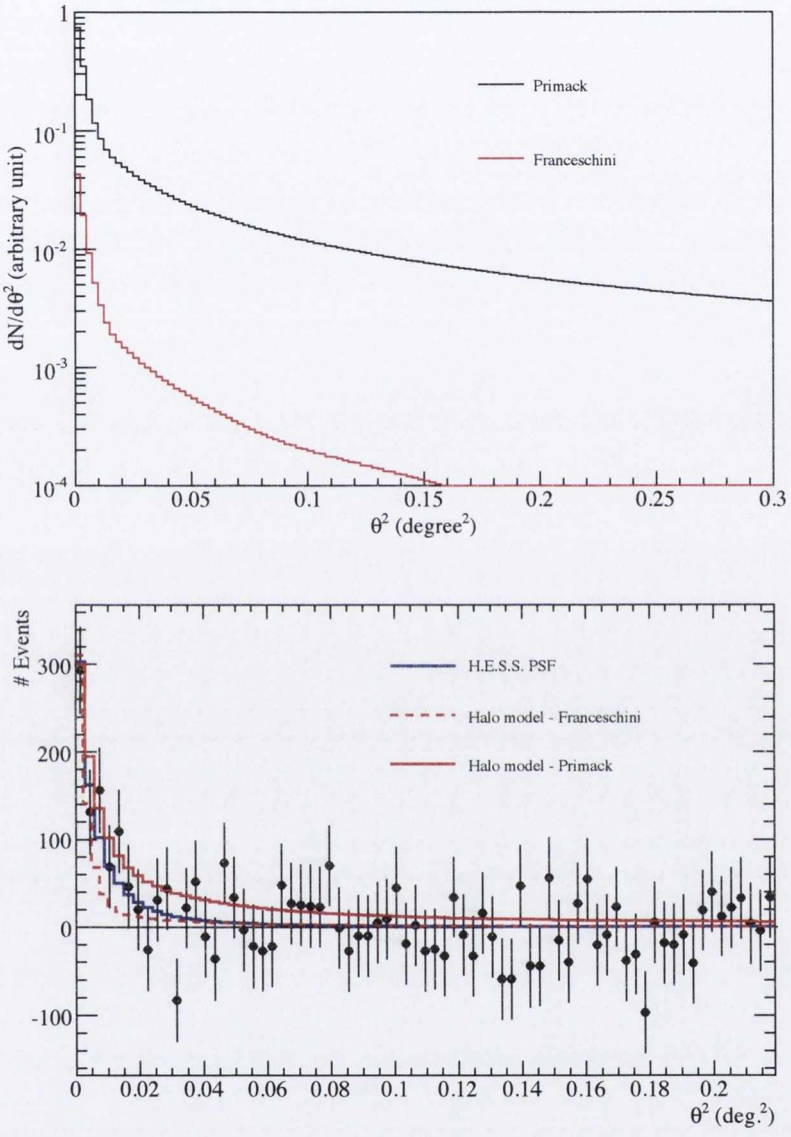

Figure 6.7: *Differential angular distribution of pair halo gamma photons with energy above 100 GeV. The results for different EBL models, Primack et al. (2001) and Franceschini et al. (2008) are shown. In both cases, the pair halo photons are produced from power-law distributed primary γ-rays with an index $\Gamma = 1.5$. Lower Panel:The H.E.S.S. point spread function is shown in blue, with the data points representing γ-ray observations for the source 1ES 1101-232. The model results are scaled to fit the data.*

To make a direct comparison between this work and the results presented in Chapter 5, using the same method for the model dependent upper limits for pair halo emission, this new version of the model to calculate the upper limits for 1ES 1101-232 was used. Using this spatial model, the "maximum halo excess" for this source (i.e. how much of a halo component can be added to the overall shape) at the 95% confidence level, was estimated (see Figure 6.8). The PSF normalisation was left free and the number of excess events in the pair halo model were increased until the fit had a probability < 0.1. The differential limit was then calculated by dividing the maximum number of halo events by the overall exposure, which assumes a spectral index. The result for 1ES 1101-232, assuming $\Gamma_{1.5}$ is 1.04×10^{-12}cm^{-2} s^{-1} TeV^{-1} > 1 TeV, which is a slight improvement on the result previously obtained (1.98×10^{-12}cm^{-2}s^{-1}TeV^{-1} > 1 TeV).

In Figure 6.10 (lower panel), the particular EBL model assumed has a very noticeable difference on the pair halo SED, especially at high energies. In the high energy region (approx $\gtrsim$ 200 GeV) the pair halo SED is quite sensitive to the EBL in the near-infrared range. The Primack model (Primack et al. 2001), exhibits a flattening in the high energy range, which starts to disappear for the Franceschini et al. (2008) model. This is due to the fact that the SED in the near-infrared region for this model has a slightly different form.

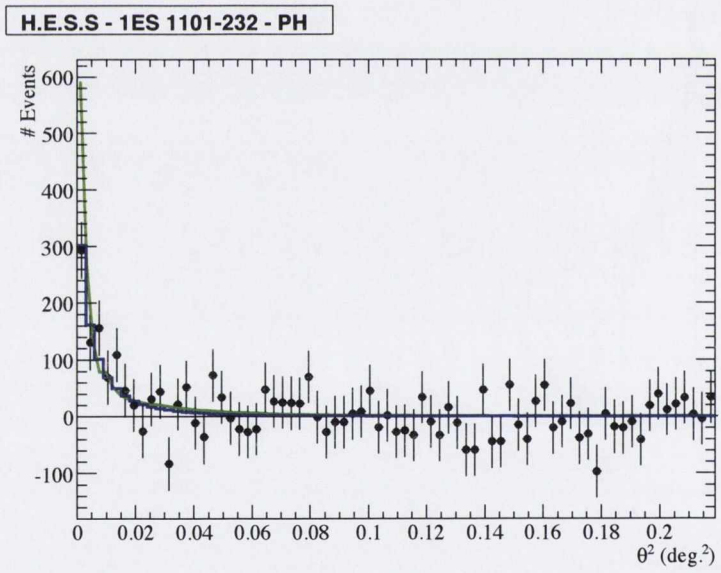

Figure 6.8: *Differential angular distribution of pair halo gamma photons with energy above 100 GeV. The H.E.S.S. PSF (blue line) is shown, compared to the maximum halo excess (green line) at a 95% Confidence Level, with the data points representing the H.E.S.S. observations for 1ES 1101-232.*

Therefore, it should be noted that observing the pair halo spectral energy distribution in the high energy regime can constrain the CIB in the near-infrared range. At lower energies, (< 100 GeV) there is no significant deviation between the two models, however, the photons in this region are the main contributor to the pair halo angular distributions.

It is very difficult to extract the pair halo angular profile, as the PSF is comparable to the halo size. In future, it may be preferable to study nearby objects like Mrk 501 and 421 (with redshifts $z \sim 0.03$) or possibly Arp 220 which is located at a distance of 77 Mpc ($z \sim 0.018$) with CTA.

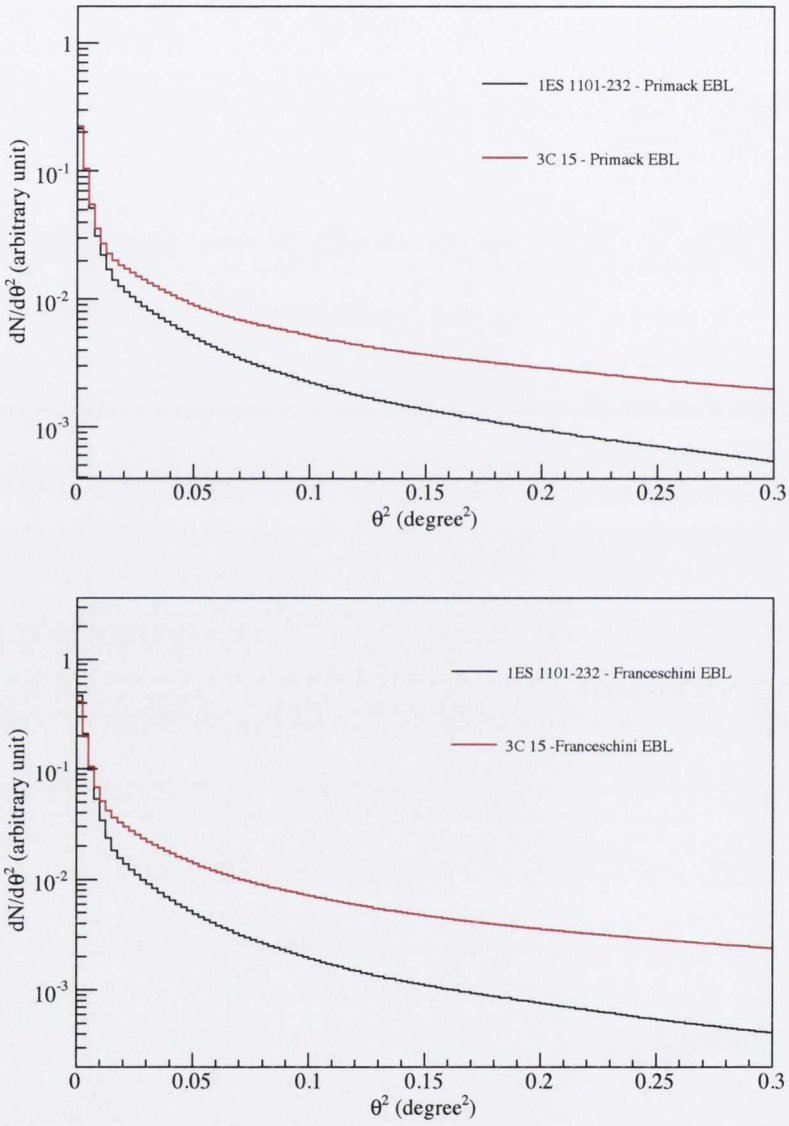

Figure 6.9: *Angular distributions for different EBL models, Primack et al. (2001) and Franceschini et al. (2008) are shown. In both cases, the pair halo photons are produced from power-law distributed primary γ-rays with an index $\Gamma = 1.5$. 1ES 1101-232 has a redshift of $z = 0.186$ whereas 3C 15 is located at $z = 0.073$.*

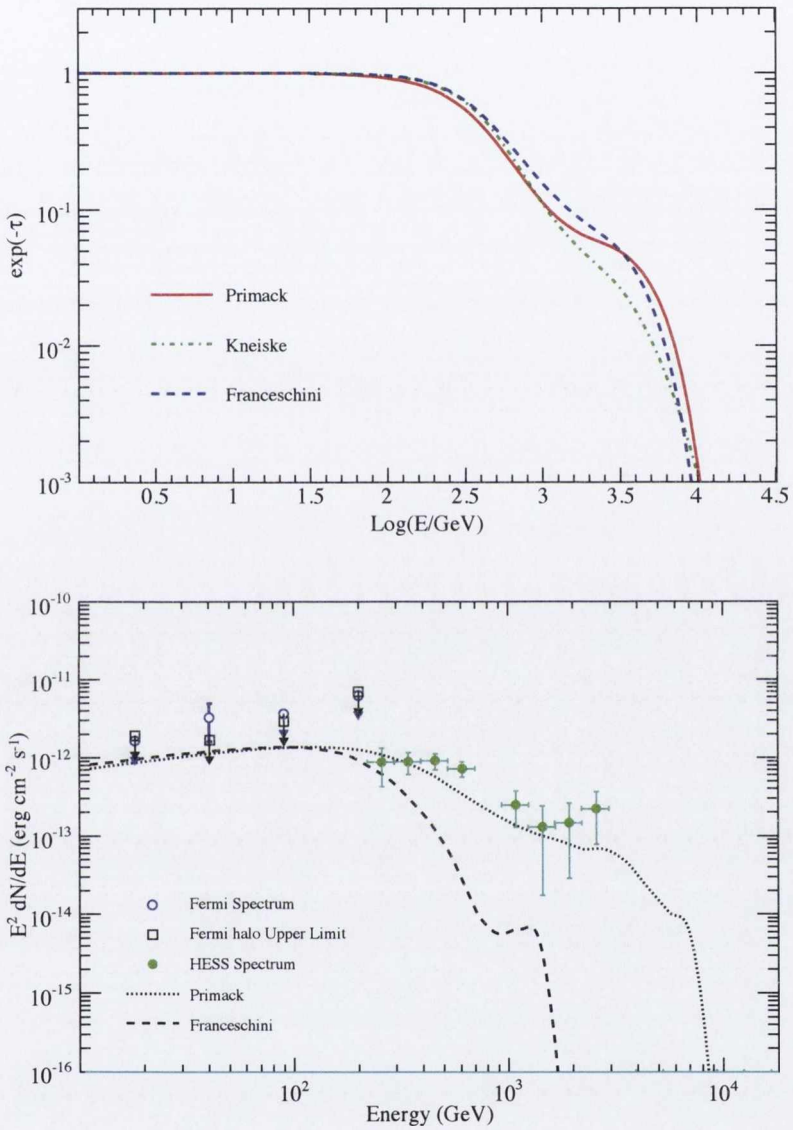

Figure 6.10: *Upper Panel: The attenuation factor exp(-τ) for γ-ray photons as a function of their energy for three different EBL models : Primack et al. (2001), Kneiske et al. (2002) and Franceschini et al. (2008) respectively. Lower Panel: Spectral energy distribution for 1ES 1101-232. The pair halo SEDs for different EBL models are shown, compared to H.E.S.S. and Fermi observations. The pair halo SEDs assume an intrinsic spectrum of* $\Gamma = 1.5$.

6.2.2 Pair Halos for different upper energy limits

Another critical parameter is the upper energy limit, E_2 in the case of power law VHE photon sources. For a primary γ photon spectrum,

$$(dN/dE)_{source} \propto E^{\alpha} \tag{6.1}$$

where $E_1 \leq E \leq E_2$ and α in this case is 1.5. For the results shown below, E_1 is fixed to a value of 100 GeV and E_2 is = 10 TeV or 50 TeV. The angular distribution in Figure 6.11 (upper panel) and the SED in Figure 6.11 (lower panel) show the effect of the upper energy limit on the pair halo profile. With respect to the angular distributions, it is clear that with a higher value of E_2, there is more interaction and hence a higher flux at the centre. For simulations with a higher cutoff energies, e.g. 100 TeV and 500 TeV, the results are almost identical. This implies that the pair halo properties depends sensitively on E_2 for values below $\sim$ 100 TeV.

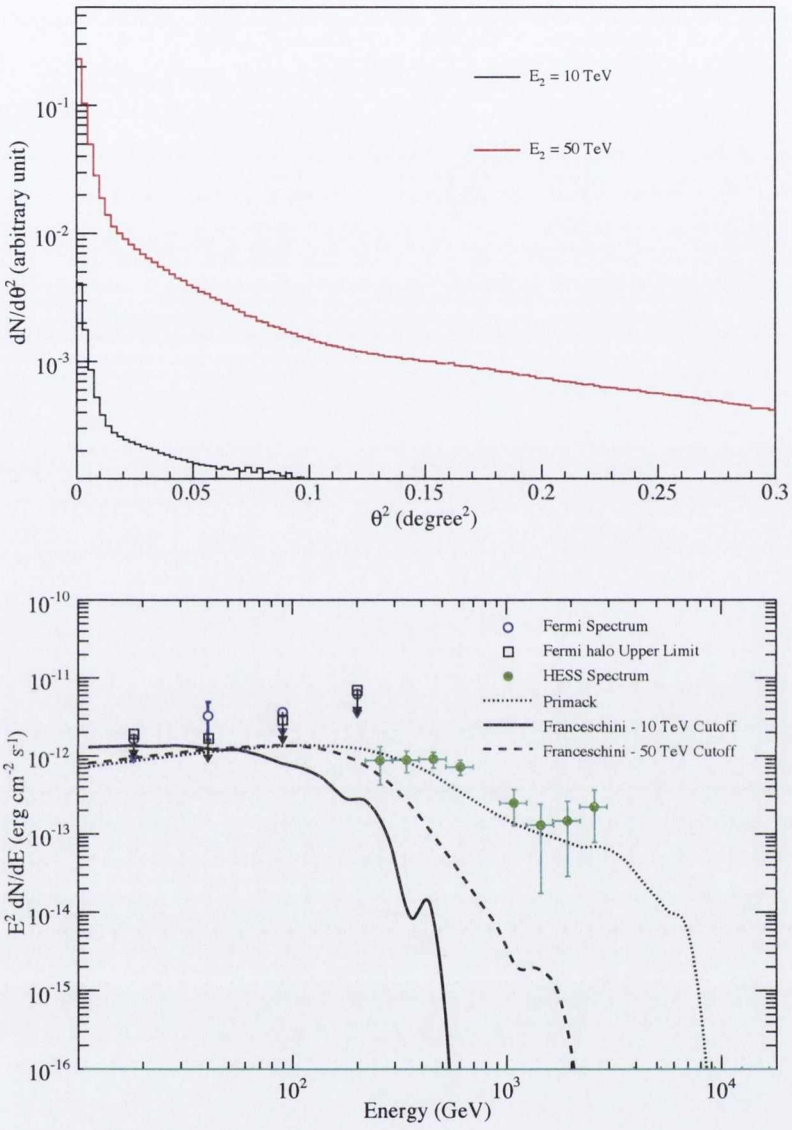

Figure 6.11: *Upper Panel: Differential angular distribution of pair halo gamma photons with energy above 100 GeV, from power-law distributed primary γ-rays with an index $\Gamma = 1.5$. The red line represents an upper energy cutoff (E_2) of 50 TeV, with the 10 TeV cutoff shown in black. Lower Panel: Spectral Energy Distribution for 1ES 1101-232. H.E.S.S. data points are shown (green points), as well as Fermi data (blue circles) and pair halo upper limits (black squares). The dotted black line is the SED of the pair halo gamma photons within 1° for the Franceschini EBL model. The black solid line and dashed line are the SEDs using the Franceschini EBL model with energy limits of 10 TeV and 50 TeV respectively. For each model, an intrinsic spectrum of an $\Gamma = 1.5$ is assumed.*

6.3 Future H.E.S.S. observations - The Radio Galaxy 3C 15

Due to their powerful nature, radio galaxies are the ideal candidates for a pair halo search. 3C 15 is a nearby radio galaxy located at a redshift of $z = 0.073$ Spinrad et al. (1985) which corresponds to a distance of 280 Mpc. This is a suitable distance for a pair halo search, as the preferred distance for observation of a pair halo with the H.E.S.S. experiment, due to the field of view, is in the range of several hundred Mpc to around 1 Gpc. 3C 15 was first catalogued at a frequency of 159 MHz by the Third Cambridge Catalogue of Radio Sources in Bennett (1962). An optical synchrotron jet was discovered in this source by Martel et al. (1998). They reported a very good match between the optical morphology and the features of the radio jet, suggesting the optical emission is strongly dominated by synchrotron radiation. Another curious attribute of this source is that its radio structure is intermediate between Fanaroff-Riley (FR) classes I and II (Leahy et al. 1997). As well as being an ideal candidate for pair halo detection, 3C 15 has the interesting characteristic of being located at Right Ascension (RA) = 0. This would provide the opportunity for deep observations, leading to the establishment of a new source class for the H.E.S.S. experiment of very powerful, distant, non-aligned radio galaxies. Although 3C 15 has been studied from the radio to X-ray band, it has yet to be observed in the γ-ray domain. We are confident that with the new H.E.S.S. analysis we could detect 1×10^{-12} erg cm^{-2} s^{-1} in $\sim$ 50 hours. There are several possible sources for high energy γ ray emission present in 3C 15:

- **nucleus**: As 3C 15 is an AGN, there is a supermassive black hole at the nucleus. The observed hard X-ray spectrum from the nucleus and emission from the inner knots in the radio, optical and X-ray indicates that the AGN has been active for at least 10^4 years. Therefore, particle acceleration and VHE γ-ray production in the vicinity of the nucleus is possible in a number of scenarios. Such non-thermal emission can be time-variable, and this could be used to distinguish from other possible emission sites within 3C 15.

- **knots (kpc - few kpc)**: 3C 15 has a bright northern jet containing four prominent knots, with a much weaker counter-jet on the southern side of the nucleus Kataoka et al. (2003). From Chandra observations, most of the X-ray jet emission comes from a single knot, denoted by *knot C* in their paper. The presence of such knots may imply that the AGN is activated from time to time, leading to the periodic ejection of material along the jet's main axis. (Martel et al. 1998). The radio and optical characteristics of knot C have been interpreted as the signatures of a strong shock with a well-ordered magnetic field and therefore implies high-energy emission Dulwich et al. (2007).

- **lobes (5 kpc - 60 kpc)**: Diffuse X-ray emission was detected by Chandra over the full

extent (63 kpc x 25 kpc) of the radio lobes. The observed hard spectrum suggests an inverse Compton, rather than synchrotron, origin for the X-rays (Kataoka et al. 2003) and places an upper limit on the maximum energy of the accelerated electrons of around 10 TeV. However, such a maximum still allows for γ-rays from IC scattering on the CMB to be produced at the lower end of the energy range detectable by H.E.S.S.

• **outer lobes** (~ **100s of kps**): Although not yet observed, the presence of outer lobes could also add to the energy production mechanisms provided by this source. 3C 15 is the brightest galaxy in a cluster. Electrons accelerated in 3C 15 to high energies may be ejected to the surrounding medium and IC scatter seed photons to γ-ray energies. However, the lifetime of high-energy electrons is limited by IC and synchrotron losses to ~ 10^6 years, so only relatively recently injected electrons will contribute to such emission. However, 3C 15 may also accelerate hadrons. In this case such cosmic rays with energies < 10^{15} eV can accumulate within the greater cluster volume for the entire Hubble time. This CR component, together with the presence of target material in the form of the hot intra-cluster medium (ICM), will lead to VHE γ-ray production via inelastic proton-proton collisions and subsequent π^0 decay. See for example (Hinton et al. 2007).

• **very large scale halo**: If a pair halo is formed through the production of electron/positron pairs by ≫TeV γ-rays from the inner jet, it should be possible to observe extended γ-ray emission from the central source. A non-point like detection would allow us to distinguish between pair-halo emission and the other scenarios. Because the high energy γ-rays in pair halos are produced by TeV electrons, the lifetime of which against Compton losses does not exceed 10^6 yr, the detectability of these structures requires γ-ray activity that has not stopped earlier than 10^6 years ago (Aharonian 2004).

There are several promising sites for high energy γ-ray production in 3C 15, which motivates us greatly to observe this source. 3C 15 is located at RA = $00^h37^m04^s.114$, DEC = -01°09'08".46 in J2000. As mentioned previously, having this particular Right Ascension means 3C 15 has great observing potential.

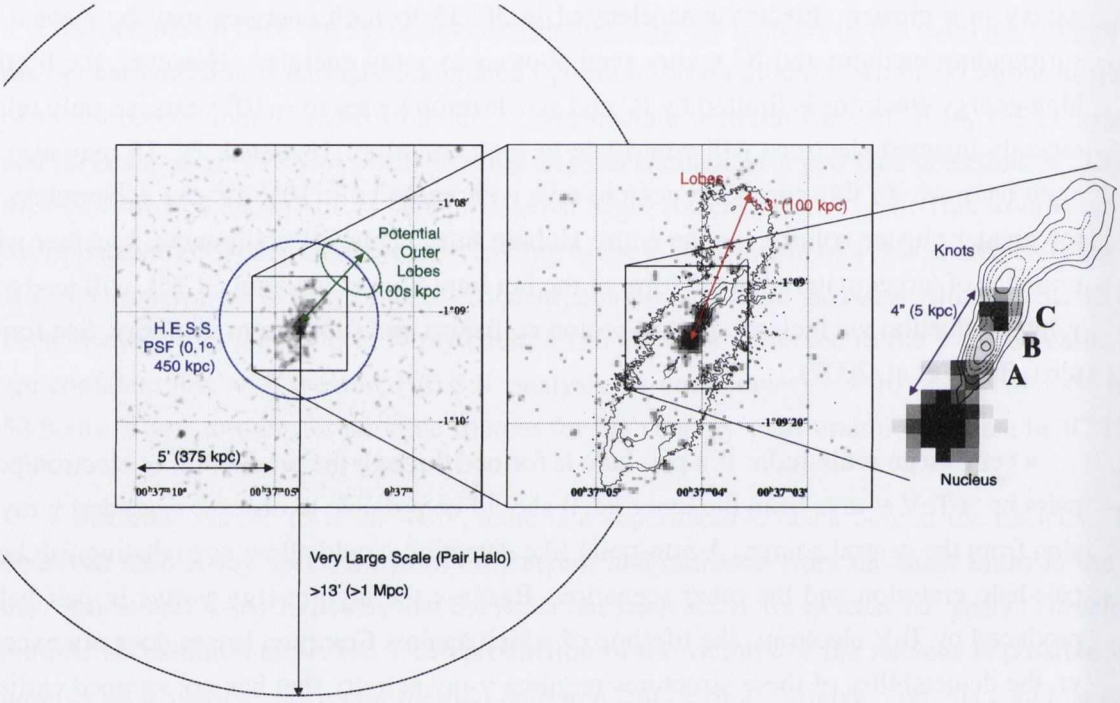

Figure 6.12: *Above is a composite image showing the various scales of observation for 3C 15. Left: a 0.4-0.8 keV X-ray image taken by Chandra. Center: a radio (VLA 8.3 GHz) and X-ray image of the 3C 15 lobes and jet. Right: Expanded plot of the central jet region of 3C 15, where A, B and C denote the jet knots as defined in Martel et al. (1998). Images taken from Kataoka et al. (2003). The black ring represents a very extended pair halo.*

7

Summary and Conclusions

The work presented in this thesis results from a search for signatures of electromagnetic cascades in the intergalactic medium initiated by blazars, undertaken with H.E.S.S., currently the most sensitive ground-based instrument in the γ-ray regime. To date, there has been no confirmed observational evidence of this cascade emission. Its discovery is of prime importance to the community, especially as it would provide constraints on the intergalactic magnetic field strength. From a sample of three sources, PKS 2155-304, 1ES 1101-232 and 1ES 0229+200, a detailed analysis was conducted and the most constraining upper limits to date were obtained. Unfortunately, no significant signal was found in this work, but the results are very promising for a future study with a more sensitive instrument.

The introductory chapters are described as follows :

- In order to select suitable candidates for such a study, in **Chapter 1**, an over-view of the field is given. From the origins of γ-ray astronomy, to the sources in which these photons are produced, a comprehensive introduction to this area of study is presented. The mechanisms for the production of VHE γ-rays are discussed, as well as Active Galactic Nuclei, our source of choice throughout the thesis. A brief introduction to the *Fermi* γ-ray space telescope is also provided.

- The instruments we use for this study, imaging atmospheric cherenkov telescopes are described in **Chapter 2**, as well as the analysis methods used for the core of the thesis. Fundamental aspects of γ-ray astronomy, such as electromagnetic air showers and cherenkov radiation are introduced. Details of the H.E.S.S. telescopes, including both hardware and software techniques are provided in this chapter.

- The two phenomena which are the focal point of this thesis are pair halos and beam broadened cascades. A theoretical overview is presented, detailing the physical processes involved. The importance of the extragalactic background light, as well as the strength of the surrounding intergalactic magnetic fields are discussed in **Chapter 3**.

7.1 General Results

In the years since the H.E.S.S. Cherenkov telescope array became operational, more than 70 γ-ray sources, 30 of which are extra-galactic have been discovered. **Chapter 4** is dedicated to the three AGN chosen for this study, justifying the reasons for their selection. Although the results presented here have not been published, they are in strong agreement with previously published H.E.S.S. results. A detailed analysis of these three objects, PKS 2155-304, 1ES 1101-232 and 1ES 0229+200 is presented in this chapter. Detailed morphological and spectral analyses are performed for all three AGN, as well as coalescing information on these sources to give a complete picture of their characteristics and to demonstrate their suitability for this study.

7.2 Principal Results

The analysis and results of observations of active galactic nuclei PKS 2155-304, 1ES 1101-232 and 1ES 0229+200 were presented in **Chapter 5** with a summary provided here :

- The search for a pair halo surrounding these respective VHE sources show no indication of pair halo emission. From our analysis, the constraint on the extended emission from our three sources was found to be $< 1\%$, $< 1\%$ and $< 5\%$ of the Crab flux above 1 TeV, respectively. Though our limits are comparable to previous obtained values by other instruments for other blazars, we have here analysed specifically blazars with the strongest evidence for a lack of cutoff up to multi-TeV energies, a prerequisite for pair halo emission. Thus our results mark a significant improvement on previous limits. The limits obtained from this pair halo analysis can be used to set limits on the γ-ray output from these AGN for the past 10^6 years. If any of these AGN were more active in the past, more pairs would consequently have been produced,

which would subsequently increase the strength of limit on the extended emission constraint.

- A search for beam broadened cascade emission in the arriving flux from these blazars was also carried out. The fluxes from both 1ES 1101-232 and 1ES 0229+200 were found to contain too few statistics for any real constraint to be determined at present. However, a constraint was found to be obtainable using the PKS 2155-304 observational results. From H.E.S.S. observations of the angular profile for PKS 2155-304, the EGMF was excluded for the range $1 - 3 \times 10^{-15}$ G (for a coherence length of 1 Mpc), at the 99.5% C.L. For fields stronger than this range, the cascade component drops below the direct emission contribution and the angular profile tends towards that of a point-like source.

- Furthermore, our bound on the EGMF is compatible with the analytic estimates put forward in Aleksić et al. (2010a), although the analysis presented here is the most robust to date due to the theoretical modelling that has been employed. Interestingly, the success proven by this method demonstrates the possibility of probing EGMF levels inaccessible by the previously employed multi-wavelength SED method.

7.3 Future Work

It is evident that pair halos are difficult to detect. From the simulations presented in **Chapter 6** for the next generation Cherenkov Telescope Array, we are given some hope but it is clear that it is still a very challenging task. CTA once operational, will provide the best possibility to date of observing this elusive phenomenon. Some interesting ideas for the future include:

- The potential of *radio galaxies as targets* for a pair halo search has been discussed, with 3C 15 given as a suitable candidate. It should be noted that in a recent publication by Aleksić et al. (2010b), VHE γ-rays were observed from IC 310, a head-tail radio galaxy in the Perseus galaxy cluster. Observations of this nature provide fresh motivation to continue this search in the future with this powerful objects.

- Although it extends beyond the remit of the work presented here, it is possible to explore the potential of CTA to *constrain the intergalactic magnetic fields* using similar methods to those outlined in Section 6.1. This could yield some very interesting results and has been proposed as a future "science case study" within the Astroparticle Physics work package for CTA.

- Even though isotropic halo emission could prove too difficult to observe, it may still be *possible to observe some limited extension* (such as beam broadened cascade emission as discussed in Chapters 3 and 5), providing further constraints on the intergalactic magnetic fields.

Bibliography

Abdo, A. A., Ackermann, M., Ajello, M., et al. 2010, ApJS, 188, 405

Acero, F., Aharonian, F., Akhperjanian, A. G., et al. 2009, Science, 326, 1080

Aharonian, F., Akhperjanian, A., Barrio, J., et al. 2001a, A&A, 370, 112

Aharonian, F., Akhperjanian, A., Beilicke, M., et al. 2003a, A&A, 403, 523

Aharonian, F., Akhperjanian, A., Beilicke, M., et al. 2003b, A&A, 403, L1

Aharonian, F., Akhperjanian, A. G., Anton, G., et al. 2009a, A&A, 502, 749

Aharonian, F., Akhperjanian, A. G., Anton, G., et al. 2009b, ApJ, 696, L150

Aharonian, F., Akhperjanian, A. G., Anton, G., et al. 2009c, ApJ, 695, L40

Aharonian, F., Akhperjanian, A. G., Aye, K.-M., et al. 2005a, Science, 307, 1938

Aharonian, F., Akhperjanian, A. G., Aye, K.-M., et al. 2005b, A&A, 430, 865

Aharonian, F., Akhperjanian, A. G., Aye, K.-M., et al. 2004a, Astroparticle Physics, 22, 109

Aharonian, F., Akhperjanian, A. G., Barres de Almeida, U., et al. 2008a, Physical Review Letters, 101, 170402

Aharonian, F., Akhperjanian, A. G., Barres de Almeida, U., et al. 2007a, A&A, 475, L9

Aharonian, F., Akhperjanian, A. G., Bazer-Bachi, A. R., et al. 2007b, ApJ, 664, L71

Aharonian, F., Akhperjanian, A. G., Bazer-Bachi, A. R., et al. 2005c, A&A, 437, L7

Aharonian, F., Akhperjanian, A. G., Bazer-Bachi, A. R., et al. 2006a, A&A, 449, 223

Aharonian, F., Akhperjanian, A. G., Bazer-Bachi, A. R., et al. 2006b, ApJ, 636, 777

Aharonian, F., Akhperjanian, A. G., Bazer-Bachi, A. R., et al. 2006c, Nature, 440, 1018

Aharonian, F., Akhperjanian, A. G., Bazer-Bachi, A. R., et al. 2007c, A&A, 470, 475

Aharonian, F., Akhperjanian, A. G., & the H.E.S.S. Collaboration. 2006d, A&A, 457, 899

Aharonian, F. A. 2001, in International Cosmic Ray Conference, Vol. 27, International Cosmic Ray Conference, 1250+

Aharonian, F. A. 2004, Very high energy cosmic gamma radiation : a crucial window on the extreme Universe, ed. Aharonian, F. A.

Aharonian, F. A., Akhperjanian, A. G., Aye, K.-M., et al. 2004b, Nature, 432, 75

Aharonian, F. A., Akhperjanian, A. G., Barrio, J. A., et al. 2001b, A&A, 366, 746

Aharonian, F. A., Atoian, A. M., & Nagapetian, A. M. 1983, Astrofizika, 19, 323

Aharonian, F. A., Coppi, P. S., & Voelk, H. J. 1994, ApJ, 423, L5

Aharonian, F. A., Khangulyan, D., & Costamante, L. 2008b, MNRAS, 387, 1206

Aharonian, F. A., Timokhin, A. N., & Plyasheshnikov, A. V. 2002, A&A, 384, 834

Albert, J., Aliu, E., Anderhub, H., et al. 2007a, ApJ, 663, 125

Albert, J., Aliu, E., Anderhub, H., et al. 2007b, ApJ, 669, 862

Aleksić, J., Alvarez, E. A., Antonelli, L. A., et al. 2012, A&A, 539, L2

Aleksić, J., Antonelli, L. A., Antoranz, P., et al. 2010a, A&A, 524, A77+

Aleksić, J., Antonelli, L. A., Antoranz, P., et al. 2010b, ApJ, 723, L207

Ando, S. & Kusenko, A. 2010, ApJ, 722, L39

Antoni, T., Apel, W. D., Badea, A. F., et al. 2005, Astroparticle Physics, 24, 1

Atwood, W. B., Abdo, A. A., Ackermann, M., et al. 2009, ApJ, 697, 1071

Barthel, P. D., Conway, J. E., Myers, S. T., Pearson, T. J., & Readhead, A. C. S. 1995, ApJ, 444, L21

Benbow, W. 2005, Proceedings of Towards a Network of Atmospheric Cherenkov Detectors VII (Palaiseau), 163

Bennett, A. S. 1962, MmRAS, 68, 163

Berge, D., Funk, S., & Hinton, J. 2007, A&A, 466, 1219

Bernlöhr, K. 2008, in American Institute of Physics Conference Series, Vol. 1085, American Institute of Physics Conference Series, ed. F. A. Aharonian, W. Hofmann, & F. Rieger, 874–877

Bernlöhr, K., Carrol, O., Cornils, R., et al. 2003, Astroparticle Physics, 20, 111

Bernstein, R. A. 2007, ApJ, 666, 663

Bernstein, R. A., Freedman, W. L., & Madore, B. F. 2002, ApJ, 571, 107

Bhattacharjee, P. 2000, Phys. Rep., 327, 109

Biermann, P. L., Chirvasa, M., Falcke, H., Markof, S., & Zier, C. 2002, ArXiv Astrophysics e-prints : astro-ph/0211503

Bolz, O. 2004, PhD Thesis, Ruprecht-Karls Universitat, Heidelberg

Buckley, D. A. H., Tuohy, I. R., & Remillard, R. A. 1985, Proceedings of the Astronomical Society of Australia, 6, 147

Cambrésy, L., Reach, W. T., Beichman, C. A., & Jarrett, T. H. 2001, ApJ, 555, 563

Čerenkov, P. A. 1937, Phys. Rev., 52, 378

Chadwick, P. M., Lyons, K., McComb, T. J. L., et al. 1999, ApJ, 513, 161

Chary, R., Casertano, S., Dickinson, M. E., et al. 2004, ApJS, 154, 80

Cherenkov, P. 1935, Dokl. Akad. Nauk. USSR, 2, 451

Cillis, A. & Sciutto, S. J. 2000, Journal of Physics G Nuclear Physics, 26, 309

Collmar, W. 2001, Gamma-Ray Emission of Active Galaxies, ed. Schönfelder, V., 285–317

Coppi, P. S. & Aharonian, F. A. 1997, ApJ, 487, L9+

Coppi, P. S. & Blandford, R. D. 1990, MNRAS, 245, 453

Cornils, R., Gillessen, S., Jung, I., et al. 2003, Astroparticle Physics, 20, 129

Davies, J. & Cotton, E. 1957, Journal of Solar Energy, 1, 16

de Naurois, M. & Rolland, L. 2009, Astroparticle Physics, 32, 231

Dermer, C. D., Schlickeiser, R., & Mastichiadis, A. 1992, A&A, 256, L27

Dolag, K., Kachelriess, M., Ostapchenko, S., & Tomàs, R. 2011, ApJ, 727, L4+

Dole, H., Lagache, G., Puget, J.-L., et al. 2006, A&A, 451, 417

Drury, L. O., Aharonian, F. A., & Voelk, H. J. 1994, A&A, 287, 959

Dulwich, F., Worrall, D. M., Birkinshaw, M., Padgett, C. A., & Perlman, E. S. 2007, MNRAS, 374, 1216

Elbaz, D., Cesarsky, C. J., Chanial, P., et al. 2002, A&A, 384, 848

Elvis, M., Plummer, D., Schachter, J., & Fabbiano, G. 1992, ApJS, 80, 257

Essey, W., Kalashev, O., Kusenko, A., & Beacom, J. F. 2011, ApJ, 731, 51

Eungwanichayapant, A. & Aharonian, F. 2009, International Journal of Modern Physics D, 18, 911

Falomo, R. & Pesce, J. E. 1994, The Messenger, 78, 30

Falomo, R., Pesce, J. E., & Treves, A. 1993, ApJ, 411, L63

Falomo, R., Scarpa, R., & Bersanelli, M. 1994, ApJS, 93, 125

Falomo, R. & Ulrich, M.-H. 2000, A&A, 357, 91

Fazio, G. G., Ashby, M. L. N., Barmby, P., et al. 2004, ApJS, 154, 39

Feldman, G. J. & Cousins, R. D. 1998, Phys. Rev. D, 57, 3873

Fixsen, D. J., Dwek, E., Mather, J. C., Bennett, C. L., & Shafer, R. A. 1998, ApJ, 508, 123

Franceschini, A., Rodighiero, G., & Vaccari, M. 2008, A&A, 487, 837

Frayer, D. T., Huynh, M. T., Chary, R., et al. 2006, ApJ, 647, L9

Fugmann, W. 1988, A&A, 205, 86

Funk, S. 2005, PhD Thesis, Max-Plank-Institut fur KernPhysik

Funk, S., Hermann, G., Hinton, J., et al. 2004, Astroparticle Physics, 22, 285

Funk, S., Hinton, J., Hermann, G., et al. 2005, in American Institute of Physics Conference Series, Vol. 745, High Energy Gamma-Ray Astronomy, ed. F. A. Aharonian, H. J. Völk, & D. Horns, 753–757

Galbraith, W. & Jelley, J. V. 1953, Nature, 171, 349

Gardner, J. P., Brown, T. M., & Ferguson, H. C. 2000, ApJ, 542, L79

Gorjian, V., Wright, E. L., & Chary, R. R. 2000, ApJ, 536, 550

Gould, R. J. & Schréder, G. P. 1967, Physical Review, 155, 1404

Greisen, K. 1966, Physical Review Letters, 16, 748

Hartman, R. C., Webb, J. R., Marscher, A. P., et al. 1996, ApJ, 461, 698

Hauser, M. G., Arendt, R. G., Kelsall, T., et al. 1998, ApJ, 508, 25

Heck, D., Knapp, J., Capdevielle, J. N., Schatz, G., & Thouw, T. 1998, CORSIKA: a Monte Carlo code to simulate extensive air showers., ed. Heck, D., Knapp, J., Capdevielle, J. N., Schatz, G., & Thouw, T.

HESS Collaboration, Abramowski, A., Acero, F., et al. 2010, A&A, 520, A83+

Hillas, A. M. 1984, ARA&A, 22, 425

Hillas, A. M. 1985, in International Cosmic Ray Conference, Vol. 3, International Cosmic Ray Conference, 445–448

Hillas, A. M. 1996, Space Sci. Rev., 75, 17

Hinton, J. 2009, New Journal of Physics, 11, 055005

Hinton, J. A. 2004, New A Rev., 48, 331

Hinton, J. A., Domainko, W., & Pope, E. C. D. 2007, MNRAS, 382, 466

Hofmann, W. 2000, Astroparticle Physics, 12, 207

Hofmann, W., Jung, I., Konopelko, A., et al. 1999, Astroparticle Physics, 12, 135

Huan, H., Weisgarber, T., Arlen, T., & Wakely, S. P. 2011, ApJ, 735, L28+

Impey, C. D., Lawrence, C. R., & Tapia, S. 1991, ApJ, 375, 46

Jelley, J. V. & Porter, N. A. 1963, QJRAS, 4, 275

Jones, T. W., O'dell, S. L., & Stein, W. A. 1974, ApJ, 188, 353

Karle, A., Ahrens, J., Bahcall, J. N., et al. 2003, Nuclear Physics B Proceedings Supplements, 118, 388

Karle, for the IceCube Collaboration, A. f. 2010, ArXiv e-prints : astro-ph/1003.5715

Kataoka, J., Leahy, J. P., Edwards, P. G., et al. 2003, A&A, 410, 833

Katz, U. F. 2006, Nuclear Instruments and Methods in Physics Research A, 567, 457

Kneiske, T. M., Mannheim, K., & Hartmann, D. H. 2002, A&A, 386, 1

Konigl, A. 1981, ApJ, 243, 700

Kotera, K. & Olinto, A. V. 2011, ARA&A, 49, 119

Kotilainen, J. K., Falomo, R., & Scarpa, R. 1998, A&A, 336, 479

Leahy, J. P., Black, A. R. S., Dennett-Thorpe, J., et al. 1997, MNRAS, 291, 20

Levenson, L. R. & Wright, E. L. 2008, ApJ, 683, 585

Li, T.-P. & Ma, Y.-Q. 1983, ApJ, 272, 317

Longair, M. S. 1992, High energy astrophysics. Vol.1: Particles, photons and their detection, ed. Willcox, P. J.

Madau, P. & Pozzetti, L. 2000, MNRAS, 312, L9

Mannheim, K. & Biermann, P. L. 1992, A&A, 253, L21

Martel, A. R., Sparks, W. B., Macchetto, D., et al. 1998, ApJ, 496, 203

Matsumoto, T., Matsuura, S., Murakami, H., et al. 2005, ApJ, 626, 31

Meyer, M., Horns, D., & Zechlin, H.-S. 2010, A&A, 523, A2+

Meyer, M., Raue, M., Mazin, D., & Horns, D. 2012, ArXiv e-prints : astro-ph/1202.2867 in press

Morrison, P. 1958, Il Nuovo Cimento, 7, 858

Nedbal, D. 2008, PhD Thesis, Ruprecht-Karls Universitat, Heidelberg

Neronov, A., Semikoz, D. V., Tinyakov, P. G., & Tkachev, I. I. 2011, A&A, 526, A90+

Neronov, A. & Vovk, I. 2010, Science, 328, 73

Orr, M. R., Krennrich, F., & Dwek, E. 2011, ApJ, 733, 77

Paneque, D. 2004, PhD Thesis, Max-Plank-Institut fur Physik

Papovich, C., Dole, H., Egami, E., et al. 2004, ApJS, 154, 70

Parsons, R. 2011, PhD Thesis, University of Leeds.

Perlman, E. S., Stocke, J. T., Schachter, J. F., et al. 1996, ApJS, 104, 251

Plaga, R. 1995, Nature, 374, 430

Pohl, M., Reich, W., Krichbaum, T. P., et al. 1995, A&A, 303, 383

Porter, N. A. & Weekes, T. C. 1977, SAO Special Report, 381

Primack, J., Bullock, J., & Somerville, R. S. 2005, American Institute of Physics Conference Series, 745, 23

Primack, J. R., Gilmore, R. C., & Somerville, R. S. 2008, in American Institute of Physics Conference Series, Vol. 1085, American Institute of Physics Conference Series, ed. F. A. Aharonian, W. Hofmann, & F. Rieger, 71–82

Primack, J. R., Somerville, R. S., Bullock, J. S., & Devriendt, J. E. G. 2001, in American Institute of Physics Conference Series, Vol. 558, American Institute of Physics Conference Series, ed. F. A. Aharonian & H. J. Völk, 463–478

Punch, M., Akerlof, C. W., Cawley, M. F., et al. 1992, Nature, 358, 477

Rector, T. A., Gabuzda, D. C., & Stocke, J. T. 2003, AJ, 125, 1060

Remillard, R. A., Tuohy, I. R., Brissenden, R. J. V., et al. 1989, ApJ, 345, 140

Romero, G. E., Cellone, S. A., & Combi, J. A. 1999, A&AS, 135, 477

Rowell, G. P. 2003, A&A, 410, 389

Rybicki, G. B. & Lightman, A. P. 1979, Radiative processes in astrophysics, ed. Rybicki, G. B. & Lightman, A. P.

Sikora, M., Begelman, M. C., & Rees, M. J. 1994, ApJ, 421, 153

Spinrad, H., Marr, J., Aguilar, L., & Djorgovski, S. 1985, PASP, 97, 932

Stecker, F. W., Malkan, M. A., & Scully, S. T. 2006, ApJ, 648, 774

Takeda, M., Hayashida, N., Honda, K., et al. 1999, ApJ, 522, 225

Tamm, I. & Frank, I. 1937, Dokl. Akad. Nauk. USSR, 544, 107

Tavecchio, F., Ghisellini, G., Bonnoli, G., & Foschini, L. 2011, MNRAS, 414, 3566

Tavecchio, F., Ghisellini, G., Foschini, L., et al. 2010, MNRAS, 406, L70

Taylor, A. M., Vovk, I., & Neronov, A. 2011, A&A, 529, A144

The Fermi-LAT Collaboration. 2011, ArXiv e-prints : astro-ph/1108.1435

The Pierre Auger Collaboration, Abraham, J., Abreu, P., et al. 2007, Science, 318, 938

Urry, C. M. & Padovani, P. 1995, PASP, 107, 803

Vassiliev, V. V. 2000, Astroparticle Physics, 12, 217

VERITAS Collaboration, Acciari, V. A., Aliu, E., et al. 2009, Nature, 462, 770

Véron-Cetty, M.-P. & Véron, P. 2006, A&A, 455, 773

Vestrand, W. T., Stacy, J. G., & Sreekumar, P. 1995, ApJ, 454, L93+

Vovk, I., Taylor, A. M., Semikoz, D., & Neronov, A. 2012a, ApJ, 747, L14

Vovk, I., Taylor, A. M., Semikoz, D., & Neronov, A. 2012b, ApJ, 747, L14

Wang, X.-Y., Liu, R.-Y., & Aharonian, F. 2011, ApJ, 736, 112

Weekes, T. C., Cawley, M. F., Fegan, D. J., et al. 1989, ApJ, 342, 379

Weinberg, S. 1995, The Quantum Theory of Fields, ed. Weinberg, S.

Williams, W. S. C. 1991, Nuclear and particle physics., ed. Williams, W. S. C.

Wills, B. J., Wills, D., Breger, M., Antonucci, R. R. J., & Barvainis, R. 1992, ApJ, 398, 454

Woo, J., Urry, C. M., van der Marel, R. P., Lira, P., & Maza, J. 2005, ApJ, 631, 762

Wright, E. L. 2001, ApJ, 553, 538

Wright, E. L. 2004, New A Rev., 48, 465

Wright, E. L. & Reese, E. D. 2000, ApJ, 545, 43

Xu, C. K., Donas, J., Arnouts, S., et al. 2005, ApJ, 619, L11

Zacharopoulou, O., Khangulyan, D., Aharonian, F. A., & Costamante, L. 2011, ApJ, 738, 157

Zatsepin, G. T. & Kuz'min, V. A. 1966, JETP Letters, 4, 78